DISSERTATION

zur Erlangung
des naturwissenschaftlichen Doktorgrades
der Bayerischen Julius-Maximilians-Universität
Würzburg

Non-Newtonian Properties of Magmatic Melts

vorgelegt von Ingo Sonder aus Freiburg i. Br.

Würzburg 2010

Eingereicht am:

1. Gutachter:

2. Gutachter:

der Dissertation

1. Prüfer:

2. Prüfer:

der mündlichen Prüfung

Tag der mündlichen Prüfung:

Doktorurkunde ausgehändigt am:

Sonder, I. (2010): Non-Newtonian Properties of Magmatic Melts. Dissertation Univ. Würzburg, 100 S., 22 Abb., 5 Tab.

Zusammenfassung

Die vorliegende Arbeit beschreibt eine neue Methode zur modellunabhängigen Messung von Viskositäten bei hohen Temperaturen. Viele der Mechanismen, welche vulkanischer Aktivität zugrunde liegen, werden stark durch die viskosen Eigenschaften der beteiligten Materialien beeinflusst. Die eruptierten Materialien – zum überwiegenden Teil Silikatschmelzen – sind bei Eruptionstemperatur nicht komplett geschmolzen. Deshalb sind Gleichgewichts- und Nichtgleichgewichtskristalle in den betrachteten Systemen vorhanden. Um diese Inhomogenitäten in objektive Materialparameter einzubeziehen, basiert die vorgestellte Viskositätsmessung auf auf einem Rotationsviskosimeter in einer "wide gap"-Anordnung. Die Spaltbreite zwischen den beiden konzentrischen Zylindern wurde so groß wie möglich gemacht um Inhomogenitäten zu berücksichtigen. Die aufkommenden Schwierigkeiten bezüglich der modellunabhängigen Bestimmung der Viscositäten aus den gemessenen Daten wurden mit einer geeigneten Interpolationsmethode gelöst.

Mit dieser Methode wurden die Viskositäten eines, für die Mehrheit vulkanischer Eruptionen auf der Erde typisches Material gemessen: eines kontinentalen Basaltes aus Billstein (Rhön, Deutschland). Die gemessenen Viskositäten zeigen bei konstanter Temperatur eine starke Abhängigkeit von der Deformationsrate. Dies überrascht, da basaltische Schmelzen bis heute bei vergleichbaren Temperaturen als Newtonsche Flüssigkeiten betrachtet wurden.

Da ein nicht-Newtonsches Material, im Vergleich mit einem Newtonschen, ein deutlich anderes Relaxationsverhalten aufweist (das Newtonsche zeigt ultimativ keine Relaxation), und da ein deutliches Relaxationssignal während der Viskositätsmessung gemessen wurde, wurden die Bewegungsgleichungen der Couette Bewegung untersucht. Die zeitabhängige Spannungeverteilung in einem Material, verursacht durch eine quasi-stufenartige Geschwindigkeitsänderung am inneren Couette-Radius (d. h. am Drehkörper des Viskosimeters) wurde betrachtet. Die Ergebnisse zeigen, dass ein Material, welches ein linear elastisches Schermodul und eine newtonsche Viskosität kombiniert – ein Maxwell-Material – das Relaxationverhalten quantitativ nicht beschreiben kann. Dies könnte als Hinweis betrachtet werden, dass die weitverbreiteten Maxwell-Relaxationszeiten nicht 1:1 von mikroskopischen Betrachtungen auf makroskopische Situationen angewendet werden können.

Abstract

This work presents a new method to measure model independent viscosities of inhomogeneous materials at high temperatures. Many mechanisms driving volcanic eruptions are strongly influenced by the viscous properties of the participating materials. Since an eruption takes place at temperatures at which these materials (predominantly silicate melts) are not completely molten, typically inhomogeneities, like e.g. equilibrium and non-equilibrium crystals, are present in the system. In order to incorporate such inhomogeneities into objective material parameters the viscosity measurement is based on a rotational viscometer in a wide gap Couette setup. The gap size between the two concentric cylinders was designed as large as possible in order to account for the inhomogeneities. The emerging difficulties concerning the model independent data reduction from measured values to viscosities are solved using an appropriate interpolation scheme.

The method was applied to a material representative for the majority of volcanic eruptions on earth: a typical continental basaltic rock (Billstein/Rhön/Germany). The measured viscosities show a strong shear rate dependency, which surprises, because basaltic melt has been, until now, assumed to behave as a Newtonian fluid.

Since a non-Newtonian material shows a very different relaxation behavior in the Couette motion compared to a Newtonian one (which, ultimately, does not show any), and a strong relaxation signal was recorded during viscosity measurements, the equations of Couette motion were investigated. The time dependent stress distribution in a material due to a quasi step-like velocity change at the inner Couette radius (i.e. the spindle) was considered. The results show that a material combining a linear shear modulus and a Newtonian viscosity – a Maxwell material – cannot quantify the relaxation behavior. This could be considered as a hint, that the widely used Maxwell relaxation times cannot be applied as a 1:1 mapping from microscopic considerations to macroscopic situations.

Acknowledgments

I want to use this place to thank Prof. Dr. Bernd Zimanowski for his always available advice. His thorough, comprehensive knowledge about the complex systems emerging in volcanology is a constant source of ideas. I also want to thank Prof. Dr. Pierro Dellino for the good cooperation and for reviewing this thesis. Also Prof. Dr. Vladimir Dyakonov is thanked for his willingness to examine this work.

Working in this interdisciplinary laboratory has been a pleasure, since it served as a pool of many ideas, pragmatic and systematic solutions of the diverse problems of volcanology. I want to thank all members of the PVL who made this possible. Special thanks go to PD. Dr. Ralf Büttner, whose experimental expertise and knowledge on physical principals proved to be very helpful. Anton Uttinger is thanked for providing rock solid and customized tools for viscometry. Manuel Hobiger is acknlowledged for his contribution to the viscometry techniques. Further, I want to thank the following laboratory members: Hermann Beyerichen, Tobias Dürig, Andrea Schmid, Rolf Seegelken, Philipp Revilak, Michael Eitel, Andrea Bossmann, and Alexander Heinz.

Apart from the laboratory I want to thank Anette, Jochen, and Josefine. Life in the Falltorgasse has been a pleasure.

Contents

Introduction

1

Processes controlling volcanic eruptions take place on time scales varying from several thousand years (10^{10} s) [54] to less than a microsecond (10^{-6} s) [16]. These huge variations are responsible for the complexity and the comparable little knowledge about volcanic systems. Volcanic eruptions are typically classified from field-, or from direct visual observation [3, 14]. Viscous properties of igneous materials play an important role in almost all eruption scenarios [54]. The only important exception are explosive volcanic eruptions driven by Molten Fuel Coolant Interaction (MFCI, [22]). This process is strong and fast enough to bring even a liquid with a viscosity comparable to water from fluid state into the brittle regime, so that dissipative properties of continuous deformation do not play a role. The violence of a volcanic eruption is strongly controlled by the conversion of heat of the magma taking part in the eruption process into kinetic energy. The transitions from continuous plastic deformation of partially molten magmatic material to elastic deformation, and finally to brittle failure at the far end of the deformation scale, are processes which determine the time scale of this energy conversion [15].

Viscous properties describe the dissipation of momentum of a material in motion due to inner friction arising from its deformation. Exact knowledge of these properties is important everywhere, where a material can be assumed to get deformed at some rigid boundary. The momentum loss due to friction takes then place in the boundary layer [see e.g. 7, 31, 51], and the thickness of the boundary layer is determined by the materials properties. In typical volcanic processes this boundary layer is large enough to cover the whole volume under consideration (the involved viscosities are typically high compared to water, which dominates the picture of a 'typical' viscous fluid). Therefore viscous properties are a vital part in the description of igneous material motion. Viscous properties in continuous media are usually described via the Navier-Stokes equations [57]. One of the material parameters taken into account, the viscosity, describes the momentum loss. Materials obeying these equations, which assume a linear dependence of viscous stress on rate of deformation, are called Newtonian materials. Materials not following this rule consequently are

called non-Newtonian materials. When dealing with highly viscous systems the question arises if one paramter for the description of momentum dissipation is sufficient, despite the aim to keep the overall description of a system as simple as possible. This question is not only academic, it rather arises from practical applications in volcanology. A good example for this question is the application of the Navier-Stokes equations to the problem of a lava flow. Calculating the velocities of the lava consists essentially of solving these equations. This is usually done numerically, since nature typically does not provide simple boundary conditions. However, one important limit of the consideration is the analytical expression describing the balance of viscous force, represented by parameter η, acting against deformation caused by the gravitational acceleration g. Assuming simple boundary conditions the lava may flow down a simple plain inclined by an angle α. The thickness of the lava layer is given by h. Figure 1 provides a sketch of this scenario. The steady state velocity of this system is then given by

$$v = \frac{\rho}{\eta} \frac{g \sin\alpha}{2} y\,(2h - y) \quad . \tag{1-1}$$

For typical measured parameters [27], i.e. $\eta \simeq 100\,\mathrm{Pa\,s}$, $\rho \simeq 3 \cdot 10^3\,\mathrm{kg\,m^{-3}}$, and $\sin\alpha \simeq 1/2$, a velocity at a flow width of 1 m of $75\,\mathrm{m\,s^{-1}}$ is calculated. This result is orders of magnitudes too large. Typical observed flow velocities lie in the range from halt up to rarely seen $5\,\mathrm{ms^{-1}}$. Larger velocities can be observed only during explosive eruptions. There, fragmentation processes produce big and small particles travelling as 2-phase flows, or as single particles on ballistic trajectories [15, 35, 62, 63]. It is also documented [9] that the Newtonian model fails to describe the often observed behavior of a lava flow to 'hang' at a slope. That means, the velocity almost vanishes — the flow jams. To describe this behavior using the measured heat conductivities [17], a Newtonian viscosity needs to have a value of $10^5\,\mathrm{Pa\,s}$. Measured Newtonian viscosities are more than 3 orders of magnitude lower. It was also shown numerically [9] that boundary conditions as e.g. the finite length of a flow or confinement at the flow sides do not alter this result significantly. The large number of components in a magmatic melt leads to a temperature range in which a part of these components is molten, and other components are still solid. There are various (mostly thermodynamic) calculations [e.g. 24] and measurements investigating solid and liquid states of these

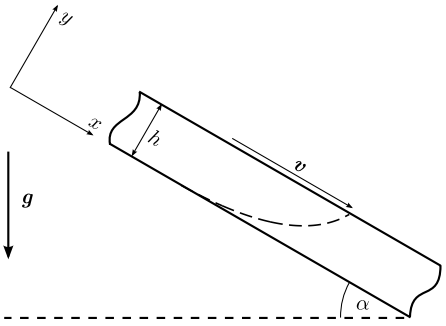

Figure 1.1: *Simple lava flow. The curved, dashed line in the flow indicates the velocity profile.*

components . Other research also shows that non-equilibrium effects of crystallization and remelting strongly depend on cooling and heating rates, not only on absolute temperatures [34, 60]. Therefore it is not possible to describe the dynamic behavior in complete detail. On the other hand, because the number of these effects is large, all of them will be effective at once, non of them alone, as dominating process. In such a case it seems reasonable to describe the material as quasi-continuum. The minimum scale to which this description can be applied is then set by the condition that the largest inhomogeneities must still be much smaller than the minimum scale. Material properties derived from these assumption will not be as simple as for, say chemically 'pure' materials. The presence of a melting region instead of a melting point is just one consequence.

Besides the meaning for material deformation, viscosity has been widely used to relate microsopic models via thermodynamical processes to macroscopic, mechanical observables [49]. The ratio of viscosity and a materials elastic modulus defines the maxwell relaxation time [e.g. 38], which is related to various propabilities of change of states of a material. Thus, knowledge of viscosity is necessary to verify microscopic models of many macrosopic observables. For Newtonian materials viscosity is independent of rate of deformation, and so the relaxation time is a material constant (as long as the elastic modulus is a constant). In the case of a non-Newtonian material the relaxation time is not a material constant but consists of at least one material function leading to a spectrum of relaxation times.

Systematic measurement of viscous properties of volcanologically relevant materials started in the late 60s of last century [see e.g. 41, 43, 53]. Since that time it has been a constant topic of discussions. Besides technical difficulties of viscosity measurement, arising from high temperatures and inhomogeneities of various kinds, and the development of some rather exotic measurement techniques [45], the characteristic dependency of shear stress on deformation rate has been a strongly stressed point. The first measurements assumed Newtonian fluid models even though the measured flow curves were not linear. The non-linearity was claimed to originate from viscous heating [53]. Later a yield stress was introduced into the measurement procedures [46], which for some highly viscous, igneous melts were then replaced by a non-linear relationship between stress and deformation rate [12, 59]. Melts with comparable low SiO_2 content today are assumed [47] to show Newtonian behavior, except the melt has a very high crystal content ($\geq$ 30%). This assumption however, has never experimentally been validated. A class of volcanic material with a low, i.e $\leq$ 55 wt.% SiO_2 content are basaltic melts. Numerical simulations of lava flows have been using non-Newtonian rheology since the last decade [19–21, 25, 42]. They introduced the Bingham fluid to lava rheology. Named

after E. C. Bingham, who introduced [10] this model of a flow curve as a first, pragmatic approximation to a more complex description of friction in fluids. Analogously to friction between solid bodies the Bingham model assumes zero shear rate below a critical shear stress, the so-called yield strength. Above the yield strength the material is assumed to show a linear flow curve. In search of more accurate models, research in the 1980s showed, that there is no reasonable way to reproducibly measure its value [5, 6] — the yield strength does not really exist. Therefore the Bingham model is not suitable as a base of flow curve measurement. The determination of the relation between deformation rate and shear stress, should be as transparent as possible, and as independent of models as possible. Various different constitutive equations, i.e. types of flow curves, have been developed [e.g. 11, 36]. After a correct measurement it is possible to set up a suitable approximation of a flow curve that fits to further applications.

The aim of this work is to provide a method to measure the flow curve of magmatic melts making as few assumptions as possible about the constitutive equation. Only if it is possible to determine, besides the quantitative measurement of the flow curves parameters, its qualitative structure, the result will be useful for further applications.

Material: In order to establish this method a suitable material needs to be selected that represents a large class of volcanic activities. A continental flood basalt at Billstein hill in the volcanic field Rhön/Germany, satisfies this condition. There is nothing special about this basalt except that some of its properties have already been measured [61] and the general behavior is known from daily work in the laboratory. The chemical composition is listed in appendix B.2.

The content is roughly devided into three parts. Chapter 2 introduces principal properties of the considered flows and materials, which are used in the following of the document. Chapter 3 derives the experimental method of flow curve measurement, and presents first results of test materials and of the application to the 'real world' material Billstein Basalt. Chapter 4 finally investigates the transient behavior of the considered material regarding the Maxwell relaxation times formalism, and consequences from the measured non-Newtonian viscosities. The results of the viscosity measurements and the measurement of the rate of deformation at brittle fragmentation were published in the Geophysical Research Letters [56] and the Journal of Geophysical Research [15], respectively. The publications can be read in appendix D.

Deformation and Stress

2

The following treats magmatic materials as quasi continuum. To account for inhomogeneities, which are assumed to be small enough so that a reasonable averaging can be achieved, a more general friction behavior, compared to the linear Newtonian assumption, is explicitly allowed. The resulting bulk properties can be more complicated as can be seen at e.g. the properties of polymer solutions. Physical effects taken into account in this description are:

1. Mass density ρ. As long as no gaseous phase is present besides the two other phases, it is reasonable to assume ρ as constant in space and time. The temperature dependence of ρ is reasonably well known [30, 43].

2. Elasticity. Describes the ability of a system to recover some initial state after being forced to move out of it. Deformation due to elastic properties conserves a systems total energy. Elasticity will be denoted by its modulus M.

3. Material internal friction η. Describes the effect of energy and momentum loss due to material deformation. In many simple materials η can be approximated by a constant of material motion. For other materials, though very homogeneous, η must be determined empirically for every state of motion by a material function. In some cases it might not even be possible to determine a viscosity.

A gaseous phase which is probably present during a magmatic eruption must be neglected here due to its high dependency on pressure states and buoyancy effects. The description of material motion assumes a non-porous, incompressible, homogeneous material. The well established equation for conservation of mass $\partial\rho/\partial t + \operatorname{div}(\rho\boldsymbol{v}) = 0$ [31], in which $\boldsymbol{v}$ is the velocity of a material point, yields the equally well known condition of material incompressibility

$$\operatorname{div}\boldsymbol{v} = 0 \quad .$$

Conservation of momentum in a continuous, inviscid material leads to the Euler equation

$$\dot{\boldsymbol{v}} = -\frac{1}{\rho}\operatorname{grad} p + \boldsymbol{g} \quad ,$$

where p is the isostatic pressure and $\boldsymbol{g}$ represents the gravitational acceleration. The left hand side is the total derivative, or the so called material derivative of velocity $\boldsymbol{v}$. In order to include effects of momentum dissipation one can expand a – yet unknown – momentum term, representing energy dissipation in a material, into first order of spatial velocity gradient [31]. The condition that this description must be independent of the frame of reference leads to the Navier-Stokes equations

$$\dot{\boldsymbol{v}} = -\frac{1}{\rho}\operatorname{grad} p + \frac{\eta}{\rho}\triangle\boldsymbol{v} + \boldsymbol{g} \quad . \tag{2-1}$$

η is called viscosity and results as the first order parameter from the expansion. The right hand side can alternatively be written with help of a stress tensor S

$$\dot{\boldsymbol{v}} = \frac{1}{\rho}\operatorname{div}\mathsf{S} + \boldsymbol{g} \quad . \tag{2-2}$$

S contains here the isostatic pressure p as well as the terms of the velocity gradient and viscosity.

The application of this formalism is possible, but implies a) the existence of material functions connecting the dissipative material character in S and the velocity gradient, and b) the existence of the material functions first derivative with respect to the deformation gradient. Then the first derivative represents a linear approximation of dissipation at small velocity gradients and defines the so called 'Newtonian' viscosity. To extend this formalism to higher terms of the velocity gradients time derivative [50], it is necessary to increase the number of experimental determined parameters significantly, for various flow symmetries. Such methods were not able to produce reasonable results for many materials which are known not to follow the Navier Stokes formalism [52].

An alternative to expansion into higher terms of velocity gradient is to assume certain symmetries of a material motion. Examples of different types of motion are translation, rotation, extension, or shear. Each type of motion possesses comparably high symmetry properties, and therefore corresponding material properties can be verified quiet well. In particular the motion in a rotational viscometer can be identified with a simple shear deformation. This assumption enables one to solve the Navier-Stokes equations (2-1) analytically. An empirical verification in chapter 3 however will show that the linear dependency of material stress due to inner friction proposed by equation (2-1) is not a good approximation. On the other hand this simple deformation type allows to verify more complicated material properties. Since equation (2-2) denotes the material stress implicitly, it is suitable for a more general material description. The disadvantage of this method is the reduced applicability of measured

material parameters. Material properties measured under this conditions and with these assumptions are strictly speaking only valid for the assumed type of motion. For application to scenarios in volcanic processes, however, the shear motion is a very important (probably the most important) type of deformation.

The movement of a material element with coordinates $\mathrm{d}x^i$ at time t is commonly described by a transformation from the elements coordinates $\mathrm{d}\tilde{x}^k$ at some reference time t_0. Material motion can always be described as a combination of rotation motion, in which relative material positions are preserved (an antisymmetric operation), and a deformation motion which describes the rest (a symmetric operation). The symmetric part of material motion describes only material deformation. It is given by the so called Cauchy-Green strain tensor

$$c_{ik} = (f^T)_{ij}\, f^j{}_k = g_{lj}\, \frac{\partial x^l}{\partial \tilde{x}^i}\, \frac{\partial x^j}{\partial \tilde{x}^k} \quad . \tag{2-3}$$

Here g_{ik} denote the components of the metric tensor. A measure for rates of deformation can be derived in an analogous way. The deformation rate tensor reads

$$d_{ik} = \frac{1}{2}\left(\dot{f}_{ik} + \dot{f^T}_{ik}\right) = \frac{1}{2}\left(v_{i;k} + v_{k;i}\right) \quad , \tag{2-4}$$

where $v_{i;k}$ denotes the covariant derivative of the velocity's i-th component with respect to the k-th coordinate. Both definitions 2-3 and 2-4 are derived in more detail in appendix A.1.1.

Shear Motion 2.1

As stated in the introduction it is necessary to make reasonable assumptions about some qualitative properties of the motion. Consequences from these assumptions are inherent to the system, and the quality of these assumptions can only be verified by empirical observation. The simple shear motion is given in orthogonal coordinates, i. e. $g_{ik} = g_{ii}$ is diagonal. Furthermore all velocity components are assumed to vanish except of one, say v^2, which is assumed to depend on only one coordinate which is not the direction of deformation, i. e. x^2. The assumptions can be written as

$$\begin{aligned} v^1 &= 0 \quad , \\ v^2 &= v(x^1, t) \quad , \qquad\qquad g_{ik} = g_{ik}(x^1, x^3) \quad . \\ v^3 &= 0 \quad , \end{aligned} \tag{2-5}$$

Appendix A.1.1 shows, that then the physical components C_{ik} of the deformation tensor c_{ik} depend only on one parameter γ: $C_{ik} = C_{ik}(\gamma)$. In cylindrical coordinates, which are conveniently related to the cartesian system by

$$\begin{aligned} x^1 &= r \quad , & x^2 &= \phi \quad , & x^3 &= z \quad , \\ x &= r\,\cos\phi \quad , & y &= r\,\sin\phi \quad , & z &= z \quad , \end{aligned}$$

γ is written as

$$\gamma = r\,\frac{\partial \phi}{\partial r} \quad . \tag{2-6}$$

Physical components of the deformation rate tensor D_{ik} analogously depend only on the shear rate $\dot{\gamma}$, $D_{ik} = D_{ik}(\dot{\gamma})$. $\dot{\gamma}$ is given by

$$\dot{\gamma} = r\,\frac{\partial \omega}{\partial r} \quad , \tag{2-7}$$

where $\omega = \dot{\phi}$.

2.2 Stress Tensor of Shear Motion

The dissipative part of stress S in equation 2-2 is physically related to the rate of deformation. Possible elastic effects are related to states of deformation. Therefore it is reasonable to assume $\mathsf{S} = s_{ik}(\gamma, \dot{\gamma})$. Appendix A.2 derives further details of the s_{ik} from symmetry properties. In general the shear motion allows the s_{ik} to depend on four material functions. This functions have various different definitions, since they can be distributed over five non-vanishing elements of s_{ik}. They will be denoted as $p, \tau, \mathcal{N}_1$, and $\mathcal{N}_2$. Three of them, the pressure p and the two Normal Stress Differences $\mathcal{N}_1$ and $\mathcal{N}_2$, emerge in the diagonal elements s_{ii}. The first Normal Stress Difference $\mathcal{N}_1$ is responsible for the Weissenberg Effect [11], also known as rod climbing of a material. Its magnitude is typically more than 100 times smaller than the shear stress τ which is found in the off-diagonal elements of S. Effects of the second Normal Stress Difference are rarely known and there are only few materials for which there exist estimates of its magnitude. Therefore $\mathcal{N}_1$ and $\mathcal{N}_2$ will be neglected in the following. The stress tensor is then of the form

$$s_{12} = s_{21} = \tau \quad , \quad s_{11} = s_{22} = s_{33} = -p \quad , \quad \text{others:} \quad 0 \quad . \tag{2-8}$$

A further assumption is that the direction of $\boldsymbol{g}$ is anti-parallel to z. This restricts the motion to the so-called Couette flow. Calculation of physical components of $\operatorname{div}\mathsf{S}$ (see appendix A.3) and application to the equation of motion (2-2) yields the following relation between motion ω and shear stress τ in cylindrical coordinates for the Couette motion

$$\rho\, r\, \frac{\partial \omega}{\partial t} = \frac{\partial \tau}{\partial r} + \frac{2}{r}\,\tau \quad . \tag{2-9}$$

This result makes no assumptions about the explicit dependency of material functions p, τ on flow states $\gamma, \dot{\gamma}$. It can be used for further specializations as e.g. in chapter 3 assuming a time independent velocity. Then the flow curve $\tau(\dot{\gamma})$, the dissipative part of the shear stress, can be measured experimentally. In chapter 4 an explicit model is assigned to equation 2-9, and the time dependent velocity is determined from the boundary value problem.

Constant Deformation 2.3

In the special case of constant angular velocity $\dot{\omega} = 0$, the elastic property does not contribute to the stress in a material. Thus, the measurement of viscous properties, as described in chapter 3, is carried out at constant angular velocities. The experimental method used is that of a rotational viscometer, where a material is sheared between two rotating cylinders. The corresponding radii of the inner and outer cylinder will be called R_i and R_o, respectively, in the following. Using these assumptions, the relation between motion and stress – equation (2-9) – is time independent and decoupled. This means, for a suitable boundary condition, the material function $\tau(\dot{\gamma})$ describing the momentum dissipation due to inner friction, is then determined completely.

Viscometry

3

The aim of this chapter is to derive a method to empirically determine a materials viscosity character. The primary interest here is not the time dependent response behavior of a material due to applied stress or motion, though this time dependence will play a role as motivation for the next chapter. The focus lies on the state of stationary shear motion. For materials relevant to geologic processes the measured material samples should be as large as possible. The larger a sample, the more inhomogeneities can be taken into consideration experimentally. The more effects due to inhomogeneities can be measured, the more realistic, i.e. scalable, a model will become, which is based on this measurement. A samples size is limited by the experimental setup. There are many methods to measure viscosity of a material [11]. The best realization of a shear motion is achieved by a rotational viscometer. It allows measurements with comparable large sample volumes (in contrast to a, say, capillary viscometer). A rotational viscometer essentially consists of a sensor, which measures the torque applied to a rotation axis z. The setup applying the torque can vary significantly. The shear zone typically lies either perpendicular to z or perpendicular to r. In the former case an approximation of simple shear is achieved in the Cone and Plate setup (Figure 3.1 a). For a good approximation of shear motion properties, as given from equation (2-5), the cone angle α must be small, so that $\cos\alpha \simeq 1$. Then the shear rate $\dot{\gamma}$ is approximately constant over the whole gap, and thus determined by the experimental geometry only. The latter case is typically realized in the Couette geometry, where two concentric cylinders setup the deformation zone. If the finite length of the cylinders is neglected, the Couette geometry always

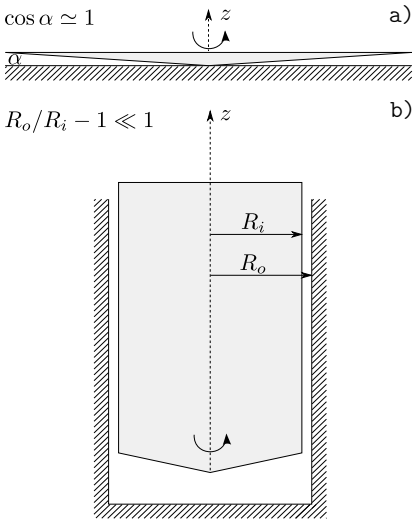

Figure 3.1: *Typical geometries of rotational viscometer setups for measurement of Non-Newtonian properties. a.) Cone and Plate, b.) Narrow Gap Couette.*

provides a simple shear motion, regardless of the gap size.

In order to simplify calculations and to reduce errors it can be realized in a Narrow Gap setup, in which the curvature of the deformation zone is negligible (Figure 3.1-b). Then, similar to the Cone and Plate case, γ and $\dot{\gamma}$ are approximately constant over the gap. The simplifying geometries are, however, difficult to achieve for large sample volumes. The Narrow Gap approximation for example, $R_o/R_i - 1 \ll 1$ where R_o denotes the crucible and R_i the bob radius, respectively, is only valid if either R_o is too large for today's laboratory scales or the gap is too small for the materials considered here. In numbers, the necessary gap size of 1 cm needs a crucible radius of not less than 1 m. This clearly exceeds scales of currently available laboratory equipment, keeping in mind that the experiment needs to be done at temperatures of $> 1600\,\mathrm{K}$. Alternatively it is possible to reduce R_i, the radius of the bob in the Couette geometry. Then the cylinder curvature cannot be neglected but the deformation is still of simple shear type. Consequently the complexity of data analysis grows significantly. However, it is still *possible* to measure viscosities within reasonable error bars. Since this method has not been used in common viscosity measurement techiques the procedure of measurement and data processing had to be reworked completely. These methods are described in the following.

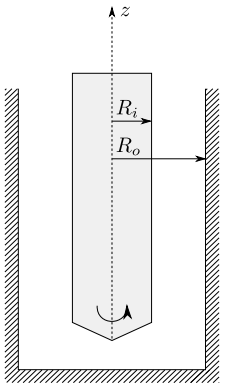

Figure 3.2: *Couette geometry, wide gap setup.*

3.1 Measurement of Shear Viscosity

The measurement of the flow curve $\tau(\dot{\gamma})$ follows the ideas of I. L. Krieger and H. Elrod [28, 29]. At the time when these analyses were published, scientific computing was almost completely done by hand. Digital computers were rare and very expensive. It will turn out that the data analysis contains a significant part of numerical effort which explains why these ideas did not become very popular. Since then times changed. The following derives the necessary analytical expressions and then shows how to discretize the measured data for numerical processing. It assumes incompressible behavior of the measured material, and the existence of a material function $\tau(\dot{\gamma})$ – the flow curve – which was motivated in chapter 2.1.

The torque N acting on the inner cylinder is related to shear stress τ by

$$\tau = \frac{N}{2\pi r^2 L} \quad , \tag{3-1}$$

where L is the length of the cylinder. The definition of the shear rate $\dot{\gamma}$ in cylindrical coordinates is given by equation (2-7). Thus one gets an expression for the angular velocity distribution between the cylinders using the inverse function of the yet unknown material function $\tau(\dot{\gamma})$

$$\omega(r) = \int_{R_i}^{r} \mathrm{d}\omega = \int_{R_i}^{r} \dot{\gamma}\,\frac{\mathrm{d}\tilde{r}}{\tilde{r}} = \int_{N/2\pi R_i^2 L}^{N/2\pi r^2 L} -\frac{1}{2}\,\frac{\dot{\gamma}}{\tau}\,\mathrm{d}\tau \quad . \tag{3-2}$$

It is always possible to calculate the inverse of $\tau(\dot{\gamma})$, since the flow curve is by definition a monotonously growing function. Now Ω denotes the angular velocity $\omega(r)$ at the inner cylinder $r = R_i$. The expression

$$\frac{\mathrm{d}\Omega}{\mathrm{d}N} = -\frac{1}{2}\left\{\frac{\mathrm{d}\tau_o}{\mathrm{d}N}\,\frac{\dot{\gamma}(\tau_o)}{\tau_o} - \frac{\mathrm{d}\tau_i}{\mathrm{d}N}\,\frac{\dot{\gamma}(\tau_i)}{\tau_i}\right\} \quad ,$$

where τ_i and τ_o are given by equation (3-1) for $r = R_i$ and $r = R_o$, respectively, is equivalent to

$$2N\,\frac{\mathrm{d}\Omega}{\mathrm{d}N} = \dot{\gamma}(\tau_i) - \dot{\gamma}\left(\frac{R_i^2}{R_o^2}\,\tau_i\right) \quad .$$

The left hand side can be summed up, scaled by the geometry parameter $\lambda = (R_i/R_o)^2$

$$\begin{aligned} 2N\,\frac{\mathrm{d}\Omega}{\mathrm{d}N} + 2\tilde{N}\frac{\mathrm{d}\Omega}{\mathrm{d}\tilde{N}}\bigg|_{\tilde{N}=\lambda N} &= \dot{\gamma}(\tau_i) - \dot{\gamma}(\lambda^2\tau_i) \\ \Leftrightarrow \quad \sum_{i=0}^{n} 2\tilde{N}\frac{\mathrm{d}\Omega}{\mathrm{d}\tilde{N}}\bigg|_{\tilde{N}=\lambda^i N} &= \dot{\gamma}(\tau_i) - \dot{\gamma}(\lambda^{n+1}\tau_i) \quad . \end{aligned}$$

Expanding $n \to \infty$, the latter part of the right hand sides of the above equations vanishes, since $\lambda < 1$. Thus the shear rate $\dot{\gamma}$ can be obtained by the measured data pairs N and Ω, while shear stress τ is obtained directly by the measured torque only:

$$\tau = \frac{N}{2\pi R_i^2 L} \tag{3-3}$$

$$\dot{\gamma} = \sum_{i=0}^{\infty} 2\tilde{N}\frac{\mathrm{d}\Omega}{\mathrm{d}\tilde{N}}\bigg|_{\tilde{N}=\lambda^i N} \quad . \tag{3-4}$$

Here the advantage of a known law for the flow curve becomes clear. For any explicit (and valid) functional dependence $\tau(\dot{\gamma})$ the sum in equation (3-4)

converges, when calculated explicitly via equation (3-2) and a more or less simple expression is obtained. It becomes, however, also clear what happens if the assumed flow curve model is too simple. Then specific features *cannot* be seen, which might be relevant for deformation behavior of a fluid. If, for example, a fluid starts from rest to some finite deformation rate, all states of deformation rate in between need to be known, not only the final state. However, without any further assumption about the relation $\Omega(N)$ it is not possible to proceed from this state of analysis. Since $\Omega(N)$ is written as a continuous function in equation (3-4) the quality of the interpolation method relating the descrete measured data pairs to the continuous function Ω is responsible for the result. The most neutral way to interpolate between measured points is a simple linear interpolation. Since this is a lot of similar, but not absolutely standardized work, a small numerical program was written to ease the data processing. The program takes measured torque and frequency data and provides user interfaces where necessary to control the process. A detailed description is given in chapter 3.3. Closely related to the above discussion is also the in the introduction mentioned question of a possible existence of a yield stress. The significant effort in the late 1980's to the early 1990's to develop a measurement technique to reproducibly extrapolate a flow curve $\tau(\dot{\gamma})$ to a possible finite value of τ at $\dot{\gamma} = 0$ was not successful [6]. It was shown that a material (e.g. 6 % iron oxide dispersed in mineral oil [44]) which changes viscosity by a factor of 10^5 in a range of applied shear stress between 0.7 Pa and 3 Pa has a finite viscosity at low shear rates and a continuous transition. The more accurate the measuremen is, i.e. the lower the minimum shear rate is, the lower is the extrapolated yield stress.

The considerations above are only valid for very long cylinders, for which effects of finite lengths are much smaller compared to the torque due to the motion independent on the vertical coordinate z. This complication is another example how an explicit assumption of the flow curve would significantly simplify the calculation, but on the other hand will have a significant implicit influence on the result, which is not easy to quantify. The measured torque consists of two parts

$$N = N_c + N_0 \quad ,$$

where N_0 denotes the torque caused by the end effect, and N_c the torque caused by cylindrical symmetric (z-independent) shear flow. The aim, to measure only N_c, can be approximately achieved in the limit of large distances of the spindles end from the crucible bottom. Then N_0 does not depend on z, and the difference of two measurements with same angular frequencies but different immersion

depths (N_{long}, N_{short}) does not depend on N_0:

$$\begin{aligned} N_{long} - N_{short} &= N_{c,long} + N_0 - N_{c,short} - N_0 \\ &= N_{c,long} - N_{c,short} \quad . \end{aligned}$$

It should be noted that the melt level in the crucible varies significantly due to the different immersion depths. If L_0 denotes the height difference of the spindle between long and short immersion depths in a laboratory coordinate system, the difference in the fluid covered length L of the spindle is

$$L = \frac{L_0}{1-\lambda} \quad . \tag{3-5}$$

For the experiment the squared ratio of the two radii λ is of great importance. Besides the high temperatures which are a constant source of noise, and therefore must be taken care of throughout the whole calculation of errors, λ is present explicitly in equation (3-4) and implicitly in equation (3-3) via (3-5). To minimize errors the exact control of λ and it's temperature dependence is very important.

Viscometer and Measurement Procedure 3.2

The viscometer is a Searl type instrument, i.e. the rotating parts are its axis and the spindle, the crucible stands still. It consists of a Haake M5 sensor, which applies a constant angular velocity Ω and measures the torque N on the rotation axis. The rotation axis is connected to rotating spindle which couples to the fluid in the crucible. There are two joints built into the rotation axis. This construction provides a self centering mechanism for small deviations of the spindle from the central position in the crucible. It will not interfere with the measurement as long as the joint angles α are small, i.e. $\cos\alpha \simeq 1$. Figure 3.3 gives a short overview of the experimental setup. The range of angular velocities which can be applied lie between $\Omega = 5.2\,10^{-3}\mathrm{s}^{-1}$ and $52\,\mathrm{s}^{-1}$. Since the rotation axis not only experiences the mechanichal torque of the measurement, but also the thermal gradient between room temperature and measurement temperature, it is made of a Al_2O_3 ceramic, which provides a very low thermal conductivity as well as a well known thermal expansioncoefficient, and a very low heat capacity. The crucibles are also made of this material. It provides good wetting properties for the melt-crucible interface in combination with chemical stability. The spindle consists of a high temperature steel with a melting point of about 1400 °C, which provides good mechanical coupling to the measured material.

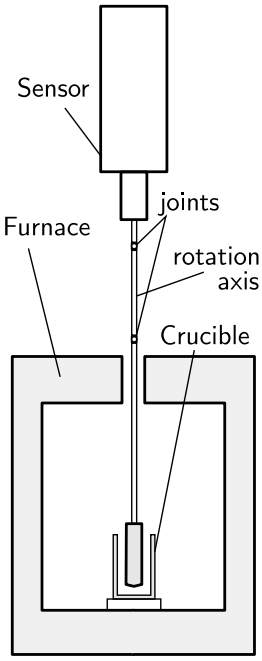

Figure 3.3: *Viscometer-furnace connection.*

Thus slip effects, which are very important for viscometry of polymers [4], can be neglected. As already discussed the geometry of the deformation zone is of Couette type. To minimize the end effect right from the start the cylindrical walls of the spindle were designed as long as possible.This construction maximizes the contribution from the ideal cylindrical flow to the total torque. The radius sizes of spindle and crucible were taken from former measurements in the laboratory [17, 61]. The dimensions in combination with the applied angular velocities yield shear rates, which cover the most important ranges observed in nature. These former measurements were carried out in a standardized DIN 53019 setup [18], which also provides a wide gap in a Couette motion. The setup was designed to measure Newtonian viscosities and so was the end of the spindle. This way it is possible to determine viscosity without measuring twice at each velocity — however only by employing the Newtonian material assumption. The crucibles in use have a diameter of about 5 cm. The diameter of the spindle is about 1 cm. This geometry yields a factor $\lambda = 0.04$ measured at room temperature. The procedure of experiment starts with centering the torque sensor above with the crucible in the furnace. Then the crucible is filled with about 150 g of the Billstein material and heated up to 1350 °C. It turned out that the best and most reproducible result is achieved, when the melt has enough time to "equilibrate" at this temperature, that means if it stays at this temperature for about 12 hours (typically over night). After this time torque is measured for applied angular velocities.

When changing the sensor speed the torque typically shows an overshoot before settling to its asymptotic value. The latter is then taken for viscosity determination. Figure 3.4 shoes an example of typical material response to a step-like change of sensor speed Ω. In some cases (usually at higher Ω) N shows no overshoot over the asymptotic value but approaches it from smaller values. This time dependence is quite characteristic when measuring non-Newtonian materials. It does not occur in the case of a Newtonian fluid. It was, however, not possible to figure out a characteristic rule for this dependency. A possible reason is the varying acceleration duration of the spindle. The change in Ω does not happen immediately, but is electronically controlled such, that the sensor is not overloaded. Acceleration times lie between 0.1 and 1 s. Therefore chapter 4 discusses the material response to a step-like change in Ω, including the step

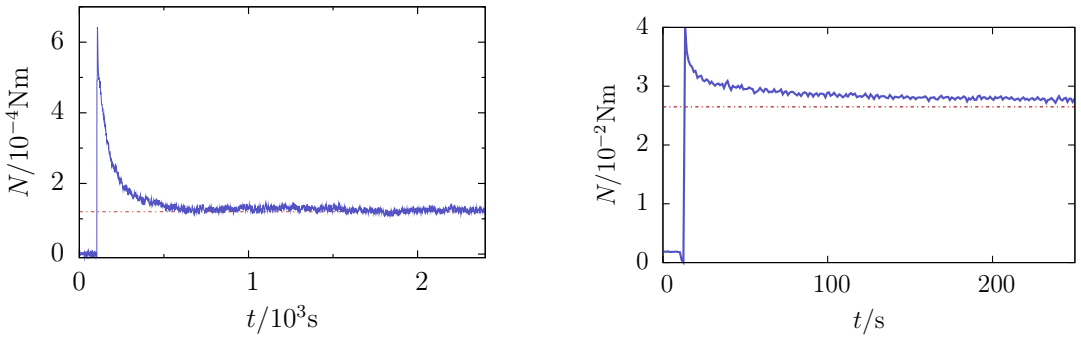

Figure 3.4: *Typical time dependence of torque signals during viscosity measurements. The red line indicates the asymptotic value to which N relaxes.*

duration. The qualitative difference between the Newtonian and non-Newtonian material response is that the Newtonian material, despite varying acceleration times does not show signifficant torque over-/undershoots.

Data Processing 3.3

To determine $\dot{\gamma}$ from equation (3-4) it is necessary to evaluate a function $\Omega(N)$, which is only known at several (the measured) points. A graphical representation of the approach given in the following is shown in Figure 3.6. Calculation of the shear rate given in formula (3-4) means to start evaluation ($i = 0$) of $\Omega(N)$ at a measured point, say the j-th point (Ω_j, N_j). For the next term of the sum $\Omega(N)$ needs to be evaluated at $N = \lambda N_j$ which probably does not coincide with a measured data pair. Thus it is necessary to interpolate between the (Ω_j, N_j). In order to stay as model independent as possible (e.g do not explicitly assume a curvature of the flow curve, since this already implies a certain model), a simple linear interpolation is the only reasonable method. The interpolation of the derivative at measured points needs some extra attention. Between the (Ω_j, N_j) the derivative is given by the slope of the interpolation lines. Since the slope at measured points is not continuous, the average values of slopes at the neighbour points of lower and higher N, respectively, is taken. This rule has significant impact on the result, since the first term of sum (3-4), which is the largest contributor to the sum ($\lambda^0 N = N$), will always hit a measured point. Interpolation between the lowest velocity and the origin is also realized as linear dependency. From $\Omega = 0$ up to, but not including, the lowest velocity,

the material is thus assumed to have Newtonian properties. After an initial step in velocity, when starting from rest or changing from a before measured finite speed, the torque data show a strong dependency on time before asymptotically approaching a steady state value (see the preceding section 3.2). The reason for this dependency will be analyzed in chapter 4. It is of importance here since the time intervals to be analyzed need to be selected manually. The strange mixture of simple experimental facts and non-standard data evaluation made it necessary to write a small program, which simplifies and partially automates this process. This program is called `VC` and is written in Java to gain a maximum of compatibility. It is pragmatically divided into the following parts, which provide the necessary features. Each part is realized as an own Java class. The work flow is sketched in Figure 3.5. The chronological flow is as follows (the terms after each item are the names of corresponding classes or methods):

- Selection of time intervals in which the measured torque was constant.
  `VC_Frame`
- Calculation of average values for each spindle speed of $\Omega,\ N,\ T$.
  `UtilsCollection.average`
- Calculation of torque differences for the two immersion depths.
  `UtilsCollection.torqueDiff`
- Actual calcultation of $\dot{\gamma}$ and τ and corresponding errors.
  `VCCal`

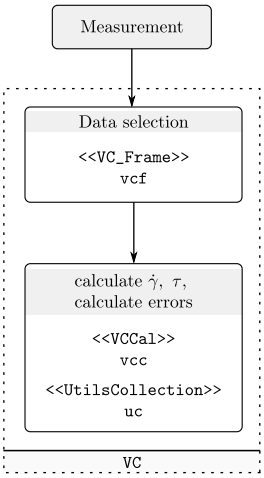

Figure 3.5: *Workflow for data evaluation.*

While the calculation of τ is straight forward from equation (3-3), the sum (3-4) for $\dot{\gamma}$ is written as a loop that aborts, when its relative change compared to the previous iteration is less that 10^{-8}. A visualization of this central part of the calculation is given in Figure 3.7. Since the measurement happens at temperatures between 1448 K and 1673 K a direct measurement of the geometry at temperature of experiment is not possible. Therefore crucible and spindle sizes were determined at room temperature, and corrected with the help of thermal expansion coefficients. At this stage of development these data are hard coded into `VC`. The comparable strong dependence of the steel spindle's radius on temperature yields a (comparable) strong dependence of λ on T. This is one of many points that shows the importance of an exact control of temperature in the furnace. Above the largest measured velocity the curve is

assumed to have the same slope as between the largest two measured data pairs (i.e. assumption of a Newtonian model outside the measured range).

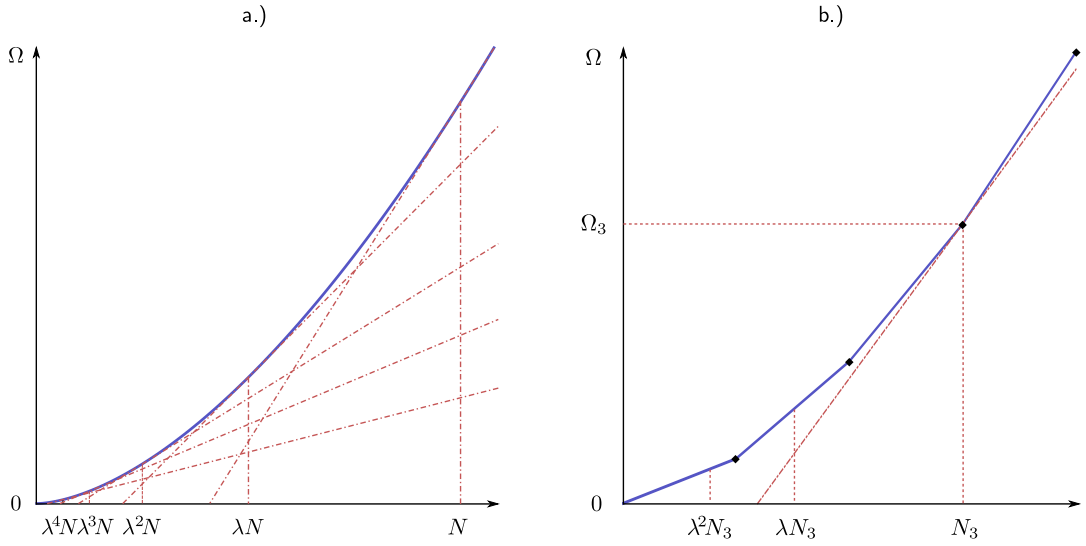

Figure 3.6: *Method of data evaluation. For demonstration a flow curve $\tau \sim \dot{\gamma}^{1/2}$, and $\lambda = 1/2$. a.) Ideal evaluation points/values for a continuous flow curve. b.) Approximation for a finite number of real measured data.*

Figure 3.8 shows strongly shortened the interdependence of data flow between the most important classes. As already stated the central position is taken by class `VC_Cal`. Input of experimental parameters – except measured time intervals – are handeled by class `ViscoCalcParams`, which also initializes the main user interface `VC_Frame`. `VC_Frame` provides an input interface for time intervals, the input and output file/folder selections and the "go"-button to start the calculation. Classes drawn at the left side provide the user interface. `VC_Cal` in the middle leads through the calculation. At the right side the class `UtilsCollection` provides methods and fields, for which it turned out that a separate class would be handy. Modules providing error calculation were not drawn into the graph.

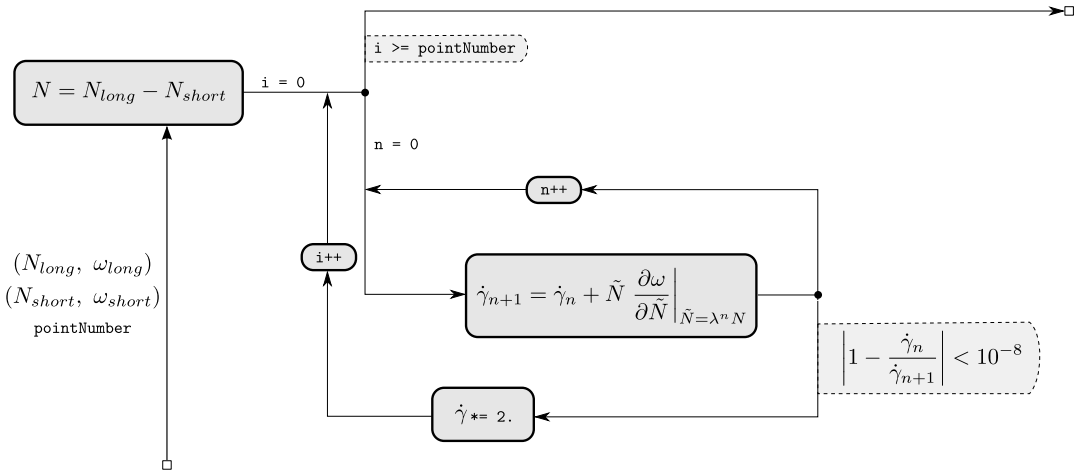

Figure 3.7: *Numerical implementation of equation* (3-4)*. Boxes with a dashed border illustrate under which conditions data flow in the referring branch, after a branch point, here illustrated with a dot. The two squares show the entrance and exit point, respectively.*

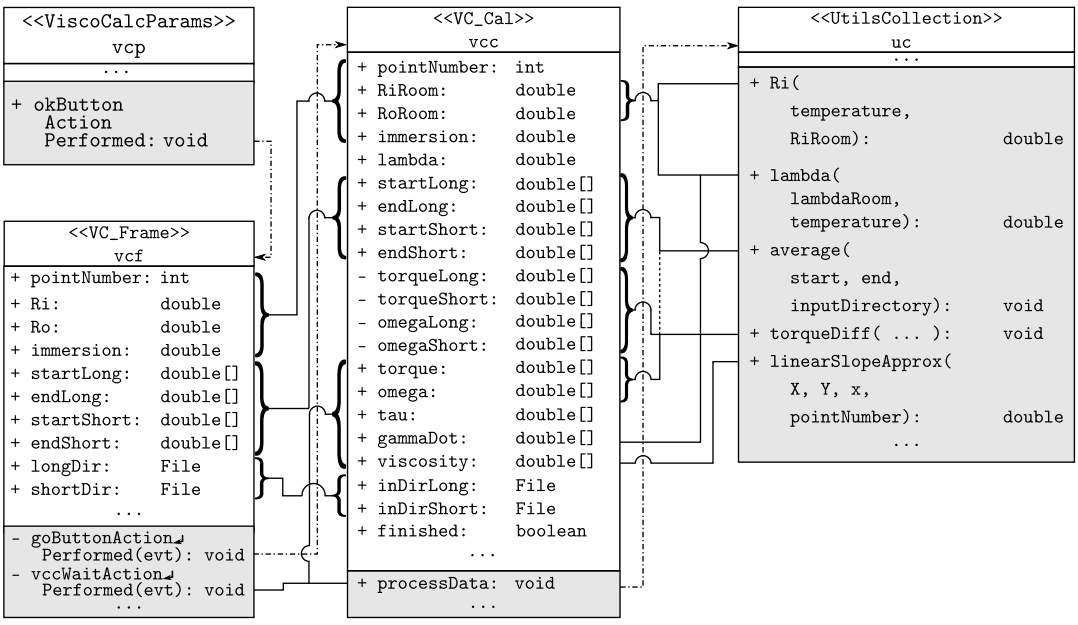

Figure 3.8: *Overview of the structure of VC. A box represents a class with its prototype and name in the top part. The middle part (white background) shows important variables. The lower part (grey background) contains methods provided by the class. The connection lines show, which method creates which instance of an object, or which method is responsible for variable manipulation. Plus and minus signs describe the visibility of and object, i.e. visible and invisible, respectively, for objects not belonging to the same instance of a class.*

Test 3.4

The setup was tested with two materials with known viscosities. One is a Newtonian silicon based oil called AK 10000 [58] produced by Wacker Chemie GmbH. It is normally used for calibration purposes and has an approximate viscosity of 10 Pa s at room temperature. The other is a polymer water solution. The polymer content is 0.4 weight percent. The product title of producer Ciba^{TM} is Magnafloc^{TM} 1011. Viscous properties of polymers and silicon oils highly depend on temperature. Therefore the room temperature needed to be very constant during measurement. For the silicon oil the temperature was adjusted to 20°C. Viscosity data for comparison of the polymer were taken from a publication by M. W. Liberatore et. al. [32] dealing with structures of drag reducing polymers, and measured viscosity of Magnafloc^{TM} at 25°C. Hence the test measurement was also performed at this temperature. Figure 3.9 shows the measured viscosities for the two test materials. The results are in good agreement with the reference values. The viscosity variations of the silicon oil are smaller than the errors. The strong non-Newtonian behavior of the polymer is well reproduced. The comparison with the reference fluid cannot be as good as for the silicon oil, since all measurements of non-Newtonian materials are principally less exact compared to the ones with assumed Newtonian behavior.

Results 3.5

Results of the viscosity measurement are shown in Figure 3.11. Viscosity values shown there are also listed in appendix B.3. They show a strong shear thinning behavior. The viscosities vary by a factor of 10 in the measured shear rate range, which lies typically between $10^{-2}\,s^{-1}$ and $30\,s^{-1}$. At high shear rates seems to weaken a little.

After measuring the viscosities it is now easily possible to pragmaticaly fit a function to these data. In the measured shear rate interval, this function, and its parameters, is then a very reliable measure of viscosity, despite of its pragmatic nature. Figure 3.12 shows the same viscosities as Figure 3.11, but with both

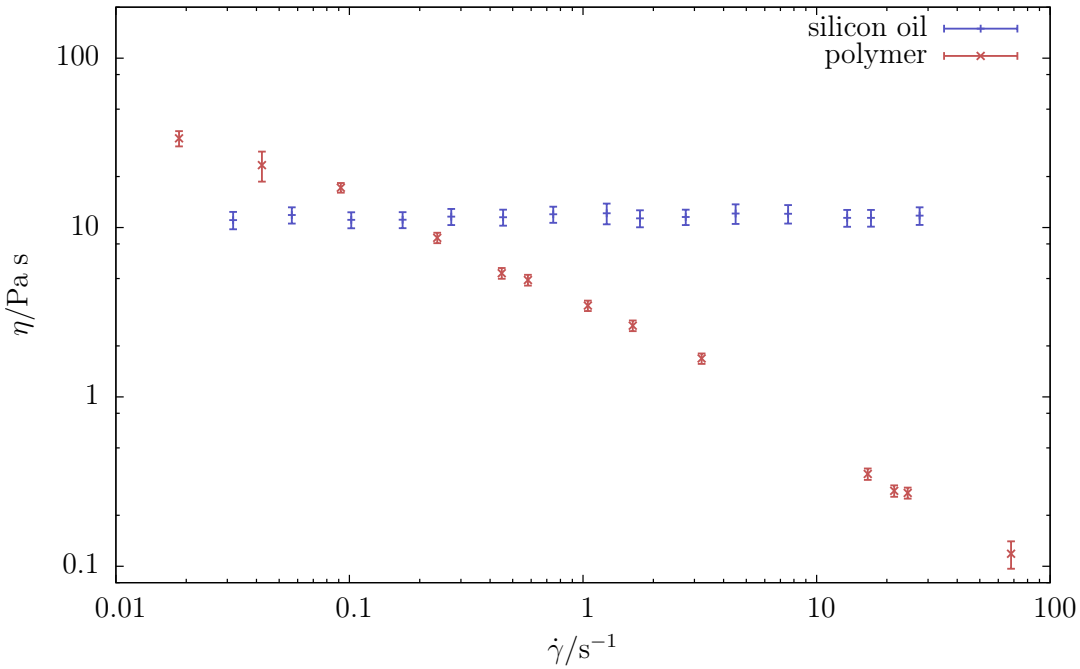

Figure 3.9: *Test of experimental setup and evaluation method. The experiment correctly measures the viscosity of the Newtonian calibration oil, as well as the strongly shear thinning behavior of the Magnafloc polymer.*

T/K	$\bar{\eta}$/Pa s^m	m
1448	209 ± 15.29	0.59 ± 0.02
1458	111	*0.59*
1473	59 ± 3.87	0.56 ± 0.02
1497	17.4 ± 1.4	0.62 ± 0.02

Table 3.1: *Viscosity fit parameters of equation* (3-6).

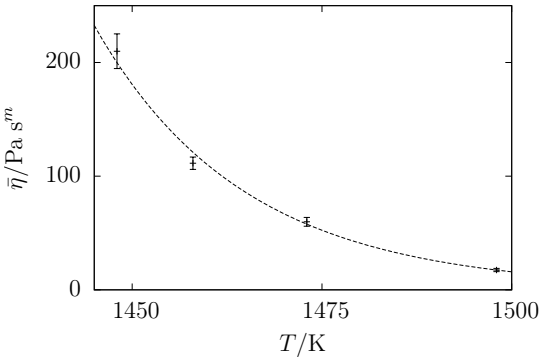

Figure 3.10: *Graph of the viscosity temperature dependency given in the table left.*

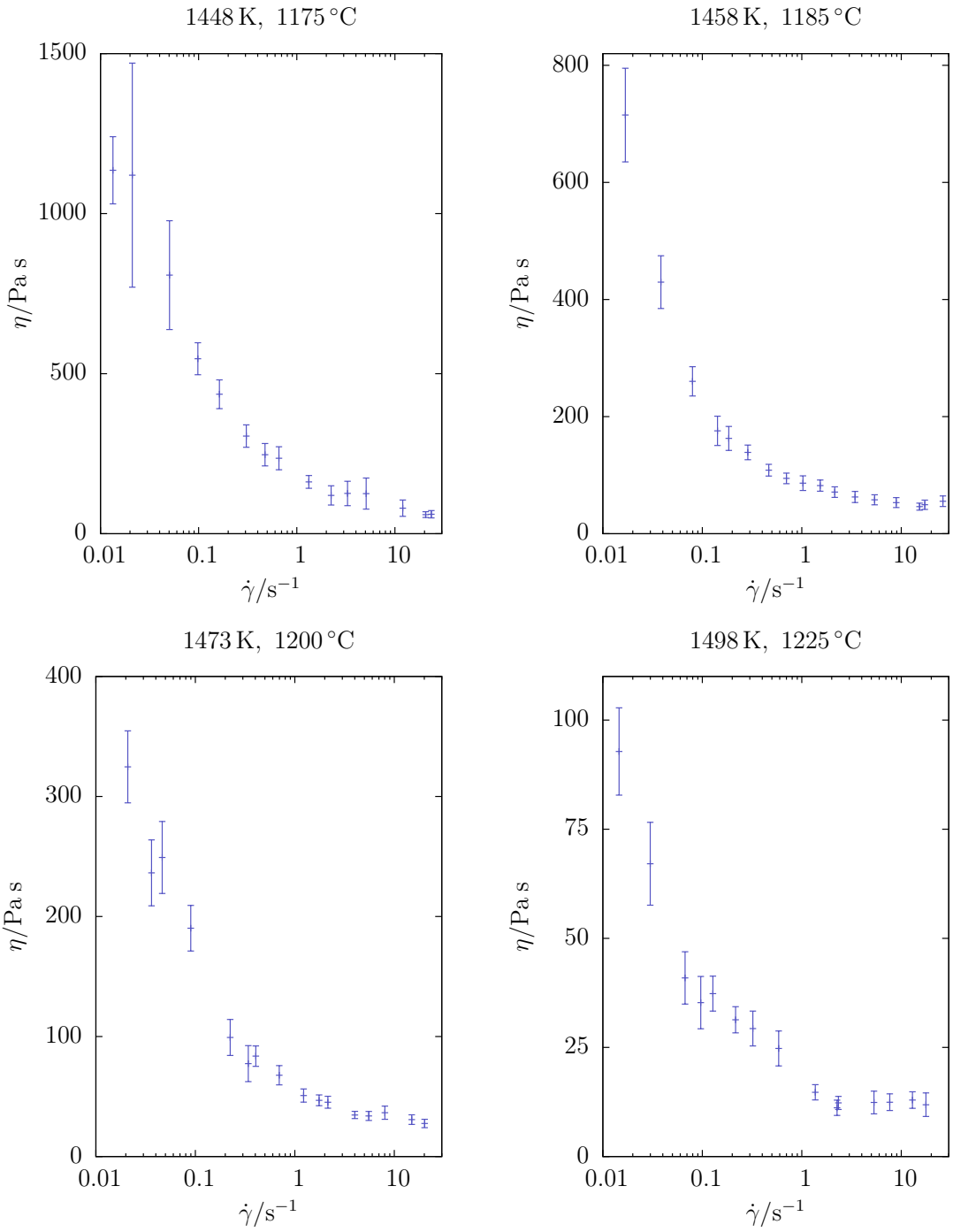

Figure 3.11: *Viscosities of Billstein Basalt at temperatures between 1448* K *and 1498* K.

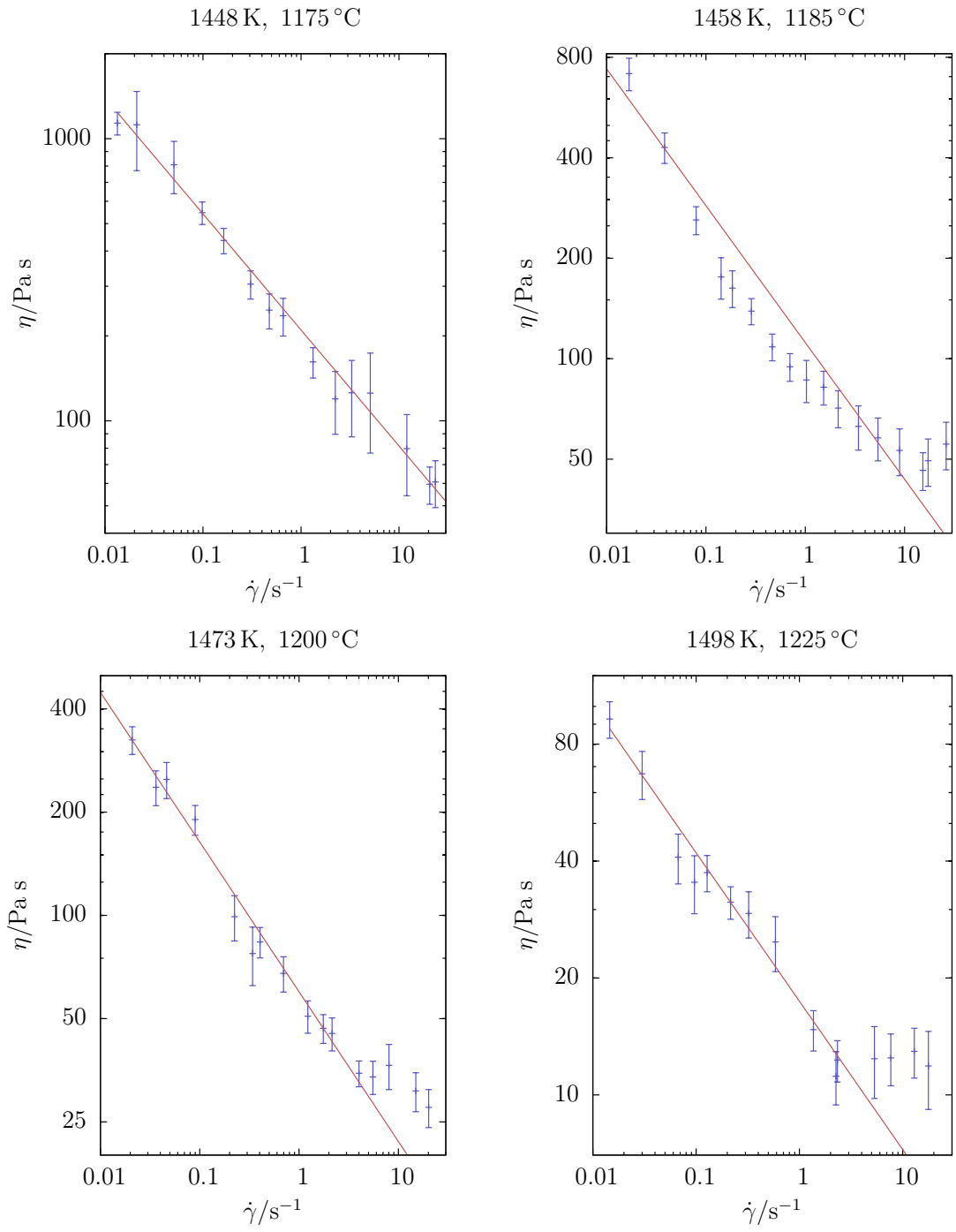

Figure 3.12: *Power law fits (equation* (3-6)*) to the measured viscosities.* m *varies between 0.56 and 0.62. The main temperature dependence is found in the proportionality constant.*

axes scaled logarithmically. The dashed lines represent best fits of a power law

$$\frac{\tau}{\tau_0} = \left(\frac{\dot{\gamma}}{\dot{\gamma}_0}\right)^m \qquad (3\text{-}6)$$

$$\Leftrightarrow \quad \eta = \bar{\eta}\ \dot{\gamma}^{m-1} \quad .$$

For 1458 K the power law index m was taken as fixed value. Then $\bar{\eta}$ agrees well with an overall smooth temperature dependence. The value of exponent m is roughly 0.6 for all the measured temperatures. Table 3.4 lists the exact values. Since m does not vary significantly over T the viscosity's main temperature dependency must ly in the proportionality factor $\bar{\eta}$. Figure 3.10 shows that this temperature dependency agrees reasonably well with an Arrhenian like exponential.

3.6 Viscous Heating

A possible side effect when working with viscous materials can be the heating of a sample due to its continuous inner friction. If a material is sheared fast enough, the produced energy cannot spread fast enough to the surrounding temperature reservoir, but it will raise the melts temperature at the point of friction. The conduction and temperature equilibration is controlled by the thermal conductivity λ. This calculation makes some simplifying assumptions in order to provide an upper limit of this temperature rise. The following two points enable a comparably simple consideration of the problem.

- The melts viscosity does not depend on the temperature. This assumption is an upper limit which neglects the strong temperature dependency of viscosity.
- In thermal equilibrium the temperatures at the boundaries, i.e. at $r = R_i, R_o$, respectively, are equal.

Furthermore a power law rheology is assumed, since an explicit rheology term is necessary.

If U denotes the inner energy, and $\boldsymbol{q}$ the heat flux through a volume element $\mathrm{d}V$, the heat conduction can be described with the following equation:

$$\frac{\partial}{\partial t}(\rho U) = -\mathrm{div}\,(\rho U \boldsymbol{v}) - \mathrm{div}\,\boldsymbol{q} + S^{ik} D_{ik} \quad . \tag{3-7}$$

The left hand side describes the change of inner energy due to the terms on the right hand side. The first of these is called convection. Since the melt is incompressible and has an approximately constant mass density, this term can be neglected here. The heat flux $\boldsymbol{q}$ can be seen as a gradient of a scalar function, which is proportional to temperature T. The last source of heat is the energy density of the fluids friction. It is described by the double contraction of the stress tensor S and the velocity gradient tensor D. Since convection can be neglected it is practical to express most of this equation in terms of temperature:

$$\rho\, c_p \frac{\partial T}{\partial t} = \lambda\, \mathrm{div}\,\mathrm{grad}\, T + S^{ik} D_{ik} \quad .$$

Here c_p is the samples specific heat capacity. For the purposes here it is enough to consider a case when T is in equilibrium and its derivative vanishes. Then equation (3-7) reduces to a pure heat conduction equation with a position

dependent source $S^{ik}D_{ik}$. From equation (2-8) S is known and the double contraction becomes

$$S^{ik}D_{ik} = \tau\,\dot{\gamma} \quad ,$$

and the heat conduction equation can be written in cylindrical coordinates

$$\frac{\partial^2 T}{\partial r^2} + \frac{1}{r}\frac{\partial T}{\partial r} = -\frac{\tau\dot{\gamma}}{\lambda} = -\lambda^{-1}\bar{\eta}^{-1/m}\left(\frac{N}{2\pi L}\right)^{1+1/m} r^{-2(1+1/m)} \quad .$$

The position coordinate can be scaled by $\bar{r} = r/R_o$, so that

$$T'' + \frac{T'}{\bar{r}} = -\underbrace{\lambda^{-1}\bar{\eta}^{-1/m}\left(\frac{N}{2\pi L}\right)^{1+1/m} R_o^{-2/m}}_{a}\ \bar{r}^{-2(1+1/m)} \quad , \qquad (3\text{-}8)$$

and the $'$ stands for $\partial/\partial\bar{r}$. This equation has a solution of the form

$$T(\bar{r}) = A\,\bar{r}^{\,\alpha} + B\,\ln\bar{r} + C \quad .$$

Two parameters can be determined immediately to

$$\alpha = -2/m$$
$$A = -a/\alpha^2 \quad .$$

As boundary conditions equal temperature at inner and outer radius, and its value, say T_0, are assumed:

$$T(\bar{r}=\delta) = T(\bar{r}=1), \quad \delta = \frac{R_i}{R_o} \quad ,$$
$$T(\bar{r}=\delta) = T_0 \quad .$$

From these conditions the two remaining unknown parameters can be determined as

$$B/A = -\frac{\delta^\alpha - 1}{\ln\delta} = -\xi$$
$$C = T_0 + (m/2)^2\,a \quad .$$

The proportionality constant a of equation (3-8) consists of material and geometry parameters and a value describing the state of the motion. This latter value can be chosen as the shear rate $\dot{\gamma}_i$ at the inner cylinder $r = R_i$. Then a becomes

$$a = \frac{\bar{\eta}}{\lambda}\,\dot{\gamma}_i^{m+1}\ R_o^2\,\delta^{2(1+1/m)} \quad .$$

The temperature distribution reads now

$$T(\bar{r}) - T_0 = \frac{\bar{\eta}}{\lambda}\,\dot{\gamma}_i^{m+1}\ R_o^2\,\delta^{2(1+1/m)}\left(\frac{m}{2}\right)^2\ \left(1 - \bar{r}^{-2/m} - \xi\,\ln\bar{r}\right) \quad . \qquad (3\text{-}9)$$

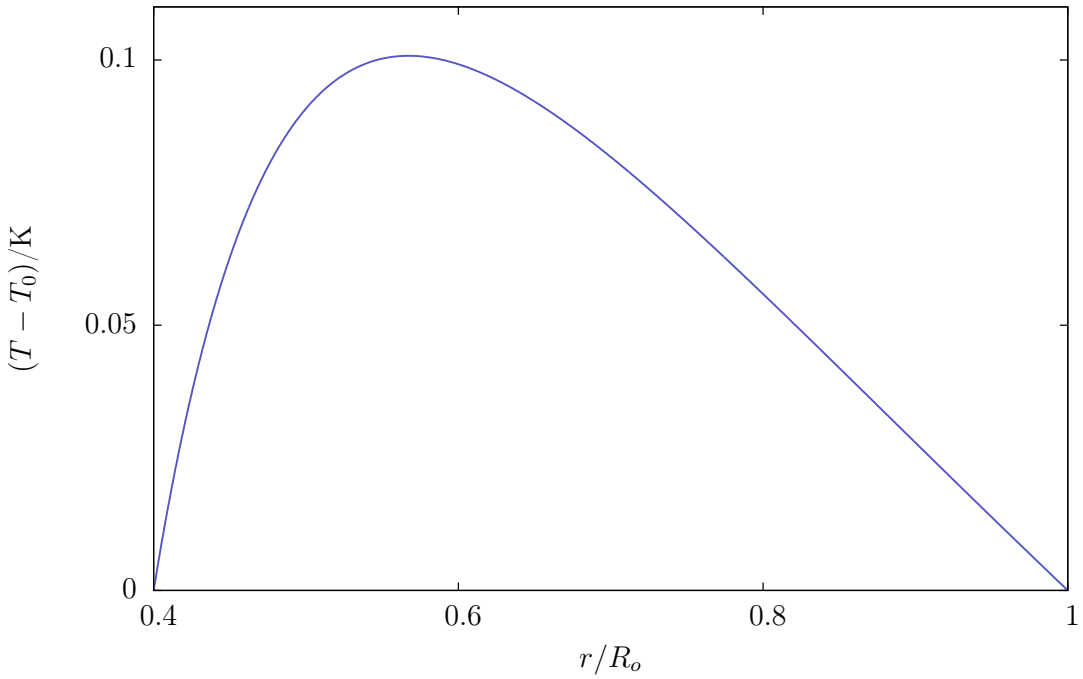

Figure 3.13: *Temperature variation due to inner friction. Material parameters are taken from Billstein material at* 1175 °C, *i.e.* $m = 0.6$, $\bar{\eta} = 200\,\mathrm{Pa\,s}^m$. *The geometry is given as* $R_i/R_o = 0.4$, $R_o = 0.025\,\mathrm{m}$. *Shear rate at the spindel was* $\dot{\gamma}_i = 25\,\mathrm{s}^{-1}$.

The radius of maximum temperature can be calculated to be

$$r_m = \left(-\frac{B}{\alpha A}\right)^{1/\alpha} = \left(\frac{m}{2}\xi\right)^{-m/2} \quad ,$$

and its corresponding temperature is

$$T_m = T(r_m) = \left(\frac{m}{2}\right)^2 a \ \left\{1 - \frac{m}{2}\xi\,(1 - \ln(m/2) - \ln\xi)\right\} \quad .$$

Figure 3.13 shows a temperature distribution (3-9). It shows the maximum temperature rise calculated from the measured data. The peak lies at about 0.1 K and hence shows that the effect of viscous heating is more than 10 times smaller compared to the error of the temperature measurement.

Material Relaxation

4

The transient behavior of a material between solid and liquid state can be described by considering a combination of viscous and elastic properties. While elasticity is a reversible process — it conserves the energy taken from deformation — the viscosity dissipates this energy, i.e. converts it to heat or changes in the materials structure. The widest known viscoelastic model is the so-called Maxwell material. It combines linear elasticity, denoted here by the shear modulus M, and a Newtonian viscosity η. The ratio of this two material constants is called the Maxwell relaxation time t_r, since James C. Maxwell used a similar ratio in 1868 in his theory of gases [40]. The model was often employed in combination with the Adam-Gibbs theory of the relaxation processes in glasses [2]. t_r determines the order of the time scale on which the material relaxes applied stress. As was shown in the previous chapter (pp. 25) the Billstein material shows significant time dependent behavior as response to a change in applied velocity. The strongest time dependency is observed when starting from rest. Though ist is difficult to reproduce exact values of this time dependence due to the experimental conditions (see section 3.2) the order of the average duration of the range of measured time dependencies is 10^2 s as response to a velocity step which took place on a time scale of 0.1 s to 1 s.

Values for the shear modulus M of ceramic materials in general lie in the range of 10 GPa − 200 GPa, for basaltic materials common values are 30 GPa − 40 GPa [8, 39]. These data were measured or calculated and refer to room temperature. There are no directly measured data on M in the solid-fluid transition region or in the fluid regime. Hence, M is usually calculated using common values for t_r, or a negligible temperature dependency of M is assumed, so that a measured value from lower temperatures can be applied [13].

Assuming a small temperature dependency of M, and combining it with the viscosities presented in the preceding chapter yields very small values for t_r: $10^{-10}\,\mathrm{s} \leq t_r \leq 10^{-7}\,\mathrm{s}$. This time scale is many orders of magnitudes to short to be a) measured using a mechanical apparatus, and b) to be comparable with the 10^2 s time scale on which the Billstein basalt material relaxes. It does not seem likely that the geometry of the viscometer apparatus, specifficaly the curvature

of the cylinder geometry due to the wide-gap setup, changes the relaxation behavior of the macroscopic sample enough to account for the huge descrepancy of relaxation behavior. However, it is not easy to estimate the interaction of material relaxation, effects of inertia, and effects of geometry in the wide-gap setup. In order to quantify these effects this chapter calculates the response of a viscoelastic Maxwell material to a quasi step-like motion at the inner Couette boundary R_i in the viscometer, taking place on the time scale t_0. Beside the linear viscoelastic material, the equations of motion are also established for a Newtonian non-elastic fluid, for a non-elastic power-law material, and for a a combined material posessing linear elastic and power-like viscous properties.

4.1 Boundary Condition

Choosing appropriate conditions describing the motion at the boundaries of the viscometer apparatus is an important part of this calculation. At the inner cylinder R_i it will be assumed that the angular velocity ω starts from rest at time $t = 0$ and accelerates in a small but finite time t_0 asymptotically to its equilibrium value. At the outer cylinder R_o the material is assumed to rest. In order to get a consistent picture, the first derivative with respect to t at $t = 0$ needs to vanish. This is accomplished by the correct superposition of two exponentials and a constant:

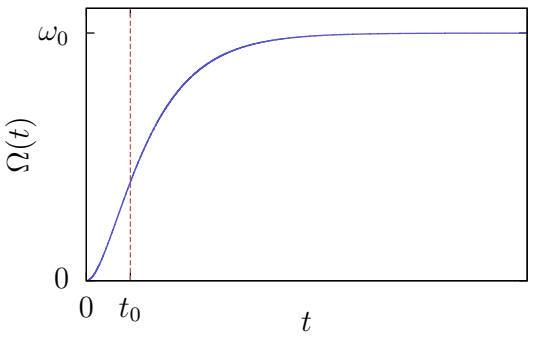

Figure 4.1: *Boundary condition at $r = R_i$: Velocity step of duration t_0.*

$$\begin{aligned} \omega(r,0) = 0 \quad , \quad \omega(R_o,t) = 0 \quad , \\ \omega(R_i,t) = \Omega(t) = \omega_0 \left(1 - 2\,e^{-t/t_0} + e^{-2t/t_0}\right) \quad . \end{aligned} \tag{4-1a}$$

Figure 4.1 gives a graphical impression of $\Omega(t)$. Initial conditions are chosen so that ω starts from 0. To stay consistent with the boundary conditions, the initial first time derivative must vanish for all $r \in [R_i, R_o]$:

$$\omega(r,0) = 0 \quad , \quad \frac{\partial}{\partial t}\,\omega(r,t)\bigg|_{t=0} = 0 \quad . \tag{4-1b}$$

Linear Viscoelastic Fluid 4.2

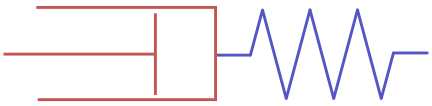

Figure 4.2: *Schematical representation of a volume element of the Maxwell material.*

To describe a material with both, elastic and viscous properties, each volume element is assigned an elastic shear modulus M and a Newtonian viscosity η. The total deformation is the sum of the partial deformation caused by elasticity and viscosity $\gamma = \gamma_e + \gamma_v$. Schematically each volume element can be seen as a combination of a spring and a dashpot as sketched in Figure 4.2. Calculation of the total stress in an element using the definitions of shear modulus $\tau = M\,\gamma$ and Newtonian viscosity $\tau = \eta\,\dot{\gamma}$ yields the stress expressed as differential equation instead of a ordinary one as in the case of a viscous material

$$\frac{\partial \tau}{\partial t} = -\frac{\tau}{t_r} + M\,\dot{\gamma} \quad . \tag{4-2}$$

The material equation is described by t_r and M. The density is not present. ρ is introduced by inserting equation (4-2) into equation (2-9) from chapter 2, derived from momentum conservation and continuity. It reads

$$\begin{aligned} \frac{\rho}{M}\frac{\partial^2 \omega}{\partial t^2} + \frac{\rho}{\eta}\frac{\partial \omega}{\partial t} &= \frac{3}{r}\frac{\partial \omega}{\partial r} + \frac{\partial^2 \omega}{\partial r^2} \quad , \quad \text{or} \\ \ddot{\omega} + \frac{\dot{\omega}}{t_r} &= c^2\left(\frac{3}{r}\,\omega' + \omega''\right) \quad . \end{aligned} \tag{4-3}$$

This equation has the form of a wave equation with a damping term $\dot{\omega}/t_r$. In the second line a wave speed is introduced by $c^2 = M/\rho$. The dots and primes refer to partial derivatives with respect to t and r, respectively.

The solution of the boundary value problem arising from equations (4-1a) and (4-3) is derived in detail in appendix A.5. It consists of the sum of two solutions: The first solution contains the amplitudes A_s, which are functions of position r. They result from a fourier transform (with frequency parameter s) of equation (4-3) and boundary condition $\Omega(t)$ (see equation (4-1a) and section A.5.1 in the appendix). This solution obeys the boundary conditions, but not the initial conditions of equation (4-1b). Correct initial conditions are achieved by adding a solution based on a separation ansatz, which vanishes at the boundaries R_i, R_o, compensates the wrong initial values of the first term,

and adds correct initial conditions:

$$\omega(r,t) = \omega_0 \Big\{ A_0(r) - 2\,A_{i/t_0}(r)\,e^{-t/t_0} + A_{2i/t_0}(r)\,e^{-2t/t_0} + \sum_{j=1}^{\infty} T_j(t)\,Z_j(r) \Big\} \quad . \tag{4-4}$$

The summation term is the separation ansatz solution. The $Z_j(r)$ form a fundamental system so that expansion coefficients can be derived to compensate the non-zero parts of the amplitudes at $t = 0$, and setup correct start values. Details of this part are shown in Appendix A.5.2. Details on numerical determination of the wave numbers q_j, on which the Z_j are based, are given in the appendix in equation (A-22)/page 64 and appendix C.3.

The stress is determined with help of equation (4-2). This is a linear differential equation of first order for the time variable. The general solution includes one integration parameter, depending on r, which is chosen, so that $\tau(r,0) = 0$. The solution is given here again in terms of the amplitudes A_s:

$$\begin{aligned} \tau(r,t) = \; \omega_0\,M\,r\,t_r \; \Big\{ & \frac{\partial A_0}{\partial r}(1 - e^{-t/t_r}) \\ & - \frac{2}{1 - t_r/t_0}\,\frac{\partial A_{i/t_0}}{\partial r}\,(e^{-t/t_0} - e^{-t/t_r}) \\ & + \frac{1}{1 - 2t_r/t_0}\,\frac{\partial A_{2i/t_0}}{\partial r}(e^{-2t/t_0} - e^{-t/t_r}) \\ & + \sum_{j=0}^{\infty} \frac{\partial Z_j}{\partial r} \Big[\frac{B_{1,j}}{a_{1,j} + 1/t_r}(e^{a_{1,j}t} - e^{-t/t_r}) \\ & \qquad + \frac{B_{2,j}}{a_{2,j} + 1/t_r}(e^{a_{2,j}t} - e^{-t/t_r}) \Big] \Big\} \quad . \end{aligned} \tag{4-5}$$

Appendix A.5.2 lists it in a more explicit form.

This solution is a quite general expression of the behavior of a Maxwell material in the Couette geometry. It describes the interaction of inertia ρ, elasticity M and viscosity η. This three material parameters, the geometry scales R_i and R_o, and the boundary condition (4-1a) can be combined to form three time scales, and their relation classifies the material behavior.

$$t_c = \frac{R_o - R_i}{c}, \qquad t_r = \frac{\eta}{M}, \qquad t_0 \text{ (see eq. (4-1a))}$$

The newly introduced variable t_c is an approximate measure for the time necessary for a signal to travel the distance from R_i to R_o. Figure 4.3 shows an example of the velocity and stress distribution in which multiple reflections between spindle and crucible walls take place. The 3 time scales yield 6 types of

material response. In the following list the signs of inequality ($<$) must not be read literally. Their meaning is that one time scale is significantly smaller or larger, so that the corresponding effect becomes clear:

a. $t_c < t_r < t_0$
The signal can travel from R_i to R_o (and back) before the material relaxes. Therefore, even though the acceleration takes place on a longer time scale than material relaxation, the stress response is slower than the velocity.

b. $t_c < t_0 < t_r$
The signal can travel from R_i to R_o (and back) before the material relaxes. The acceleration is also faster than material relaxation. Thus the stress response is always slower compared to case *a*.

c. $t_0 < t_c < t_r$
The boundary condition is the fastest. The signal travels faster between R_i and R_o and back than the material can relax. This can be seen as characteristic advances in the stress signal.

d. $t_0 < t_r < t_c$
The boundary condition is the fastest. The material relaxes faster than the signal travels between R_i and R_o and back. The stress response is faster compared to the velocity at R_i and shows a characteristic overshoot.

e. $t_r < t_0 < t_c$
The material relaxes faster than the material is accelerated. The material is accelerated faster than the signal travels back and forth in the gap. This results in a characteristic stress overshoot on the time scale t_0. The limit of this case for $t_r \to 0$ corresponds to the behavior of a Newtonian fluid.

f. $t_r < t_c < t_0$
The material relaxes faster than the signal travels in the gap, and is accelerated on a longer time scale compared to the signal travel time. The stress response is thus faster than the velocity at R_i, but does not show any overshoot. The limit $t_r \to 0$ in this case does not correspond to the Newtonian fluid, since t_c has a significant effect — by "removing" the overshoot during material acceleration — determined by c, the wave speed. c, however, is infinite in an idealized Newtonian fluid.

Figure 4.4 shows typical stress responses for all of the 6 described categories. The change between response types due to changes in geometry is difficult to describe by simple closed formulas. This change heavily relies on the Bessel functions employed in solution (4-5) and the numerically determined wave numbers q_j.

Figure 4.5 shows a transition from a type *a.* response, to a type *e.* response, passing the 'region' of type *f.*

The maxwell material, as shown by the solution of this boundary value problem, shows qualitatively all features necessary to describe the strong time dependent response in the viscometer. A type *d.* response with a small enough acceleration time t_0 corresponds to the time dependent torque response shown in Figure 3.4 and described in the preceding chapter on viscometry (page 25). The maxwell model, however, predicts a torque response on the time scale of the larger one of t_r and t_c. This time scales, if determined by the macroscopic parameters $\rho,\ M,\ \eta$ are much to small to be comparable to 10^2 s. The geometry dependence, which is not covered by the simple estimate in the introduction of this chapter, is much too weak to be responsible for the multiple orders lying between the measured and the predicted relaxation durations.

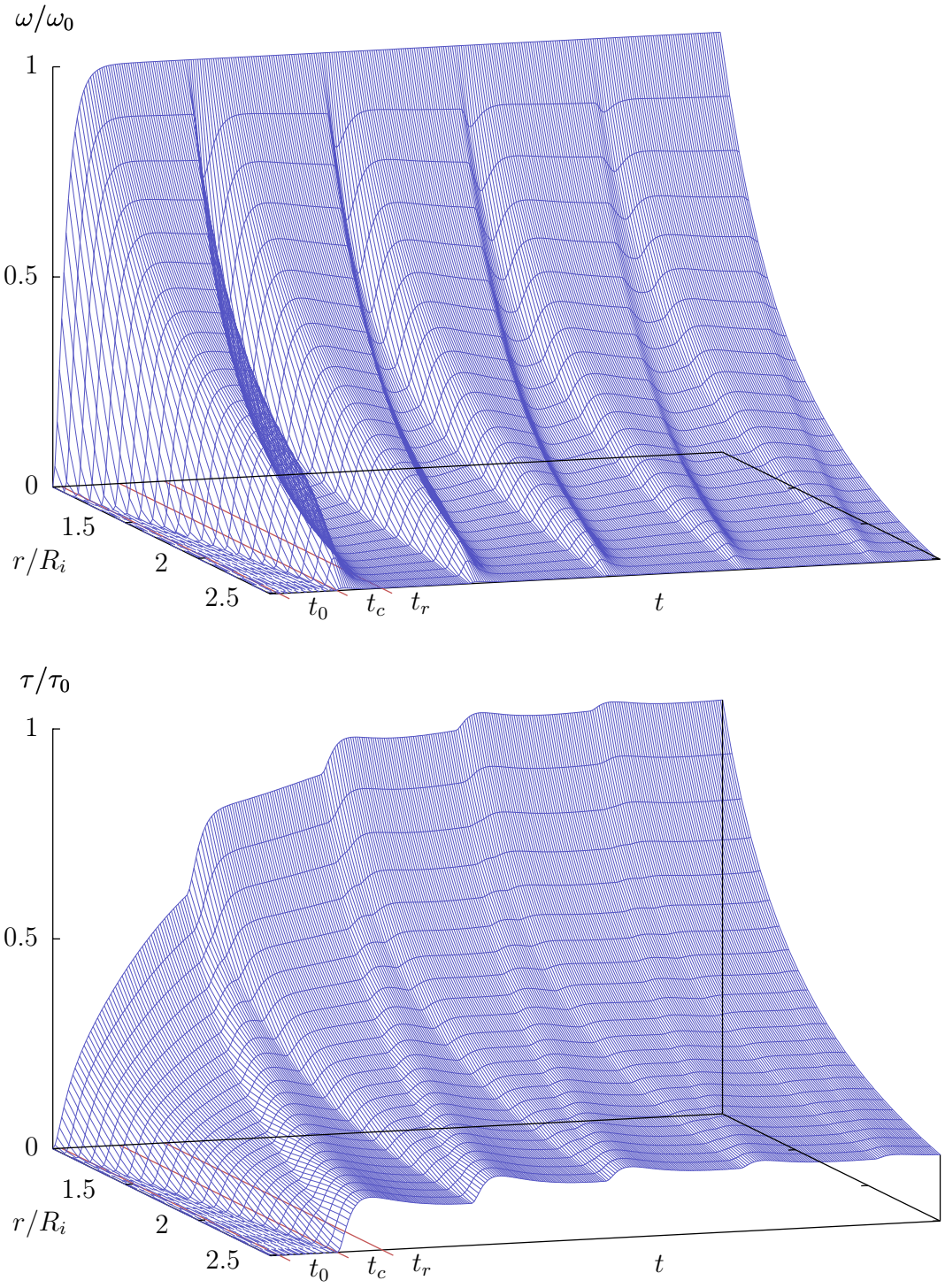

Figure 4.3: *Typical response of a Maxwell viscoelastic material to a step-like forced motion at the boundary R_i, drawn in the upper plot as line parallel to the t axis. The plots show the angular frequency $\omega(r,t)$ and shear stress $\tau(r,t)$ between the cylinder walls ($R_i \le r \le R_o$). Reflections at R_o can be identified as well as the wave speed c. Here the boundary and material parameters were chosen so that $t_r = 5\,t_0$.*

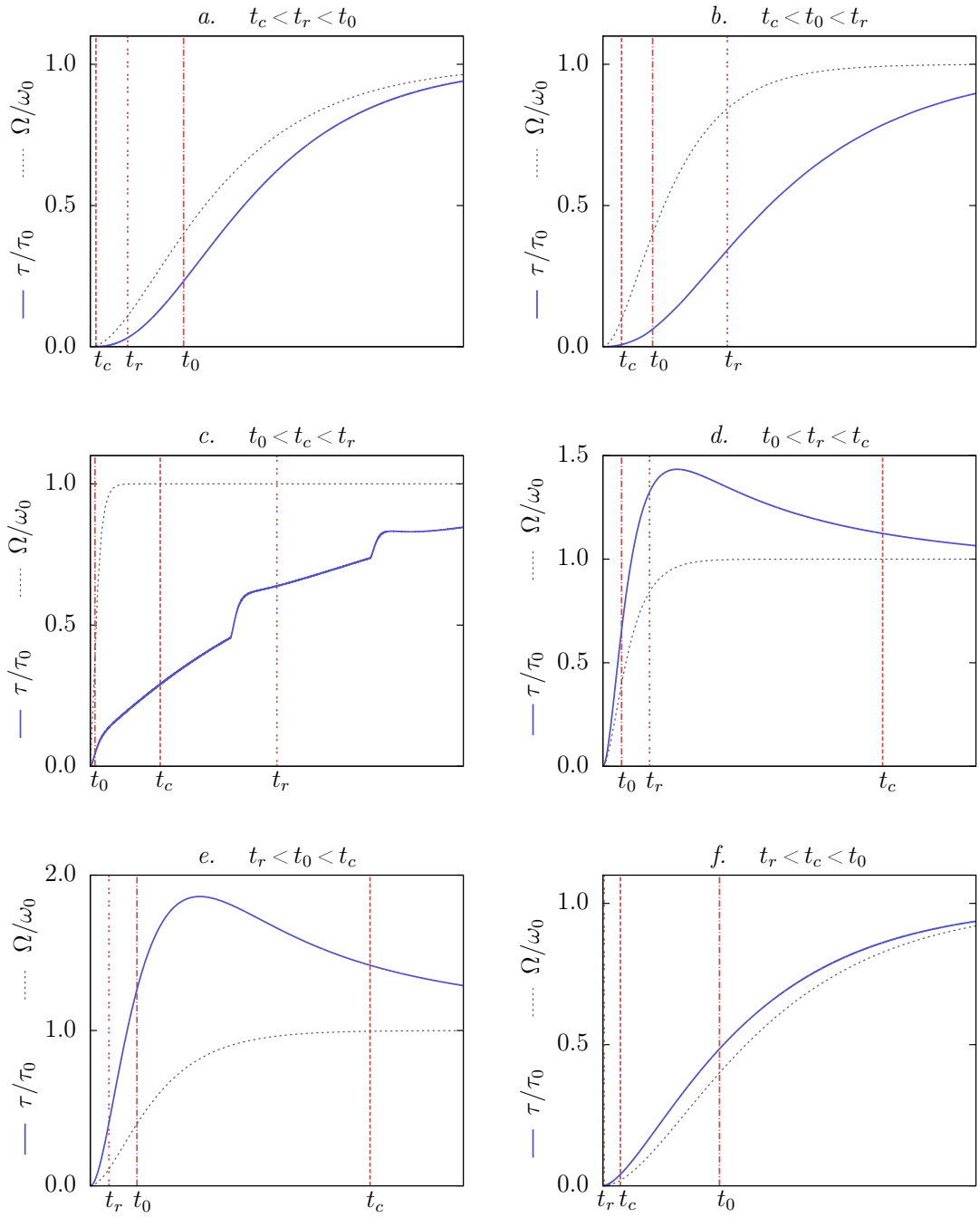

Figure 4.4: *Classification of stress response of the Maxwell material. Vertical red lines show the position of corresponding time scales. For comparison with the blue stress reponse, the velocity at $r = R_i$ (i.e. the boundary condition) is plotted as grey dashes into each graph.*

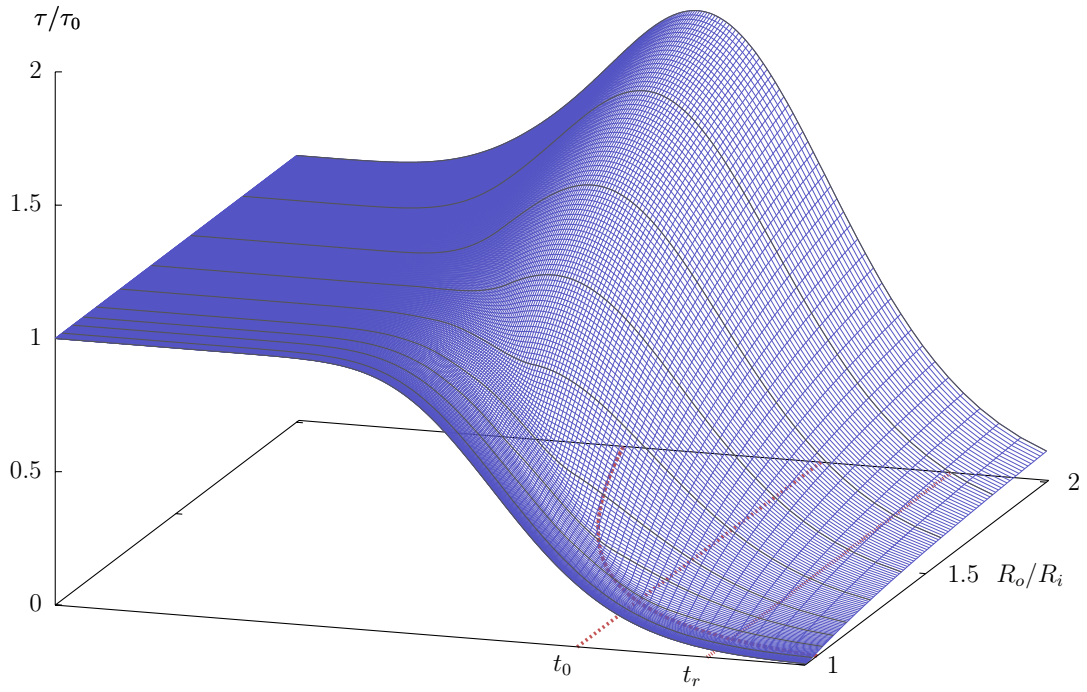

Figure 4.5: *Material response at various geometries. Transition of material stress response from asymptotic convergence from smaller values for geometries with R_o close to R_i, to overshoot behavior for $R_o > R_i$. The response behavior starts as type $a.$, crosses type $f.$, and ends as type e. Time scales are drawn as lines into the t-R_o plane. The vertical axis is scaled by τ_0 so that the response converges to 1 for large t. The t-axis is scaled logarithmically.*

4.3 Newtonian Fluid

The behavior of a Newtonian fluid can be considered as a limit of $t_r \to 0$ of the Maxwell fluid derived in the preceding section. For small relaxation times the first time derivative in equation (4-3) is dominant compared to the second time derivative, so that the equation of motion becomes independent of shear modulus M:

$$\frac{\rho}{\eta}\frac{\partial \omega}{\partial t} = \frac{\partial^2 \omega}{\partial r} + \frac{3}{r}\frac{\partial \omega}{\partial r} \quad . \tag{4-6}$$

This equation can also be derived from the general equation of motion (2-9) and the material behavior of a Newtonian fluid $\tau = \eta\,\dot{\gamma}$. It can also be derived directly from the Navier-Stokes equations by limitting the motion to a Couette system [31]. The solution of the boundary value problem is also given by formula (4-4), the wave numbers given from boundary condition (4-1a) do not contain wave speed c, however. They are given by

$$k_s^2 = -is\rho/\eta \quad , \quad k_{i/t_0} = \sqrt{\frac{\rho}{\eta\, t_0}} \quad , \quad k_{2i/t_0} = \sqrt{2}\, k_{i/t_0} \quad . \tag{4-7}$$

The shear stress of a viscous material is not determined from the velocity distribution by a differential equation, but by a linear relation. Thus this materials react quasi instantneoulsy – as a whole – to applied stress or deformation. Consequently discontinuities in the quantities ω and τ are possible. Therefore τ is uniquely defined by the solution of (4-6) and the material equation of a Newtonian fluid. Since τ is directly proportional to the shear rate no new features can be extracted from this solutions time dependence. Therefore it will not be discussed in further detail.

4.4 Power-Law viscosity

As shown in chapter 3 a power law description of viscosity is much more applicable to silicate based materials compared to a Newtonian model. Combination of its material equation

$$\frac{\tau}{\tau_0} = \left(\frac{\dot{\gamma}_v}{\dot{\gamma}_0}\right)^m \quad \Leftrightarrow \quad \tau = \bar{\eta}\,\dot{\gamma}^m \quad . \tag{4-8}$$

with equation (2-9), the equation of motion of a power law fluid in Couette geometry reads

$$\rho/(m\,\bar{\eta})\;(r\,\omega')^{1-m}\dot{\omega} \;=\; \omega'' + (m+1)/m\;\frac{\omega'}{r} \quad . \tag{4-9}$$

This is a quasi-linear partial differential equation. As long as $0 \leq m \leq 1$ the nonlinearity sticks to terms containing first derivatives. In the other case it is still possible to formulate equation (4-9) as quasi-linear, it might however make more sense to formulate an equation of motion for material stress τ. The nonlinearity circumvents the possibility to superpose multiple special solutions to customize solutions to a boundary value problem. Equation (4-9) needs to be solved at once. An ansatz

$$\omega'^{1-m} = \zeta\, r^{m-1}\frac{\ddot{\omega}}{\dot{\omega}}$$

with the complex parameter ζ transforms equation (4-9) into a linear partial differential equation of an increased order:

$$\zeta\rho/(m\,\bar{\eta})\;\ddot{\omega} = \omega'' + (m+2)/m\;\frac{\omega'}{r} \quad . \tag{4-10}$$

As was shown in chapter 4 for the boundary value problem of the maxwell material, this equation can be solved analytically. However, either the transformation parameter ζ and the second order derivative need a physical inerpretation, or a physically reasonable mapping of the boundary conditions needs to be established. Both alternatives are beyond the scope of this work.

Linear elasticity and viscous power law 4.5

Combining the considerations of the previous sections naturally yields the question of an equation of motion for an elastic material with a non-linear friction property. Following the considerations of section 4.2 elastic effects yields a constitutive relation in form of a differential equation. The total deformation is assumed as sum of elastic and viscous contribution as in the case of the linear maxwell material. The constitutive relation reads

$$r\,\frac{\partial\omega}{\partial r} = \dot{\gamma} = \dot{\gamma}_e + \dot{\gamma}_v = \frac{1}{M}\frac{\partial\tau}{\partial t} + \left(\frac{\tau}{\bar{\eta}}\right)^{1/m} \tag{4-11}$$

This material equation yields in combination with the general equation of motion (2-9) an equation of motion formulated in τ, which reads

$$\frac{\partial^2 \tau}{\partial r^2} - \frac{\rho}{M}\frac{\partial^2 \tau}{\partial t^2} - \rho \frac{\partial}{\partial t}\left(\frac{\tau}{\bar{\eta}}\right)^{1/m} + \frac{1}{r}\frac{\partial \tau}{\partial r} - \frac{4}{r^2}\tau = 0 \quad . \tag{4-12}$$

A similar ansatz as for the viscous power-law material can be made here. The assumption

$$\rho \frac{\partial}{\partial t}\left(\frac{\tau}{\bar{\eta}}\right)^{1/m} = \vartheta \frac{\partial \tau}{\partial t}$$

yields a linear wave equation which contains a damping term dependent on ϑ:

$$\frac{\partial^2 \tau}{\partial r^2} + \frac{1}{r}\frac{\partial \tau}{\partial r} - \frac{4}{r^2}\tau = \frac{\rho}{M}\frac{\partial^2 \tau}{\partial t^2} + \vartheta \frac{\partial \tau}{\partial t} \quad . \tag{4-13}$$

The main parts of this equation can be solved analytically. What remains to be proven is the physical significance of these kind of solutions – i.e. a reasonable explanation of parameter ϑ – as well as their applicability to suitable boundary conditions.

Conclusions

5

A new method to determine viscosities of macroscopic, inhomogeneous samples at high temperatures was developed. The results show clearly that the measured Billstein basalt, formerly classified to be a Newtonian material [47], is a non-Newtonian material. The viscosities vary by more than a factor of 10 over the measured shear rates at each given temperature. A power-law fits well to the measured flow curve, though it was not assumed to determine the latter. The transient behavior of this melt differs also strongly from a Newtonian material. Viscous heating does not play a significant role. While it is still difficult to quantify the material stress-deformation relationship, it was shown (chapter 4) that it is clearly the rheology which determines the long term material relaxation. The results may be a hint that the connection between viscosities of a macroscopic sample and microscopic properties might not be the straight forward application of a microscopically calculated Maxwell relaxation time to macroscopical scenarios, or the calculation of viscosities from a materials chemical composition alone. From the physical point of view this is not surprising: The viscosity describes the dissipation of momentum (and energy) due to material deformation. Dissipation has, however, always been the deviation, the rest not taken into account by any model. And there is no reason why this deviation should follow extraordinarily simple rules. Perhaps it is possible to deploy the evolving models of material jamming [26, 33, 37], connecting non-linear friction and temperature states, to magmatic melts. This would establish a connection to smaller structures, and probably unveil the reasons for the non-Newtonian behavior. For practical application a power-law returns satisfying results. This power-law predicts a diverging viscosity at small shear rates. This property can replace the effort to measure an objective yield stress. What remains to be solved is the interaction of a power-law rheology with an elastic modulus, i.e. equation (4-12). It also remains to be measured if viscosity continues to diverge when further decreasing the shear rate, or if it will converge to a Newtonian plateau. The measured shear thinning behavior is however significant, since the experimental setup was designed so that the corresponding shear rates ($10^{-2}\,\mathrm{s}^{-1} - 10^{2}\,\mathrm{s}^{-1}$) are in the same range as observed

in natural volcanic processes.

References

[1] M. Abramowitz & I. A. Stegun (editors), 1970: *Handbook of Mathematical Functions*. Dover Books, 9th edition.

[2] G. Adam & J. H. Gibbs, 1965: *On the Temperature Dependence of Cooperative Relaxation Properties in Glass-Forming Liquids*. In The Journal of Chemical Physics, volume 43, no. 1, page 139. doi:10.1063/1.1696442.

[3] D. Andronico, S. Branca, S. Calvari, M. Burton, T. Caltabiano, R. A. Corsaro, P. D. Carlo, G. Garfi, L. Lodato, L. Miraglia, F. Murè, M. Neri, E. Pecora, M. Pompilio, G. Salerno, & L. Spampinato, 2005: *A multi-disziplinary study of the 2002-03 Etna eruption: insights into a complex plumbing system*. In Bulletin of Volcanology, volume 67, no. 4, page 314. doi:10.1007/s00445-004-0372-8.

[4] H. A. Barnes, 1995: *A review of the slip (wall depletion) of polymer solutions, emulsions and particle suspensions in viscometers: its cause, character, and cure*. In Journal of Non-Newtonian Fluid Mechanics, volume 56, page 221.

[5] H. A. Barnes, 1999: *The yield stress - a review or 'παντα ρει' - everything flows?* In Journal of Non-Newtonian Fluid Mechanics, volume 81, page 133.

[6] H. A. Barnes & K. Walters, 1985: *The yield stress myth?* In Rheologica Acta, volume 24, no. 4, page 323.

[7] G. K. Batchelor, 1990: *An Introduction To Fluid Dynamics*. Cambridge University Press.

[8] M. Beblo, A. Berkthold, U. Bleil, H.Gebrande, B. Grauert, U. Haack, V. Haak, H. Kern, H. Miller, N. Petersen, J. Pohl, F. Rummel, & J. R. Schopper, 1982: *Physical Properties of Rocks*. In K.-H. Hellwege & G. Angenheister (editors), *Group V. Geophysics and Space Research*, Springer, volume 5,1,b of *Landolt-Börnstein. Numerical Data and Functional Relations in Science and Technology. New Series*.

[9] S. Bez, 2001: *Thermodynamisches und rheologisches Verhalten von Lavaflüssen.* Diplomarbeit, Universität Würzburg. (unpublished).

[10] E. C. Bingham, 1914: *The Viscosity of Binary Mixtures.* In Journal of Physical Chemistry, volume 18, no. 2, page 157.

[11] R. B. Bird, R. C. Armstrong, & O. Hassager, 1987: *Dynamics of Polymeric Liquids*, volume 1. John Wiley & Sons, 2nd edition.

[12] Y. Bottinga, 1994: *Configurational entropy and the non-Newtonian rheology of homogeneous silicate melts.* In Physical Review B, volume 49, no. 1, page 95. doi:10.1103/PhysRevB.49.95.

[13] Y. Bottinga & P. Richet, 1996: *Silicate melt structural relaxation: rheology, kinetics, and Adam-Gibbs theory.* In Chemical Geology, volume 128, no. 1-4, page 129 . doi:10.1016/0009-2541(95)00168-9.

[14] S. Branca & P. D. Carlo, 2005: *Types of eruptions of Etna volcano AD 1670-2003: implications for short-term eruptive behaviour.* In Bulletin of Volcanology, volume 67, no. 8, page 732.

[15] R. Büttner, P. Dellino, H. Raue, I. Sonder, & B. Zimanowski, 2006: *Stress Induced Brittle Fragmentation of Magmatic Melts: Theory and Experiments.* In Journal of Geophysical Research, volume 111, page B08204. doi:10.1029/2005JB003958.

[16] R. Büttner & B. Zimanowski, 1998: *Physics of Thermohydraulic Explosions.* In Physical Review E, volume 57, no. 5, page 5726. doi: 10.1103/PhysRevE.57.5726.

[17] R. Büttner, B. Zimanowski, C. Lenk, A. Koopmann, & V. Lorenz, 2000: *Determination of thermal conductivity of natural silicate melts.* In Applied Physics Letters, volume 77, no. 12, page 1810. doi:10.1063/1.1311815.

[18] Deutsches Institut für Normung, 1980: *DIN 53019 — Messung von Viskositäten und Fließkurven mit Rotationsviskosimetern mit Standardgeometrie.*

[19] M. Dragoni, 1989: *A dynamical model of lava flows cooling by radiation.* In Bulletin of Volcanology, volume 51, no. 2, page 88. doi:10.1007/BF01081978.

[20] M. Dragoni, I. Borsari, I. Borsari, & A. Tallarico, 2005: *A model for the shape of lava flow fronts.* In Journal of Geophysical Research, volume 110, page B09203. doi:10.1029/2004JB003523.

[21] M. Dragoni & A. Tallarico, 1994: *The effect of crystallization on the rheology and dynamics of lava flows.* In Journal of Volcanology and Geothermal Research, volume 59, no. 3, page 241. doi:10.1016/0377-0273(94)90098-1.

[22] G. Fröhlich, B. Zimanowski, & V. Lorenz, 1993: *Explosive Thermal Interactions Between Molten Lava and Water.* In Experimental Thermal and Fluid Science, volume 7, page 319.

[23] M. Galassi, J. Davies, J. Theiler, B. Gough, G. Jungman, M. Booth, & F. Rossi, 2003: *Gnu Scientific Library: Reference Manual.* Network Theory Ltd., 2nd edition.

[24] D. Giordano, J. K. Russell, & D. B. Dingwell, 2008: *Viscosity of magmatic liquids: A model.* In Earth and Planetary Science Letters, volume 271, no. 1-4, page 123. doi:10.1016/j.epsl.2008.03.038.

[25] R. W. Griffiths, 2000: *The Dynamics of Lava Flows.* In Annual Review of Fluid Mechanics, volume 32, no. 1, page 477. doi:10.1146/annurev.fluid.32.1.477.

[26] C. Heussinger & J.-L. Barrat, 2009: *Jamming Transition as Probed by Quasistatic Shear Flow.* In Physical Review Letters, volume 102, no. 21, page 218303. doi:10.1103/PhysRevLett.102.218303.

[27] A. Koopmann, 1999: *Zur Platznahme des Weiersbacher Lavastromes (Westeifel) — eine Synthese aus Gelände- und Laborarbeiten.* Diplomarbeit, Universität Würzburg. (unpublished).

[28] I. M. Krieger, 1968: *Shear Rate in the Couette Viscometer.* In Transactions of The Society of Rheology, volume 12.

[29] I. M. Krieger & H. Elrod, 1953: *Direct Determination of the Flow Curves of Non-Newtonian Fluids.* In Journal of Applied Physics, volume 24, no. 2, page 134.

[30] I. Kushiro, 1976: *Changes in Viscosity and Structure of Melt of NaAlSi2O6 Composition at High Pressures.* In Journal of Geophysical Research, volume 81, page 6347. doi:10.1029/JB081i035p06347.

[31] L. D. Landau & E. M. Lifschitz, 1991: *Lehrbuch der theoretischen Physik.* In P. Ziesche & W. Weller (editors), *Hydrodynamik*, Akademie Verlag, Berlin, volume 6 of *Lehrbuch der Theoretischen Physik.* 5th edition.

[32] M. W. Liberatore, E. J. Pollauf, & A. J. McHugh, 2003: *Shear-induced structure formation in solutions of drag reducing polymers.* In Journal of Non-Newtonian Fluid Mechanics, volume 113, no. 2-3, page 193. doi:10.1016/S0377-0257(03)00110-1.

[33] A. J. Liu & S. R. Nagel, 1998: *Jamming is not just cool any more.* In Nature, volume 396, page 21. doi:10.1038/23819.

[34] G. Lofgren, 1971: *Spherulitic Textures in Glassy and Crystalline Rocks.* In Journal of Geophysical Research, volume 76, no. 23, page 5635. doi:10.1029/JB076i023p05635.

[35] V. Lorenz & B. Zimanowski, 1984: *Fragmentation of Alkali-Basaltic Magmas and Wall-Rocks by Explosive Volcanism.* In Annales Scientifiques de l'Université de Clermont-Ferrand 2. Probabilités et Applications, volume 74, page 15.

[36] C. W. Macosko, 1994: *Rheology Principles, Measurements, and Applications.* VCH, New York, 1st edition.

[37] R. Mari, F. Krzakala, & J. Kurchan, 2009: *Jamming versus Glass Transitions.* In Physical Review Letters, volume 103, no. 2, 025701. doi:10.1103/PhysRevLett.103.025701.

[38] W. P. Mason, W. O. Baker, H. J. Mcskimin, & J. H. Heiss, 1948: *Mechanical Properties of Long Chain Molecule Liquids at Ultrasonic Frequencies.* In Physical Review, volume 73, no. 9, page 1074. doi:10.1103/PhysRev.73.1074.

[39] MatWeb. *Material Property Data.* Automation Creations Inc. Online database of material properties, `www.matweb.com`.

[40] J. C. Maxwell, 1868: *XV. On the dynamical theory of gases.* In Philosophical Magazine Series 4, volume 35, no. 235, page 129. doi:10.1080/14786446808639951.

[41] A. R. McBirney & T. Murase, 1984: *Rheological Properties of Magmas.* In Annual Review of Earth and Planetary Sciences, volume 12, page 337.

[42] H. Miyamoto & S. Sasaki, 1997: *Simulating lava flows by an improved cellular automata method.* In Computers & Geosciences, volume 23, no. 3, page 283. doi:10.1016/S0098-3004(96)00089-1.

[43] T. Murase & A. R. McBirney, 1973: *Properties of Some Common Igneous Rocks and Their Melts at High Temperatures.* In Geological Society of America Bulletin, volume 84, page 3563.

[44] R. C. Navarrete, L. E. Scriven, & C. W. Macosko, 1996: *Rheology and Structure of Flocculated Iron Oxide Suspensions.* In Journal of Colloid and Interface Science, volume 180, no. 1, page 200. doi:10.1006/jcis.1996.0290.

[45] H. Pinkerton, 1978: *Field measurements of rheology of lava.* In Nature, volume 276, page 383. doi:10.1038/276383a0.

[46] H. Pinkerton & G. Norton, 1995: *Rheological properties of basaltic lavas at sub-liquidus temperatures: laboratory and field measurements on lavas from Mount Etna.* In Journal of Volcanology and Geothermal Research, volume 68, no. 4, page 307. doi:10.1016/0377-0273(95)00018-7.

[47] H. Pinkerton & R. J. Stevenson, 1992: *Methods of determining the rheological properties of magmas at sub-liquidus temperatures.* In Journal of Volcanology and Geothermal Research, volume 53, no. 1-4, page 47. doi:10.1016/0377-0273(92)90073-M.

[48] W. H. Press, S. A. Teukolsky, W. T. Vetterling, & B. P. Flannery, 1992: *Numerical Recipes in C.* Cambridge University Press, 2nd edition.

[49] F. Reif, 1987: *Statistische Physik und Theorie der Wärme.* Walter de Gruyter, 3rd edition.

[50] R. Rivlin & J. Ericksen, 1955: *Stress-Deformation Relations for Isotropic Materials.* In Journal of Rational Mechanics and Analysis, volume 4, pages 323.

[51] H. Schlichting & K. Gersten, 2006: *Grenzschicht-Theorie.* Springer, 10th edition.

[52] W. R. Schowalter, 1978: *Mechanics of non-Newtonian Fluids.* Pergamon Press.

[53] H. R. Shaw, 1969: *Rheology of basalt in the melting range.* In Journal of Petrology, volume 10, no. 3, page 510.

[54] H. Sigurdsson, B. Houghton, H. Rymer, & J. S. and (editors), 1999: *Encyclopedia of Volcanoes.* Academic Press, 1st edition.

[55] W. I. Smirnow, 1985: *Lehrgang der höheren Mathematik*, volume 2. Verlag Harri Deutsch, 17th edition.

[56] I. Sonder, R. Büttner, & B. Zimanowski, 2006: *Non-Newtonian Viscosity of Basaltic Magma.* In Geophysical Research Letters, volume 33, page L02303. doi:10.1029/2005GL024240.

[57] G. G. Stokes, 1880: *Mathematical And Physical Papers*, volume 1. Cambridge University Press.

[58] Wacker. *Silikonöle AK.* Data Sheet.

[59] S. L. Webb & D. Dingwell, 1990: *Non-Newtonian Rheology of Igneous Melts at High Stresses and Strain Rates: Experimental Results for Rhyolite, Andesite, Basalt, and Nephelinite.* In Journal of Geophysical Research, volume 95, page 15,695.

[60] T. Wohlleben, 1993: *Zur Abkühlgeschichte experimentell erzeugter Schmelzepartikel: Analyse und Modellierung der physikalischen Prozesse.* Diplomarbeit, Universität Würzburg. (unpublished).

[61] B. Zimanowski, R. Büttner, & A. Koopmann, 2004: *Experiments on Magma Mixing.* In Geophysical Research Letters, volume 31, no. 9, page L09612. doi:10.1029/2004GL019687.

[62] B. Zimanowski, R. Büttner, V. Lorenz, & H. G. Häfele, 1997: *Fragmentation of Basaltic Melt in the Course of Explosive Volcanism.* In Journal of Geophysical Research, volume 102, page 803. doi:10.1029/96JB02935.

[63] B. Zimanowski, K. Wohletz, P. Dellino, & R. Büttner, 2003: *The volcanic ash problem.* In Journal of Volcanology and Geothermal Research, volume 122, no. 1-2, page 1. doi:10.1016/S0377-0273(02)00471-7.

Appendix A

Details of Calculations

Measures For Deformation And Rate Of Deformation

A.1

The motion of a material can be expressed in terms of a transformation converting coordinates of a given material point $\tilde{x}^i$ at time t_0 to coordinates dx^i of the same material point at time t:

$$dx^i = \frac{\partial x^i}{\partial \tilde{x}^k}\, d\tilde{x}^k = f^i{}_k d\tilde{x}^k \quad . \tag{A-1}$$

As long as the $f^i{}_k$ are denote an invertible transformation their determinant will not vanish. Then it is possible to write the $f^i{}_k$ as product of a symmetric part $u^i{}_k$ and an antisymmetric part $r^i{}_k$:

$$f^i{}_k = r^i{}_j u^j{}_k \quad . \tag{A-2}$$

The antisymmetric part can be identified with a rotation leaving the shape of a material point unaltered. The goal here, however, is to describe deformation. Hence, using the antisymmetric properties of the $r^i{}_k$, a quantity which contains only the symmetric part is a good measure for deformation:

$$c_{ik} = f^T{}_{ij}\, f^j{}_k = g_{il}\, f^l{}_j f^j{}_k \quad . \tag{A-3}$$

c_{ik} is called the (relative) Cauchy-Green Strain Tensor. An equivalent quantity is the Finger Tensor $f^i{}_j f^{Tj}{}_k$. In the following the c_{ik} will be used. This strain tensor depends on time t and on the reference configuration at time t_0, i.e. $c_{ik}|_{t=t_0} = \delta_{ik}$.

A measure for the rate of deformation is obtained from the time derivative of the deformation gradient

$$\begin{aligned} \dot{f^i}{}_k|_{t=t_0} &= \frac{\mathrm{d}}{\mathrm{d}t}(r^i{}_j u^j{}_k)|_{t=t_0} = \dot{r^i}{}_j|_{t=t_0}\, u^j{}_k|_{t=t_0} + r^i{}_j|_{t=t_0}\, \dot{u^i}{}_{kt=t_0} \\ &= (\dot{r^i}{}_k + \dot{u^i}{}_k)|_{t=t_0} \quad . \end{aligned}$$

It becomes clear that the time derivative of the deformation gradient can be expressed as the sum of an antisymmetric and a symmetric part. Explicit calculation of this derivative yields $\dot{f^i}{}_k|_{t=t_0} = v^i_{;k}$, where $v^i_{;k}$ is the covariant

derivative of the i-th velocity component. Consequently defining a suitable measure for the rate of deformation $d^i{}_k$ can be achieved as follows:

$$d_{ik} = \frac{1}{2}\left(\dot{f}_{ik} + \dot{f^T}_{ik}\right) = \frac{1}{2}(v_{i;k} + v_{k;i}) \quad . \tag{A-4}$$

The trace of this deformation rate tensor characterizes a relative change of volume in time $d^i{}_i = \mathrm{d}\dot{V}/\mathrm{d}V$, which is also known from the continuity equation

$$d^i{}_i = \operatorname{div} \boldsymbol{v} = 0 \quad . \tag{A-5}$$

A.1.1 Shear Motion

Explicit calculation of components of the strain tensor (A-3) with the assumptions given in (2-5), yields the following expressions for deformation:

$$\begin{aligned}
&c_{11} = g_{11} + g_{22}\left(\frac{\partial x^2}{\partial \tilde{x}^1}\right)^2 \quad , && c_{12} = g_{22}\frac{\partial x^2}{\partial \tilde{x}^1} \quad , && c_{13} = 0 \quad , \\
&c_{21} = g_{22}\frac{\partial x^2}{\partial \tilde{x}^1} \quad , && c_{22} = g_{22} \quad , && c_{23} = 0 \quad , \\
&c_{13} = 0 \quad , && c_{23} = 0 \quad , && c_{33} = g_{33} \quad .
\end{aligned} \tag{A-6}$$

The physical components of a tensor given in an orthogonal coordinate system are defined as

$$C_{ik} = \frac{c_{ik}}{\sqrt{g_{ii}\, g_{kk}}} \quad .$$

The C_{ik} can be expressed using only one parameter. A combination of metric tensor and deformation gradient γ is defined by

$$\gamma = \sqrt{\frac{g_{22}}{g_{11}}}\frac{\partial x^2}{\partial \tilde{x}^1} \quad , \tag{A-7}$$

and so

$$\begin{aligned}
&C_{11} = 1 + \gamma^2 && C_{12} = \gamma && C_{13} = 0 \\
&C_{21} = \gamma && C_{22} = 1 && C_{23} = 0 \\
&C_{31} = 0 && C_{32} = 0 && C_{33} = 1 \quad .
\end{aligned} \tag{A-8}$$

Physical components of the $d^i{}_k$ are calculated in a analogous way. Here the handy parameter is $\dot{\gamma}$ and called the shear rate

$$\dot{\gamma} = \sqrt{\frac{g_{22}}{g_{11}}}\frac{\partial v^2}{\partial \tilde{x}^1} \quad .$$

The physical components read then

$$\begin{array}{lll} D_{11} = 1 + \dot{\gamma}^2 & D_{12} = \dot{\gamma} & C_{13} = 0 \\ D_{21} = \dot{\gamma} & D_{22} = 1 & D_{23} = 0 \\ D_{31} = 0 & D_{32} = 0 & D_{33} = 1 \quad . \end{array} \tag{A-9}$$

Stress tensor of the shear motion — A.2

The stress tensor (2-2) is assumed to depend only on the strain tensor (A-3) and its history as well as on time t. It must follow the transformation properties of a tensor

$$\bar{s}^{i}{}_{k} = \frac{\partial x^i}{\partial \bar{x}^l} \frac{\partial \bar{x}^m}{\partial x^k} \, s^{l}{}_{m} \quad ,$$

where $\bar{x}^i(x^k)$ is some arbitrary, coordinate transformation. Now a special transformation $q^{i}{}_{k}$ can be selected which is chosen as a time independent reflection of the 3-axis

$$q^{1}{}_{1} = 1 \quad q^{2}{}_{2} = 1 \quad q^{3}{}_{3} = -1 \quad , \quad \text{others:} \quad 0 \quad .$$

Applying this to the strain tensor, we see that it stays the same for the non vanishing elements

$$\bar{c}^{i}{}_{k} = q^{i}{}_{l} c^{l}{}_{m} q^{m}{}_{k} = c^{i}{}_{k} \quad .$$

Since $q^{i}{}_{k}$ is constant in time, all parameters on which the s_{ik} depend stay the same, so that we can write

$$\bar{s}^{i}{}_{k} = q^{i}{}_{l} \, q^{m}{}_{k} \, s^{l}{}_{m} = s^{i}{}_{k} \quad .$$

However, by explicitely calculating this relation we see, that it is only true, if

$$s^{1}{}_{2} = s^{1}{}_{3} = s^{3}{}_{1} = s^{2}{}_{3} = 0 \quad .$$

s_{ik} can be assumed to be symmetric [31]. Thus the 5 non vanishing elements are determined by four independent parameters, which we choose to call $p, \tau, \mathcal{N}_1, \mathcal{N}_2$.

A.3 Divergence of the Stress Tensor

The divergence of a tensor A_{ik} in cylindrical coordinates reads

$$\begin{aligned}
(\operatorname{div} \mathsf{A})_r &= \frac{\partial a_{rr}}{\partial r} + \frac{1}{r}\frac{\partial a_{r\phi}}{\partial \phi}\frac{\partial a_{rz}}{\partial z} + \frac{a_{rr}}{r} - \frac{a_{\phi\phi}}{r} \\
(\operatorname{div} \mathsf{A})_\phi &= \frac{\partial a_{\phi r}}{\partial r} + \frac{1}{r}\frac{\partial a_{\phi\phi}}{\partial \phi} + \frac{1}{r}\frac{\partial a_{\phi z}}{\partial z} + \frac{a_{\phi r}}{r} + \frac{a_{r\phi}}{r} \\
(\operatorname{div} \mathsf{A})_z &= \frac{\partial a_{zr}}{\partial r} + \frac{1}{r}\frac{\partial a_{z\phi}}{\partial \phi} + \frac{\partial a_{zz}}{\partial z} + \frac{a_{zr}}{r} \quad .
\end{aligned}$$

With the assumed kind of stress tensor (2-8) the equations of motion (2-2) become

$$\begin{aligned}
0 &= \frac{\partial p}{\partial r} + \frac{1}{r}\frac{\partial \tau}{\partial \phi} \\
\rho\, r\, \frac{\partial^2 \phi}{\partial t^2} &= \frac{\partial \tau}{\partial r} + \frac{1}{r}\frac{\partial p}{\partial \phi} + \frac{2}{r}\tau \\
0 &= \frac{\partial p}{\partial z} + \rho\, g \quad .
\end{aligned}$$

Since we assumed that the problem is symmetric in ϕ, the first equation tells us that p is a function of z only. Thus the third equation yields the pressure dependence

$$p = \rho\, g\, (z_0 - z)$$

with an integration constant z_0, to be determined by boundary conditions. Since the variation of p is orthogonal to the motion in ϕ it does not contribute to the motion at all, so that p will not be of great further interest. The second equation is the equation of motion (2-9) to be solved in combination with some equation characterizing τ by material properties.

Equation of motion of the Maxwell Fluid A.4

The total deformation is denoted by γ and consists of two terms, the elastic, reversible deformation γ_e and the viscous, irreversible deformation γ_v. The stresses caused by this two mechanisms must be equal, i.e.

$$\begin{aligned} \gamma = \gamma_e + \gamma_v \quad &\Leftrightarrow \quad \dot{\gamma} = \dot{\gamma}_e + \dot{\gamma}_v \\ \tau = \tau_e = \tau_v \quad &= \quad M\,\gamma_e = \eta\,\dot{\gamma}_v \quad . \end{aligned}$$

This results in the differential equation (4-2)

$$\dot{\tau} = -\frac{\tau}{t_r} + M\,\dot{\gamma} \quad .$$

Calculating the derivative of equation (4-2) with respect to r and the derivative of equation (2-9) with respect to t yields

$$\begin{aligned} \frac{\partial}{\partial r}\left(r\,\frac{\partial \omega}{\partial r}\right) &= \frac{1}{M}\frac{\partial^2 \tau}{\partial r \partial t} + \frac{1}{\eta}\frac{\partial \tau}{\partial r} \\ \frac{\partial}{\partial t}\left(\rho\, r\frac{\partial \omega}{\partial t}\right) &= \frac{\partial^2 \tau}{\partial r \partial t} + \frac{2}{r}\frac{\partial \tau}{\partial r} \quad . \end{aligned}$$

Dividing the second equation by M and subtracting it from the first gives

$$\frac{\partial}{\partial r}\left(r\frac{\partial \omega}{\partial r}\right) - \frac{1}{M}\frac{\partial}{\partial t}\left(\rho\, r\frac{\partial \omega}{\partial t}\right) = \frac{1}{\eta}\frac{\partial \tau}{\partial r} - \frac{2}{r}\left(r\frac{\partial \omega}{\partial r} - \frac{\tau}{\eta}\right) \quad .$$

The second term on the right hand side of this equation is derived from equation (4-2). The two terms containing τ and a derivative of τ, can now be replaced with help of equation (2-9) by terms only consisting of expressions containing ω. This leads to equation (4-3).

Boundary Value Problem of the Maxwell Fluid A.5

There are several ways to obtain solutions of equation (4-3). The following two will be used here

a. Fouriertransform,

b. Separation of variables.

The solution is obtained in two steps, represented by the two velocities $u(r,t)$ and $v(r,t)$, respectively. $u(r,t)$ will satisfy the boundary conditions (4-1a), but not the initial conditions (4-1b). $v(r,t)$ will vanish at $r = R_i$ and $r = R_o$. Additionally, initial values of v will equal the negative initial values of u. The new boundary conditions hence read:

$$u(R_o,t) = 0 \quad , \quad u(R_i,t) = \omega_0 \left(1 - 2\,e^{-t/t_0} + e^{-2t/t_0}\right) \quad , \tag{A-10a}$$

$$v(R_o,t) = 0 \quad , \qquad v(R_i,t) = 0 \quad , \tag{A-10b}$$

$$v(r,0) = -u(r,0) \quad , \qquad \dot{v}(r,0) = -\dot{u}(r,0) \quad . \tag{A-10c}$$

The solution of the boundary value problem will then have the structure

$$\omega(r,t) = u(r,t) + v(r,t) \quad . \tag{A-11}$$

A.5.1 u – Fourier transform

With the relaxation time $t_r = \eta/M$ and some wave speed defined by $c^2 = M/\rho$, a fourier transform can be applied to equation (4-3)

$$r^2 \frac{d^2}{dr^2}\, \mathcal{F}_s u + 3\,r\,\frac{d}{dr}\, \mathcal{F}_s u + c^2\, r^2 \left(s^2 - i\,s/t_r\right)\, \mathcal{F}_s u = 0 \quad . \tag{A-12}$$

The transformation

$$\begin{aligned} x &= c\,\sqrt{s^2 - i\,s/t_r}\; r = k_s\, r \quad , \\ y &= r\,\mathcal{F}_s u \quad , \end{aligned} \tag{A-13}$$

yields a Bessel differential equation of first order:

$$x^2\,\frac{d^2y}{dx^2} + x\,\frac{dy}{dx} + (x^2 - 1)\,y = 0 \quad . \tag{A-14}$$

The general solution is a linear combination of the two linear independent Bessel functions of first order

$$y = C_1\,J_1(x) + C_2\,Y_1(x) \quad .$$

C_1 and C_2 are integration constants. Thus the general solution of equation (A-12) is

$$\mathcal{F}_s u = \frac{1}{r}\left(C_1\,J_1(k_s r) + C_2\,Y_1(k_s r)\right) \quad . \tag{A-15}$$

Boundary condition (A-10a) determines an integration constant at $r = R_o$ as

$$C = \frac{C_2}{C_1} = -\frac{J_1(k_s R_o)}{Y_1(k_s R_o)} \quad .$$

Further (A-10a) determines the second constant via its fourier transform at $r = R_i$ by

$$\frac{C_1}{R_i}\left\{ J_1(k_s R_i) - \frac{J_1(k_s R_o)}{Y_1(k_s R_o)}\, Y_1(k_s R_o) \right\} = \sqrt{2\pi}\omega_0 \; [\, \delta(s) - 2\delta(s - i/t_0) + \delta(s - 2i/t_0)\,] \quad .$$

Both conditions included, the solution reads

$$\mathcal{F}_s u(r) = \sqrt{2\pi}\,\omega_0 \; \frac{R_i}{r}\, \frac{\phi_{k_s}(r)}{\phi_{k_s}(R_i)} \; [\, \delta(s) - 2\delta(s - i/t_0) + \delta(s - 2i/t_0)\,] \quad ,$$

where $\phi_k(r) = J_1(r)Y_1(R_o) - J_1(R_o)Y_1(r)$. Application of the inverse fourier transform $\mathcal{F}_t^{-1}(\mathcal{F}_s u)$ leads to the first part in equation (4-4)

$$\omega(r,t) = \omega_0 \; \left(A_0(r) - 2A_{i/t_0}(r)\, e^{-t/t_0} + A_{2i/t_0}\, e^{-2t/t_0} \right) \quad . \tag{A-16}$$

Here the "amplitudes" $A_s(r)$ are given by

$$A_s(r) = \frac{R_i}{r}\, \frac{\phi_{k_s}(r)}{\phi_{k_s}(R_i)} \quad .$$

In the case $s = 0$, the amplitude is given by its limitting value

$$A_0(r) = \lim_{s \to 0} \; \frac{R_i}{r} \frac{J_1(k_s r)Y_1(k_s R_o) - J_1(k_s R_o)Y_1(k_s r)}{J_1(k_s R_r)Y_1(k_s R_o) - J_1(k_s R_o)Y_1(k_s R_i)}$$

The Bessel functions behave [1] like

$$\begin{aligned} z \to 0: \quad J_\nu(z) &\simeq \frac{1}{\Gamma(\nu+1)} \left(\frac{z}{2}\right)^\nu \\ Y_\nu(z) &\simeq -\frac{\Gamma(\nu)}{\pi} \left(\frac{2}{z}\right)^\nu \quad , \end{aligned}$$

thus

$$A_0(r) = \frac{(R_o/r)^2 - 1}{(R_o/R_i)^2 - 1} \quad . \tag{A-17}$$

A.5.2 v – Separation of variables

For $v(r,t)$ the ansatz

$$v(r,t) = T(t) \cdot R(r) \tag{A-18}$$

is applied to the partial differential equation (4-3), which yields two ordinary differential equations, parameterized by a currently not determined wave number, say q:

$$\begin{aligned} \frac{d^2T}{dt^2} + \frac{1}{t_r}\frac{dT}{dt} \mp (qc)^2\, T &= 0 \\ r^2\,\frac{d^2R}{dr^2} + 3r\,\frac{dR}{dr} \mp\ q^2\, R &= 0 \quad . \end{aligned} \tag{A-19}$$

The corresponding general, parameterized solutions are

$$\begin{aligned} T_q(t) &= B_{1,q}\, e^{a_{1,q}t} + B_{2,q}\, e^{a_{2,q}t} \quad , \quad \text{and} \\ R_q(r) &= \begin{cases} \dfrac{1}{r}\left(C_{1,q}\, J_1(qr) + C_{2,q}\, Y_1(qr)\right) & , \quad +q^2 \\ \dfrac{1}{r}\left(C_{1,q}\, I_1(qr) + C_{2,q}\, K_1(qr)\right) & , \quad -q^2 \quad , \end{cases} \end{aligned} \tag{A-20a}$$

where

$$\begin{aligned} a_{1,q} &= -\frac{1}{2\,t_r} \ + \ b_j = -\frac{1}{2\,t_r} + \sqrt{\left(\frac{1}{2\,t_r}\right)^2 \pm (qc)^2} \quad , \quad \text{and} \\ a_{2,q} &= -\frac{1}{2\,t_r} \ - \ b_j = -\frac{1}{2\,t_r} - \sqrt{\left(\frac{1}{2\,t_r}\right)^2 \pm (qc)^2} \quad . \end{aligned} \tag{A-20b}$$

To get finite values for $v(r,t)$ at all t, the negative signs in the square roots of equation (A-20b) need to be chosen. Correspondingly the lower sign of the solutions in equation (A-19) are taken. One boundary condition of (A-10c), e.g. at the inner radius $v(R_i,t) = 0$, is satisfied if

$$C_q = C_{2,q}/C_{1,q} = -J_1(qR_i)/Y_1(qR_i) \quad . \tag{A-21}$$

Then the condition at R_o is

$$\begin{aligned} 0 &= \frac{C_{1,q}}{R_o}\left(J_1(qR_o) - \frac{J_1(qR_i)}{Y_1(qR_i)}\, Y_1(qR_i)\right) \qquad \Leftrightarrow \\ 0 &= J_1(qRo)\, Y_1(qR_i) - J_1(qR_i)\, Y_1(qR_o) \quad . \end{aligned} \tag{A-22}$$

This condition has infinitely many positive solutions for q, however the equation cannot be solved analytically. A numerical calculation gives knowledge of

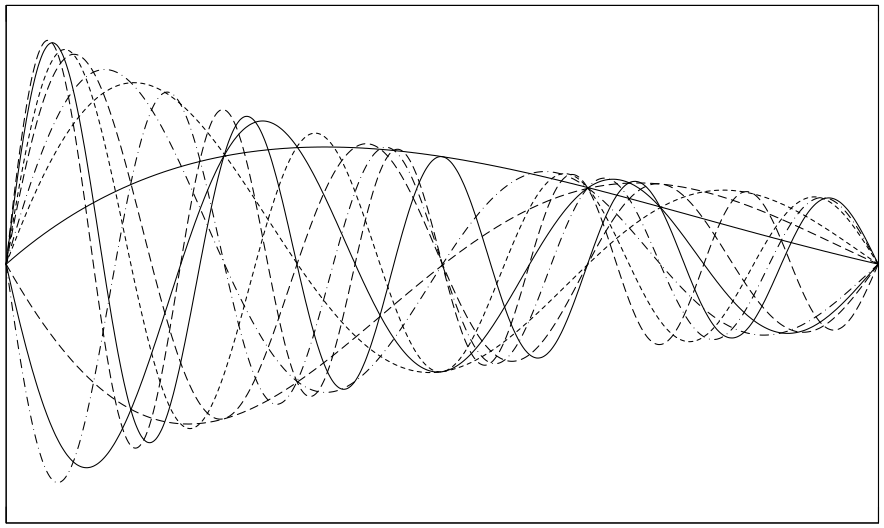

Figure A.1: *First* 10 *base functions* $Z_j(r)$ *of separation ansatz* (A-18) *between* $r = R_i$ *and* $r = R_o$.

these numbers, which from now will be denoted by q_j, where j takes integer values, starting at 1. The solutions corresponding to a specific q_j will from now be writteen as $v_j = T_j\, R_j$ etc. This condition can be used to construct a fundamental system with base functions $R_j(r)$ [55]. A weighted scalar product of two functions $f_1(r),\ f_2(r)$ can be defined by

$$\langle f_1,\ f_2\rangle = \int_{R_i}^{R_o} f_1(r)\,\overline{f_2}(r)\,r^3 dr \quad ,$$

where the bar denotes the complex conjugate of a number. Calculating explicitely the products $\langle R_j,\ R_l\rangle$ it is seen that the R_j are orthogonal on $[R_i, R_o]$, i.e. $\langle R_j,\ R_l\rangle \sim \delta_{j,l}$. The equation

$$\delta_{j,l} = \langle Z_j,\ Z_l\rangle = \frac{1}{N_j\overline{N}_l}\ \langle R_j,\ R_l\rangle \tag{A-23}$$

defines hence a normalized set $Z_j(r) = R_j(r)/N_j$ of functions proportional to the R_j, satisfying ansatz (A-18). Figure A.5.2 gives an impression of the $Zj(r)$ in the range$[R_i, R_o]$.

Recalling the initial conditions in (A-10c) $v(r,0) = -u(r,0)$ and $\dot{v}(r,0) = -\dot{u}(r,0)$, with the onthonormal Z_j, two conditions for the integration constants

$B_{1,j},\ B_{2,j}$ of the T_j can be formulated:

$$\begin{aligned} B_{1,j} + B_{2,j} &= -\langle u(r,0),\ Z_j\rangle \\ &= -\omega_0 \left(\langle A_0,\ Z_j\rangle - 2\left\langle A_{i/t_0},\ Z_j\right\rangle + \left\langle A_{2i/t_0},\ Z_j\right\rangle\right) \end{aligned}$$

$$\begin{aligned} a_{1,j}B_{1,j} + a_{2,j}B_{2,j} &= -\langle \dot{u}(r,0),\ Z_j\rangle \\ &= -\omega_0\ 2/t_0 \left(\left\langle A_{i/t_0},\ Z_j\right\rangle - \left\langle A_{2i/t_0},\ Z_j\right\rangle\right) \quad . \end{aligned}$$

For a further analysis it is necessary to split the T_j into even and odd functions with respect to t. Since the b_j take either real or imaginary, but never complex numbers, the T_j can be written in terms of real functions

$$\begin{aligned} T_j(t) = \omega_0\, e^{-t/(2t_r)} \Big\{ &\langle A_0,\ Z_j\rangle \left[-1/(2t_r) b_j^{-1}\, f_{odd}(t) - f_{even}(t)\right] \\ -2 &\left\langle A_{i/t_0},\ Z_j\right\rangle \left[(1/t_0 - 1/(2t_r))\, b_j^{-1}\, f_{odd}(t) - f_{even}(t)\right] \\ &\left\langle A_{2i/t_0},\ Z_j\right\rangle \left[(2/t_0 - 1/(2t_r))\, b_j^{-1}\, f_{odd}(t) - f_{even}(t)\right] \Big\} \quad , \end{aligned} \tag{A-24}$$

where

$$f_{even}(t) = \begin{cases} \cos(|b_j|t) & \text{if} \quad (q_j c)^2 > (2t_r)^{-2} \quad , \\ \cosh(b_j t) & \text{if} \quad (q_j c)^2 < (2t_r)^{-2} \quad , \end{cases}$$

and

$$f_{odd}(t) = \begin{cases} i\ \sin(|b_j|t) & \text{if} \quad (q_j c)^2 > (2t_r)^{-2} \quad , \\ \sinh(b_j t) & \text{if} \quad (q_j c)^2 < (2t_r)^{-2} \quad . \end{cases}$$

Stress

The shear stress τ is obtained as general solution of material equation (4-2):

$$\tau(r,t) = \quad e^{-t/t_r} \left\{ \int_0^t M\, r\, \frac{\partial}{\partial r}\, \omega(r,\tilde{t})\ e^{\tilde{t}/t_r} d\tilde{t}\ +\ \tau_0(r) \right\} \quad . \tag{A-25}$$

The material is assumed to start its movement from rest without any deformation in its history. Therefore $\tau(r,0)$ must vanish. Since the integral vanishes at $t = 0$, the r-dependent integration constant $\tau_0(r)$ must vanish too. The evaluated

intgral reads in terms of derivatives of the amplitudes and base functions

$$\begin{aligned}\tau(r,t) = \ \omega_0\, M\, r\, t_r \Bigg\{ & \frac{\partial A_0}{\partial r}(1-e^{-t/t_r}) \\ & - \frac{2}{1-t_r/t_0}\,\frac{\partial A_{i/t_0}}{\partial r}\,(e^{-t/t_0}-e^{-t/t_r}) \\ & + \frac{1}{1-2t_r/t_0}\,\frac{\partial A_{2i/t_0}}{\partial r}(e^{-2t/t_0}-e^{-t/t_r}) \\ & + \sum_j \frac{\partial Z_j}{\partial r}\Big[\frac{B_{1,j}}{a_{1,j}+1/t_r}(e^{a_{1,j}t}-e^{-t/t_r}) \\ & \qquad + \frac{B_{2,j}}{a_{2,j}+1/t_r}(e^{a_{2,j}t}-e^{-t/t_r})\Big]\Bigg\} \quad .\end{aligned} \tag{A-26}$$

In terms of symmetric and antisymmetric functions τ reads

$$\begin{aligned}\tau(r,t) = \omega_0\, M\, r\, t_r \Bigg\{ & \frac{\partial A_0}{\partial r}(1-e^{-t/t_r}) \\ & - \frac{2}{1-t_r/t_0}\,\frac{\partial A_{i/t_0}}{\partial r}\,(e^{-t/t_0}-e^{-t/t_r}) \\ & + \frac{1}{1-2t_r/t_0}\,\frac{\partial A_{2i/t_0}}{\partial r}(e^{-2t/t_0}-e^{-t/t_r}) \\ & + e^{-t/2t_r}\ \sum_j \Bigg[- \langle A_0,\ Z_j\rangle\ \frac{f_{odd}(t)}{b_j} \\ & + 2\ \langle A_{i/t_0},\ Z_j\rangle \Big[1 - \frac{1}{2t_0 t_r (q_j c)^2} \\ & \qquad + \frac{1}{t_0(q_j c)^2}\Big(f_{even}(t) - e^{-t/2t_r}\Big)\Big] \\ & + \langle A_{2i/t_0},\ Z_j\rangle \Big[\Big(\frac{1}{t_0 t_r (q_j c)^2} - 1\Big)\ \frac{f_{odd}(t)}{b_j} \\ & \qquad - \frac{2}{t_0(q_j c)^2}\big(f_{even}(t) - e^{-t/2t_r}\big)\Big]\Bigg]\frac{\partial Z_j}{\partial r}\Bigg\} \quad ,\end{aligned} \tag{A-27}$$

where f_{even} and f_{odd} are the same as were used in equation (A-24). The scalar products used in this solutions are derived by straight forward integration. In the following formulas the C_j obtained by evaluating the integration constant of

the boundary condition (A-21) at $q = q_j$.

$$\begin{aligned}\langle A_0,\ Z_j\rangle = \frac{R_o^2}{N_j q_j (R_o^2/R_i^2 - 1)}\Big\{ & \ J_0(q_j R_o) - J_0(q_j R_i) \\ & + \ J_2(q_j R_o) - \frac{R_i^2}{R_o^2} J_2(q_j R_i) \\ & + C_j\Big(Y_0(q_j R_o) - Y_0(q_j R_i) \\ & + \quad Y_2(q_j R_o) - \frac{R_i^2}{R_o^2} J_2(q_j R_i)\Big)\Big\}\end{aligned} \tag{A-28}$$

$$\langle A_s,\ Z_j\rangle = -\frac{q_j R_i^2}{N_j (k_s^2 - q_j^2)}\big(J_0(q_j R_i) + C_j Y_0(q_j R_i)\big) \quad \text{if } k_s^2 \geq 0 \tag{A-29}$$

$$\langle A_s,\ Z_j\rangle = -\frac{q_j R_i^2}{N_j (q_j^2 + k_s^2)}\big(J_2(q_j R_i) + C_j Y_2(q_j R_i)\big) \quad \text{if } k_s^2 \leq 0 \tag{A-30}$$

And the normalizing factors N_j, finally, read

$$\begin{aligned} N_j^2 = \ & \frac{R_i^2}{2}\Big(J_0(q_j R_i) J_2(q_j R_i) + 2\, C_j J_0(q_j R_i) Y_2(q_j R_i) \\ & \quad + \ C_j^2\, Y_0(q_j R_i) Y_2(q_j R_i)\Big) \\ & + \frac{R_o^2}{2}\Big(J_0(q_j R_o) J_2(q_j R_o) + 2\, C_j J_0(q_j R_o) Y_2(q_j R_o) \\ & \quad + \ C_j^2\, Y_0(q_j R_o) Y_2(q_j R_o)\Big) \quad . \end{aligned} \tag{A-31}$$

Appendix B

Tables

Viscosities of test materials

B.1

Wacker AK 10000				Ciba^{TM} Magnafloc^{TM} 1011			
$\dot{\gamma}/s^{-1}$	η/Pa s			$\dot{\gamma}/s^{-1}$	η/Pa s		
0.03178	11.07	±	1.3	0.01863	33.60	±	3.5
0.05665	11.85	±	1.3	0.04217	23.36	±	4.7
0.1018	11.09	±	1.2	0.09190	17.19	±	1.1
0.1689	11.12	±	1.2	0.2377	8.695	±	0.61
0.2728	11.61	±	1.26	0.4487	5.377	±	0.40
0.4550	11.50	±	1.25	0.5809	4.900	±	0.36
0.7456	11.97	±	1.3	1.0495	3.457	±	0.25
1.263	12.14	±	1.7	1.634	2.635	±	0.19
1.753	11.33	±	1.3	3.220	1.685	±	0.12
2.753	11.55	±	1.2	16.56	0.3505	±	0.027
4.503	12.10	±	1.6	21.48	0.2788	±	0.022
7.554	12.06	±	1.5	24.56	0.2708	±	0.020
13.52	11.40	±	1.3	67.99	0.1185	±	0.022
17.10	11.41	±	1.3	106.4	0.08494	±	0.0068
27.61	11.76	±	1.4				

B.2 Chemical Composition of Billstein Basalt

The chemical composition was already well know at the start of this work. It has been published 2004 in a work on magma mixing [61].

Oxides	wt. %
Si	45.31
Al	12.86
Fe	11.93
Ca	10.50
Mg	10.90
Na	3.14
K	1.38
Mn	0.17
P	0.54
Ti	2.16

Viscosities of Billstein Basalt

B.3

1448 K/1175 °C				1458 K/1185 °C			
$\dot{\gamma}/s^{-1}$	η/Pa s			$\dot{\gamma}/s^{-1}$	η/Pa s		
0.01339	1135	±	105	0.01681	715	±	80
0.02111	1120	±	350	0.03829	429	±	45
0.05045	807	±	170	0.07964	260	±	25
0.09822	546	±	50	0.14201	175	±	25
0.16286	435	±	45	0.18438	162	±	20.5
0.30568	305	±	35	0.28684	138	±	12.5
0.47462	246	±	35	0.46464	108	±	10
0.65717	235	±	36	0.70039	94	±	9
1.32734	161	±	20	1.02558	86	±	12.5
2.23972	119	±	30	1.52940	82	±	9.5
3.29150	125	±	38	2.14217	71	±	9
5.08588	125	±	48.5	3.42825	62	±	9.5
12.0161	79	±	25.5	5.39221	57	±	8.5
20.5556	59	±	9	8.90426	53	±	8.5
23.4730	60	±	11.5	15.2676	46	±	6
				17.2255	49	±	8
				26.1884	55	±	9

1473 K/1200 °C		1498 K/1225 °C	
$\dot{\gamma}/\mathrm{s}^{-1}$	η/Pa s	$\dot{\gamma}/\mathrm{s}^{-1}$	η/Pa s
0.02091	324 ± 30	0.01456	93 ± 10
0.03624	236 ± 27.5	0.02998	67 ± 9.5
0.04641	249 ± 30	0.06700	41 ± 6
0.08991	190 ± 19	0.09639	35 ± 6
0.22402	99 ± 15	0.12754	37 ± 4
0.34006	77 ± 15	0.21577	31 ± 3
0.40470	83 ± 8.5	0.32218	29 ± 4
0.69727	67 ± 8	0.58527	25 ± 4
1.22494	51 ± 5.5	1.36677	14 ± 1.75
1.75198	47 ± 4.5	2.25809	11 ± 1.75
2.14861	45 ± 5	2.33467	12 ± 1.5
4.01037	35 ± 3	5.31442	12 ± 2.6
5.53170	34 ± 3.75	7.66270	12 ± 1.9
8.04271	36 ± 5.5	12.9595	13 ± 1.9
14.9918	31 ± 4	17.7091	12 ± 2.7
20.1732	28 ± 3.5		

Appendix C

Notes on Numerics

The notes given in this appendix are meant to present details on the numerical programs developed to process measured raw data (C.1 and C.2) or numerically calculated solutions (C.3).

Experimental derivative revisited *C.1*

This section gives an overview of function `linearSlopeApprox`, which determines a numerical derivative from experimental data. Since this function is essential

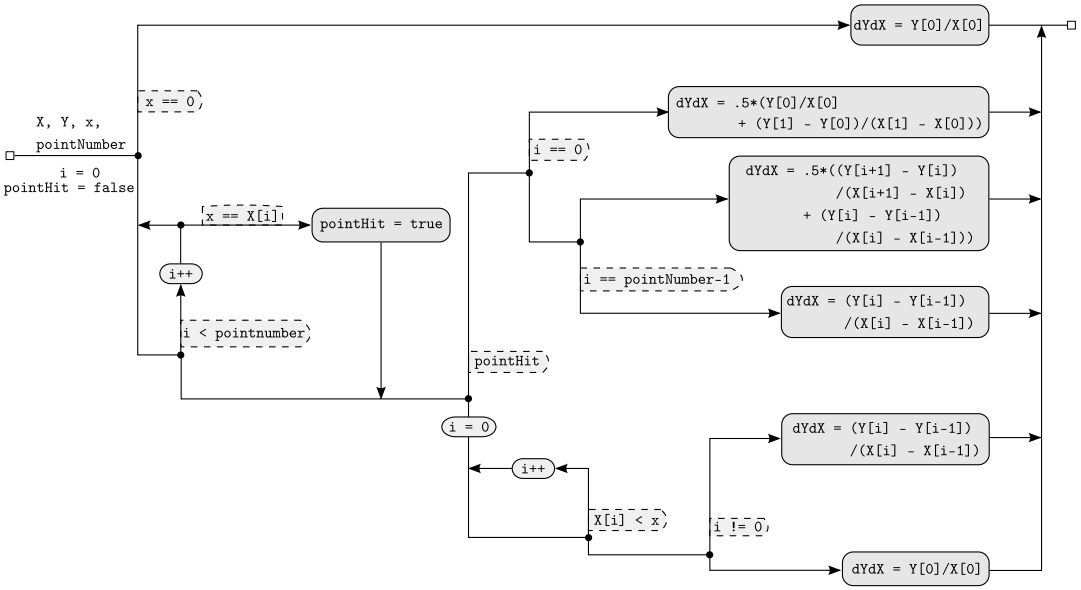

Figure C.1: *As in Figure 3.7, dots denote branching points, and the referring conditions are drawn into boxes with dashed border. Boxes with darker background show actions taken on important variables. Entrance and exit points are marked as squares.*

for the calculation, its numerical implementation is also given here.

```
public double linearSlopeApprox(double[] X,                    1
                                double[] Y,
                                double x,
```

```
                                    int pointNumber)
{
   int i;                                                          6
   boolean pointHit = false;
   double dYdX;                  // Value to be returned
   // If the argument vanishes
   if(x == 0.)
      dYdX = Y[0]/X[0];                                            11
   else
   {
      // Check if argument hits a point ...
      for(i=0; i<pointNumber; i++)
         if(x == X[i])                                             16
         {
            pointHit = true;
            break;
         }
         // ... if it hits, return the average                    21
         // value of the slopes
         // before and after this point
      if(pointHit)
      {
         if(i == 0)                                              26
            dYdX = .5*(Y[0]/X[0]
                   + (Y[1] - Y[0])/(X[1] - X[0]));
         // If x hits the last point,
         // return the slope before this point
         else if(i == pointNumber-1)                             31
            dYdX = (Y[i] - Y[i-1])/(X[i] - X[i-1]);
         //
         else
            dYdX = .5*((Y[i+1] - Y[i])
                   /(X[i+1] - X[i])                              36
                   + (Y[i] - Y[i-1])
                     /(X[i] - X[i-1]));
      }
      // Case that x does not hit a point
      else                                                       41
      {
         // Find the surrounding points
         i = 0;
         while(true)
            if(X[i] < x)                                         46
               i++;
            else
```

```
                break;
            // Usual case
            if(i != 0)
                dYdX = (Y[i] - Y[i-1])/(X[i] - X[i-1]);
            // In case that x is smaller than
            // the smallest point in X[]
            else
                dYdX = Y[0]/X[0];
        }
    }
    return dYdX;
}
```

Calculation of stress and strain rate C.2

The function `processData` is the central routine calculating the viscosity values. It is a method of class `UtilsCollection` and hence stored in the file `UtilsCollection.java`.

```
public void processData()
{
    lambda = RiRoom*RiRoom/(RoRoom*RoRoom);

    // New instance of a UtilsCollection
    UtilsCollection uc = new UtilsCollection();

    // Calculate average values ...
    // Of long immersion depth
    uc.average(pointNumber, startLong, endLong, inDirLong);
    omegaLong =       uc.omega;
    sigmaOmLong =     uc.sigmaOm;
    torqueLong =      uc.torque;
    sigmaTorqueLong = uc.sigmaTorque;
    tempLong =        uc.temperature;
    sigmaTempLong =   uc.sigmaTemp;
    // Of short immersion depth
    uc.average(pointNumber, startShort, endShort, inDirShort);
    omegaShort =       uc.omega;
    sigmaOmShort =     uc.sigmaOm;
    torqueShort =      uc.torque;
```

```
sigmaTorqueShort = uc.sigmaTorque;
tempShort =        uc.temperature;
sigmaTempShort =   uc.sigmaTemp;

// From average values calculate the difference of
// the two immersion depths.
omega =       new double[pointNumber];
sigmaOm =     new double[pointNumber];
torque =      new double[pointNumber];
sigmaTorque = new double[pointNumber];
temperature = new double[pointNumber];
sigmaTemp =   new double[pointNumber];
sigmaOm =     new double[pointNumber];
sigmaTorque = new double[pointNumber];
sigmaTemp =   new double[pointNumber];
uc.torqueDiff(pointNumber,
        omegaLong, omegaShort,
        torqueLong, torqueShort,
        tempLong, tempShort,
        omega, torque, temperature,
        sigmaOmLong, sigmaOmShort,
        sigmaTorqueLong, sigmaTorqueShort,
        sigmaTempLong, sigmaTempShort,
        sigmaOm, sigmaTorque, sigmaTemp);

boolean smallEnough;
double scaledTorque, oldValue;
double impletionDepth;
int n;
gammaDot =       new double[pointNumber];
tau =            new double[pointNumber];
sigmaGammaDot =  new double[pointNumber];
sigmaTau =       new double[pointNumber];
viscosity =      new double[pointNumber];
sigmaViscosity = new double[pointNumber];

for(i=0; i<pointNumber; i++)
{
    double l = uc.lambda(lambda,temperature[i]);
    sls = uc.sigmaLambdaS(temperature[i],RiRoom,
                          RoRoom,sigmaTemp[i]);

    // Process trust interval of torque
    if( i==0 )
    {
```

```
    sigmaTorque[i] = Math.sqrt(
        sigmaTorque[i]*sigmaTorque[i] +
        Math.pow(trustI*torque[0], 2.) +
        Math.pow(trustI*(torque[1] -
                         torque[0]), 2.));
}
else if( i == pointNumber-1 )
{
    sigmaTorque[i] = Math.sqrt(
        sigmaTorque[i]*sigmaTorque[i] +
        Math.pow(2.*trustI*(torque[i] -
                            torque[i-1]),2));
}
else
{
    sigmaTorque[i] = Math.sqrt(
        sigmaTorque[i]*sigmaTorque[i] +
        Math.pow(trustI*(torque[i+1] -
                         torque[i]), 2) +
        Math.pow(trustI*(torque[i] -
                         torque[i-1]), 2));
}

smallEnough = false;

// Calculate the shear rate
n = 0;  gammaDot[i] = 0.;
while( !smallEnough )
{
    oldValue = gammaDot[i];
    scaledTorque = Math.pow(1, n)*torque[i];
    gammaDot[i] += scaledTorque*
        uc.linearSlopeApprox(torque, omega,
                             scaledTorque,
                             pointNumber);
    if((gammaDot[i] - oldValue)/gammaDot[i]
       < 0.00000001)
    {
        smallEnough = true;
    }
    n++;
}
gammaDot[i] *= 2.;

// Error of the shear rate
```

```
int j, j_min;
double temp = 0.;
// Error contribution of torque
scaledTorque = torque[i];                                    115
smallEnough = false;
j = 1; j_min = 0;
while( !smallEnough )
{
    scaledTorque *= l;                                       120
    temp += Math.pow(l, j)*
            Math.abs(
                uc.linearSlopeApprox(
                    torque,
                    omega,                                   125
                    scaledTorque,
                    pointNumber));

    temp += torque[i]*Math.pow(l, 2*j)*
                Math.abs(                                    130
                    uc.curvatureApprox(
                        torque,
                        omega,
                        scaledTorque,
                        pointNumber));                       135
    if( scaledTorque < torque[0] )
    {
        smallEnough = true;
        j_min = j+1;
    }                                                        140
    j++;
}
temp += Math.pow(l, j_min)/(1.0/l - 1.0)*
            Math.abs(
                uc.linearSlopeApprox(                        145
                    torque,
                    omega,
                    0.5*torque[0],
                    pointNumber)) +
        Math.pow(l, 2*j_min)/(1.0/(l*l)-1.0)*                150
            torque[i]*Math.abs(
                uc.curvatureApprox(torque,
                    omega, 0.5*torque[0],
                    pointNumber));
sigmaGammaDot[i] = Math.pow(2*temp*                          155
                    sigmaTorque[i], 2);
```

```
temp = 0.;
scaledTorque = torque[i];
smallEnough  = false;
j = 1; j_min = 0;

while( !smallEnough )
{
    scaledTorque *= l;
    temp += j*Math.pow(l, j-1)*
                Math.abs(
                    uc.linearSlopeApprox(
                        torque,
                        omega,
                        scaledTorque,
                        pointNumber));
    temp += torque[i]*j*Math.pow(l, 2*j-1)*
                Math.abs(
                    uc.curvatureApprox(torque,
                        omega, scaledTorque,
                        pointNumber));

    if( scaledTorque < torque[0] )
    {
        smallEnough = true;
        j_min = j+1;
    }
    j++;
}

temp += Math.pow(l, j_min)*
            (j_min*(1.0 - l) - 1.0)/
            ((1.0 - l)*(1.0 - l))*
            Math.abs(
                uc.linearSlopeApprox(torque,
                    omega, 0.5*torque[0],
                    pointNumber)) +
        Math.pow(l, 2*j_min + 1)/
            ((l*l - 1)*(l*l - 1))*
            (1.0 - j_min*(l*l - 1.0))*torque[i]*
            Math.abs(
                uc.curvatureApprox( torque,
                    omega, 0.5*torque[0],
                    pointNumber));
sigmaGammaDot[i] += Math.pow(2.0*torque[i]*
                            temp, 2)*sls;
```

```
            sigmaGammaDot[i] = Math.sqrt(sigmaGammaDot[i]);

            // Calculate the stress
            double Ri = uc.Ri(temperature[i], RiRoom);
            impletionDepth = immersion/(1 - l);
            tau[i] = torque[i]/(2*Math.PI*Math.pow(Ri, 2.)
                            *impletionDepth);

            // Error of the stress
            sigmaTau[i] = 0.;
            sigmaTau[i] = Math.pow(tau[i]*sigmaTorque[i]/
                                   torque[i], 2);
            sigmaTau[i] += Math.pow(2.0*tau[i]/Ri, 2)*
                            uc.sigmaRiS(RiRoom,
                                    temperature[i],
                                    sigmaTemp[i]);

            sigmaTau[i] += Math.pow(tau[i]/
                                    impletionDepth, 2)*(
                                Math.pow(
                                    impletionDepth/
                                        immersion*0.0001,
                                    2) +
                                Math.pow(impletionDepth*
                                    impletionDepth/immersion,
                                    2) * sls);
            sigmaTau[i] = Math.sqrt(sigmaTau[i]);

            // Calculate viscosity
            viscosity[i] = tau[i]/gammaDot[i];

            // Error of viscosity
            sigmaViscosity[i] = Math.pow(sigmaTau[i]/
                                         gammaDot[i], 2.);
            sigmaViscosity[i] += Math.pow(tau[i]/
                                    (gammaDot[i]*gammaDot[i])
                                    *sigmaGammaDot[i], 2.);
            sigmaViscosity[i] = Math.sqrt(sigmaViscosity[i]);
            }
        // Tell VC_Frame that calculation has finished.
        finished = true;
    }
```

Maxwell Fluid: Explicit Values C.3

Figure C.2 gives an overview of the dat flow and structure of the program `viscoelastic`, wich calculates explicit values of the Maxwell boundary value problem given in equation (4-5). For speed reasons the code is written in C, and is hence functional based. Basically, the roots q_j of equation (A-22) are calculated (`FZeros`) for a given geometry. The root finding algorithm used is described in the next section (page 82). It remains the – basically – straight forward implementation of the solutions (4-4) and (4-5) of the boundary value problem by calculating the normalizing factors N_j given in equation (A-23)(`calc_Nj`) and corresponding scalar products (`scalar_A0`, `scalar_As`). These values are inserted in the solutions u (`calc_u`) and v (`calc_v`), which then define the complete solutions $\omega(r,t)$ and $\tau(r,t)$. `viscoelastic` stricktly employs the ANSI C standard. For a serious implementation of the Bessel functions the routines are linked to the Gnu Scientific Library [23].

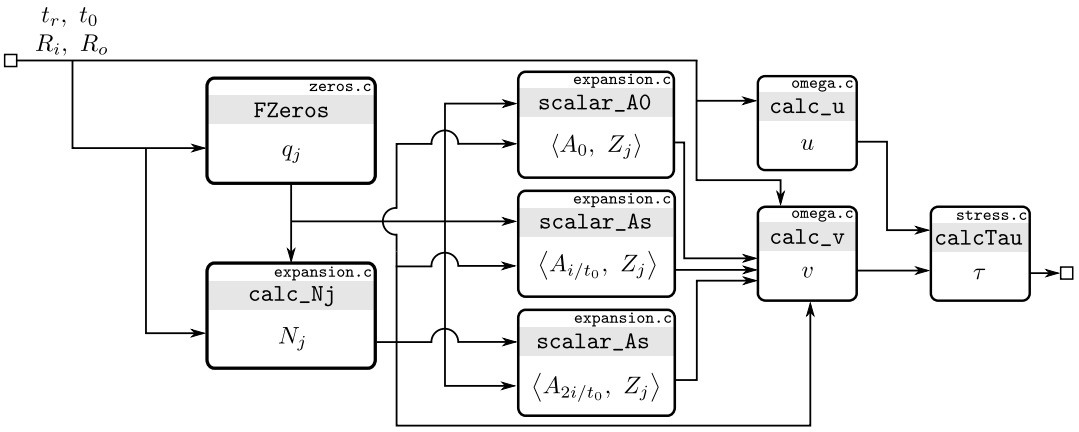

Figure C.2: *Overview of `viscoelastic`, which calculates explicit values of solution 4-5 of the Maxwell material boundary value problem. Functions processing the data are represented by boxes. Their names are underlayed with a grey background. They can be found in the source files indicated in the upper right corner of each box.*

C.3.1 Determination of zeros

The solutions q_j of equation (A-22) will be determined with help of the bisection method [48]. It might not be the fastest, but the most stable routine the author is aware of.

```
#include <math.h>
#include <gsl/gsl_sf_bessel.h>

double Fj(double Ro, double k)
{
   /*********************************************
   * Returns a function with the same zeros as the
   * linearly independent solutions satisfying the
   * boundary value problem F(1) = F(Ro) = 0
   *********************************************/
   return gsl_sf_bessel_J1(Ro*k)*gsl_sf_bessel_Y1(k)
           - gsl_sf_bessel_J1(k)*gsl_sf_bessel_Y1(k*Ro);
}

int refineInterval(double * A,
                   double * B,
                   double Ro,
                   short precision)
{
   /*************************************************
   * Refine intervals of sign change to given precision
   * with the bisection method. Every 100 steps the
   * precision is evaluated.
   *************************************************/
   int i;
   double left, right;
   left = *A;
   right = *B;
   double x, relative, error;
   error = pow(10.0, -1.0*(double)(precision));
   relative = fabs((right - left)/left);
   while( relative > error )
   {
      i = 0;
      while(i < 100)
      {
         if( Fj(Ro, left)
            *Fj(Ro, (x = .5*(left + right))) < 0 )
            right = x;
```

```
         else
            left = x;
         i++;
      }
      relative = fabs((right - left)/left);
   }

   *A = left;
   *B = right;
   if(error <= relative) return 0; else return -1;
}

int FZeros(const double Ro,
           const long j_max,
           double zeros[])
{
   /*********************************************
    * Find intervals where the sign of Fj changes.
    * Call the refine function and after that
    * write result to the 'zero[]' array.
    *********************************************/
   long j;           // Iterators
   int i;
   double interval;
   int steps;        // Number of steps
   int refineState;

   steps = 100;
   // Initial guess of zero:
   interval = 3.2/(Ro - 1.0);
   double x_old = interval/((double)(steps));
   double x;

   for(j=0; j<j_max; j++)
   {
      i = 0;
      x = x_old + interval/((double)(steps));

      // Bracket next change in sign of F
      while( Fj(Ro, x_old)*Fj(Ro, x) > 0 )
      {
         x_old = x;
         x += interval/((double)(steps));
         i++;
      }
```

```
        i = 0;
                                                                    87
        // Refine roots to a precision of 1 e-15
        refineState = refineInterval(&x_old, &x, Ro, 15);

        // Store result
        zeros[j] = x;                                               92

        // Update x_old
        x_old = x;

        // Update interval to difference between last zeros         97
        if( j > 0 ) interval = zeros[j] - zeros[j-1];
        else interval = zeros[0];
    }
    return 0;
}                                                                   102
```

C.4 Source Code and Executables

Since a listing of the complete code that was written would fill too much space, a compact disc was appended to this document. The disc contains the complete source code and additional documentation of the programs `VC` and `viscoelastic`.

VC was written using the Java development tool Netbeans (`www.netbeans.org`) in version 6.7.1. It requires a Java runtime environment in version 1.6 or later. The executable Java archive (`VC.jar`) of `VC` can be found in the folder `VC_exec` on the CD. The souce code lies in the folder `VC_dev/vc-sources`. The rest of the folder is a standard structure created by NetBeans. The folder `VC_dev/dist` contains the executables and can be copied to other locations. It contains the subfolder `javadoc` which holds Some documentation about the source code in htm format. The Java archive can be executed by submitting the command `java -jar VC.jar` to the operating system (e.g. on the command line). The calculation part is started with the 'calculate' button in the main window. After basic questions about the experimental geometries the experi-

mental data can be read. The format must be an ascii file for each measured velocity with the name 'n`.txt`', where n stands for a number between 1 and the number of measured speeds, and 1 corresponds to the lowest speed. The data file must not contain any comments, and each line must be of the format

$$'f/\mathrm{Hz} <\mathrm{tab}> N/\mathrm{Nm} <\mathrm{tab}> T/^{\circ}\mathrm{C}' \quad .$$

viscoelastic was written in C. It consists of the 5 source files `zeros.c`, `expansion.c`, `omega.c`, `stress.c`, and `testMain.c`. The corresponding header files (`.h`) of the first 4 sources are also part of the program. The files can be found in the folder `viscoelastic` on the disk. Apart from a working C compiler the source code depends on the Gnu Scientific Library [23] (`www.gnu.org/software/gsl/`). The folder `viscoelastic/Debug` contains binary executables which were build on a computer running a standard Ubuntu 9.10 Linux `x86_64` installation. For the sake of numerical simplicity the calculation is carried out using dimensionless quantities for time and position:

$$r \rightarrow \bar{r} = r/R_i \quad , \quad t \rightarrow \bar{t} = t/t_b \quad , \tag{C-1}$$

where t_b is chosen appropriately, so that the wave speed c expressed in the new coordinates equals unity. Equation (4-3) expressed in this coordinates reads

$$\ddot{\omega} + \frac{\dot{\omega}}{\bar{t}_r} = \frac{3}{\bar{r}} + \omega'' \quad , \tag{C-2}$$

where $\dot{} = \partial/\partial\bar{t}$, and $' = \partial/\partial\bar{r}$. `viscoelastic` needs 8 arguments on the command line:

1. `basedir` – folder where to write the data,
2. `Ro` – outer Couette radius $\bar{R}_o$,
3. `to` – acceleration time $\bar{t}_0$,
4. `tr` – relaxation time $\bar{t}_r$,
5. `i_max` – number of roots to search, Determines the expansion level,
6. `j_max` – number of time steps,
7. `r` – position $\bar{r}$,
8. `t_max` – upper time limit.

Appendix D

Publications

The following pages show two articles which were published in the course of this thesis.

GEOPHYSICAL RESEARCH LETTERS, VOL. 33, L02303, doi:10.1029/2005GL024240, 2006

Non-Newtonian viscosity of basaltic magma

I. Sonder, B. Zimanowski, and R. Büttner

Physikalisch Vulkanologisches Labor, Institut für Geologie, Universität Würzburg, Germany

Received 18 July 2005; revised 20 October 2005; accepted 7 December 2005; published 18 January 2006.

[1] Basaltic melt drives most of earth's volcanism. Understanding its rheology is crucial for any model of magma transport and volcanic eruption. Basaltic magma is generally treated as a quasi Newtonian liquid, but there are observations of Non-Newtonian behaviour. With a method, that allows measurement of Non-Newtonian viscosity of a representative melt (molten basaltic rock), we found a strong shear rate dependency of viscosity in a wide range of temperatures. The temperature-viscosity dependency indicates properties of the molten phase as the cause. The viscosity data are in good agreement with a power law model. **Citation:** Sonder, I., B. Zimanowski, and R. Büttner (2006), Non-Newtonian viscosity of basaltic magma, *Geophys. Res. Lett.*, *33*, L02303, doi:10.1029/2005GL024240.

[2] Basaltic volcanism is caused by the production of magma in the mantle or the deep crust in depths between 20 and more than 500 km, and its consequent transport to the surface. This magma is a complex fluid, consisting of a molecular melt and crystals (sub-liquidus system). In addition, gas bubbles can be present, due to the exsolution of volatiles caused by the pressure drop during the transport from the source region to the surface. The violence of volcanic eruptions is strongly controlled by the flux rate, i.e., by the volume of magma transported to the surface per unit time, not only because of the increase of thermal energy input but also because of the increasing degree of disequilibrium in respect to overheat and volatile overpressure. However, the rheology of magma still is poorly understood. In fact, there is not even a solid physical model for the simplest case of a lava flow at the surface. The key parameter, describing the rheology, is the viscosity. It is generally accepted that magma is a Non-Newtonian liquid; that is, the relationship between strain rate and shear stress cannot be described by a linear dependency [e.g., *Bottinga*, 1994; *Stein and Spera*, 1998]. However, high quality measurements of viscosity so far are still referenced to as Newtonian viscosities. Alternative rheology models are numerous [e.g., *James et al.*, 2004], but experimental methods for the measurement of Non-Newtonian viscosities of inhomogeneous material at high temperatures are generally lacking. In this letter we describe a method to measure the viscosity of a representative basaltic melt independent of flow field assumptions.

[3] For empirical determination of flow curves, materials of viscosities comparable to basaltic melts usually are sheared in a so called narrow gap arrangement (e.g., searle-type, cone and plate, parallel plates). If the gap is narrow enough, compared to the other dimensions of the experiment, and still wide enough to fully contain all sources of internal friction, the shear rate can be treated as constant and thus the shear stress/shear rate ratio can be measured directly. Such methods run into problems when applied to inhomogeneous materials, such as a magmatic melt that contains crystals and gas bubbles. In order to measure the bulk viscosity of a low viscosity magma, the gap in the experimental device must be in the order of 0.01 m. To get narrow gap conditions, e.g., for a rotational viscometer, the radii of container and rotational body would have to be in the order of 1 m. This exceeds laboratory scales, especially at magmatic temperatures. The only solution is to accept a wide gap arrangement, however, current wide gap techniques are not model independent [*Bird et al.*, 1987]. The experimental set-up used for the measurements presented here, is a modification of a high temperature viscometer that has been in use for standard measurement of apparent Newtonian viscosities (DIN 53019) in our Laboratory [*Zimanowski et al.*, 2004; *Büttner et al.*, 2000, 1998]. It consists of a Haake™ Sensor connected via a spindle rod to a rotating body which couples to the melt. The melt is contained in ceramic crucibles. The thermal stability of the furnace is better than 1K, the absolute accuracy better than 2.5 K. Only the geometry of the rotational body was modified as shown in Figure 1, ensuring a high cylindrical symmetry. The material selected for this study was a basaltic rock, representative for continental basaltic lava flows that has already been used in other studies [*Zimanowski et al.*, 2004]. The rock sample was granulated and a portion of 0.2 kg was filled into the crucible. All experimental runs were carried out in a quasi static argon atmosphere. The mechanical coupling of the melt to the crucible and the rotational body is good (full wettability) and thus slip effects [*Barnes*, 1995] can be neglected. In the investigated temperature range between 1450 and 1500 K a temperature independent crystal content of approx. 5 Vol. % Olivine crystals is present [*Zimanowski et al.*, 2004]. The sensor measures the torque N acting on the rotating body at a constant angular velocity ω. The torque was recorded until it was found to be constant in time. To minimize end effects on the rotating body each measurement was carried out twice for two different immersion depths (see Figure 1).

[4] The evaluation of the measured data is based on the idea of I.L. Krieger and H. Elrod [*Krieger and Elrod*, 1953]. In cylindrical coordinates the shear rate is

$$\dot{\gamma} = r \frac{\partial \omega}{\partial r},$$

where r is the distance from the z-axis. The shear rate can be calculated from the interdependence of the measured data pairs (N, ω) as

$$\dot{\gamma} = 2 \sum_{i=0}^{\infty} \tilde{N} \frac{\partial \omega}{\partial \tilde{N}}\Big|_{\tilde{N}=\lambda^i N} \quad . \tag{1}$$

0094-8276/06/2005GL024240$05.00

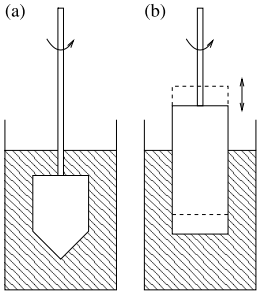

Figure 1. (a) Searl type viscometer for Newtonian fluids (DIN 53019). (b) Viscometer for Non-Newtonian fluids. It is necessary to measure at two different immersion depths.

Here $\lambda = (R_i/R_o)^2$ denotes the squared ratio of the radii of the rotating body and the crucible walls, respectively. Equation (1) contains a derivative of the measured relation $\omega(N)$. By assuming a specific rheologic model, one can calculate this derivative analytically. Since it is not our intention to assume a model, we determine it empirically by numerical calculation of this derivative from the measured data. As long as λ is small enough, the sum (1) converges. The smaller λ the faster the sum converges telling us that this method gains accuracy with increased gap size.

[5] The shear stress is determined from the torque by

$$\tau = \frac{N}{2\pi R_i^2 L} \quad ,$$

where L is the immersion depth of the cylinder in the fluid. These relations enable us to determine the viscosity η from the measured data pairs (N, ω) as

$$\eta = \frac{\tau}{\dot{\gamma}} \quad .$$

[6] The method was successfully tested (see Figure 2) using two homogeneous materials with known viscosities [*Liberatore et al.*, 2003], a Newtonian silicon calibration oil (Wacker AK 10000), and a polymer-water solution with a strong Non-Newtonian character (Ciba™ Magnafloc™ 1011). Now the method was applied to measure viscosities of the basaltic melt. The melt was measured at temperatures of 1448, 1458, 1473, and 1498 K. Results are given in

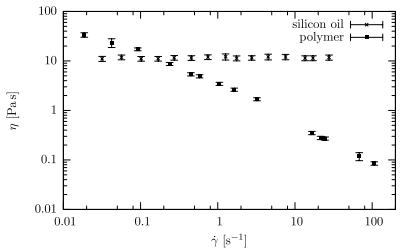

Figure 2. Viscosities of a Newtonian silicon calibration oil (Wacker AK 10000) and a 0.4% Magnafloc™ 1011 solution in purified water.

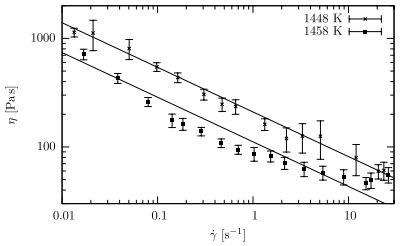

Figure 3. Viscosity of basalt at 1448 and 1458 K. The lines are viscosity calculations from a power law model, equation (2) for c = 210 Pa s^m, m = 0.588 at 1448 K, and c = 111 Pa s^m, m = 0.588 at 1458 K.

Figures 3 and 4. The obtained viscosities show a surprisingly strong dependency on the shear rate. In the measured range ($\sim 10^{-2}$ s^{-1} – 30 s^{-1}) viscosity decreased by a factor of 10. A strain rate interval with quasi Newtonian behaviour cannot be assigned to this material. Comparing the measured data with existing models, a power law model seems to be the most suitable one (Figures 3 and 4)

$$\tau = \tau_0 \left(\frac{\dot{\gamma}}{\dot{\gamma}_0}\right)^m = c\,\dot{\gamma}^m \quad . \qquad (2)$$

It is remarkable that the exponent of equation (2) does not vary dramatically at different temperatures. Thus in a first approximation the temperature dependency within the investigated range can be assigned to the proportionality factor c. Figure 5 shows the temperature dependency of c which is in good agreement with an exponential $\sim \exp\left(\frac{E}{k_B T}\right)$. Therefore, we expect Non-Newtonian behaviour also for temperatures exceeding the investigated range.

[7] The Non-Newtonian character of the investigated basaltic melt seems to originate from properties of the molten phase because influences of crystals within the investigated temperature range can be neglected. Also, in the latter case one would expect the power-law index m to depend stronger on temperature than the proportionality factor c. Our measurements demonstrate that it is inevitable to measure viscous behaviour of magmatic melts beyond the Newtonian models (which still dominate current simula-

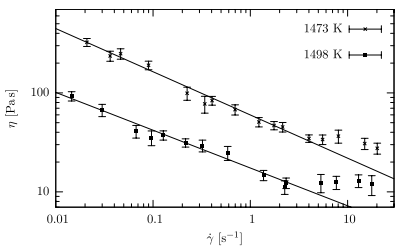

Figure 4. Viscosity of basalt at 1473 and 1498 K. The lines are viscosity calculations from a power law model, equation (2) for c = 59.9 Pa s^m, m = 0.563 at 1473 K, and c = 17.4 Pa s^m, m = 0.618 at 1498 K.

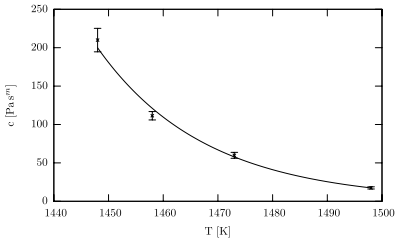

Figure 5. Temperature dependency of the power law model: Proportionality factor c plotted vs. temperature. The fitted curve is an exponential exp $\left(\frac{E}{k_B T}\right)$.

tions). The bad news for the current models of magma transport and lava flow are, that even for low viscosity, crystal poor basaltic melts, a quasi Newtonian behaviour cannot be applied. The good news, however are, that the measured data nicely fit into a power-law model with a standard exponential temperature dependency, that can be separated and used for general modelling.

[8] **Acknowledgments.** We would like to thank Thermo Electron Corporation for the provision of the Haake™ instrument, and Wacker Chemie GmbH, and Ciba a for the silicon oil and the polymer.

References

Barnes, H. A. (1995), A review of the slip (wall depletion) of polymer solutions, emulsions and particle suspensions in viscometers: Its cause, character, and cure, *J. Non Newtonian Fluid Mech.*, *56*, 221.

Bird, R. B., R. C. Armstrong, and O. Hassager (1987), *Dynamics of Polymeric Liquids*, 2nd ed., John Wiley, Hoboken, N. J.

Bottinga, Y. (1994), Configurational entropy and the non-Newtonian rheology of homogeneous silicate melts, *Phys. Rev. B*, *49*(1), 95.

Büttner, R., B. Zimanowski, J. Blumm, and L. Hagemann (1998), Thermal conductivity of a volcanic rock material (olivine-melilitite) in the temperature range between 288 and 1470 K, *J. Volcanol. Geotherm. Res.*, *80*, 293.

Büttner, R., B. Zimanowski, C. Lenk, A. Koopman, and V. Lorenz (2000), Determination of thermal conductivity of natural silicate melts, *Appl. Phys. Lett.*, *77*(12), 1810.

James, M. R., N. Bagdassarov, K. Müller, and H. Pinkerton (2004), Viscoelastic behaviour of basaltic lavas, *J. Volcanol. Geotherm. Res.*, *132*, 99.

Krieger, I. M., and H. Elrod (1953), Direct determination of the flow curves of non-Newtonian fluids, *J. Appl. Phys*, *24*(2), 134.

Liberatore, M. W., E. J. Pollauf, and A. J. McHugh (2003), Shear-induced structure formation in solutions of drag reducing polymers, *J. Non Newtonian Fluid Mech.*, *113*, 193.

Stein, D. J., and F. J. Spera (1998), New high-temperature rotational rheometer for silicate melts, magmatic suspensions, and emulsions, *Rev. Sci. Instrum.*, *69*(9), 3398.

Zimanowski, B., R. Büttner, and A. Koopmann (2004), Experiments on magma mixing, *Geophys. Res. Lett.*, *31*, L09612, doi:10.1029/2004GL019687.

R. Büttner, I. Sonder, and B. Zimanowski, Physikalisch Vulkanologisches Labor, Institut für Geologie Pleicherwall 1, D-97072 Würzburg, Germany. (sonder@geologie.uni-wuerzburg.de)

JOURNAL OF GEOPHYSICAL RESEARCH, VOL. 111, B08204, doi:10.1029/2005JB003958, 2006

Stress-induced brittle fragmentation of magmatic melts: Theory and experiments

Ralf Büttner,[1] Pierfrancesco Dellino,[2] Hannes Raue,[1] Ingo Sonder,[1] and Bernd Zimanowski[1]

Received 25 July 2005; revised 29 December 2005; accepted 16 May 2006; published 24 August 2006.

[1] The release of kinetic energy during explosive volcanic eruptions is a key parameter for hazard assessment and civil defense. The explosive production of volcanic ash by intensive fragmentation of magma and host rocks represents a substantial part of this energy. For cases of explosive eruption where predominantly host rock was fragmented (phreatomagmatic eruptions) to form the major part of volcanic ash, rock mechanical parameters could be measured and fragmentation energies assigned. In cases where most of the produced ash is of juvenile origin (magmatic eruptions) a general method for the determination of fragmentation energy is still lacking. In this article we introduce a thermodynamic approach that relates grain size data of the produced ash deposits to shear rates acting during the deformation of magma. With the use of a standardized fragmentation experiment the physical parameters needed to determine the specific fragmentation energy and deformation history were measured. The experiment was calibrated and tested with two case histories of the Campi Flegrei volcanic field (southern Italy). Both eruptions are classified as "most probable worst-case scenarios" during the next period of activity, to be expected within the next 10–100 years. Using the experimentally determined specific fragmentation energies, the total mass of produced ash of each eruption, and assuming an energy dissipation as observed in the experiments, the total kinetic energy release of the worst-case Campi Flegrei eruptive events to come were calculated with 25 and 40 kt TNT equivalent.

Citation: Büttner, R., P. Dellino, H. Raue, I. Sonder, and B. Zimanowski (2006), Stress-induced brittle fragmentation of magmatic melts: Theory and experiments, *J. Geophys. Res.*, *111*, B08204, doi:10.1029/2005JB003958.

1. Introduction

[2] Explosive volcanic eruptions are characterized by the release of kinetic energy on a short timescale. The fingerprint of such eruptions is the production of significant amounts of fine fragments (volcanic ash) by brittle mode fragmentation processes [*Bottinga*, 1994; *Zimanowski et al.*, 2003]. These ash fragments, especially in the grain size range between 20 and 150 μm [*Heiken and Wohletz*, 1985; *Dellino and LaVolpe*, 1995], not only bear information on the quality of the fragmentation processes [*Zimanowski et al.*, 1997a; *Büttner et al.*, 1999] but also on the kinetic energy needed for their production [*Büttner et al.*, 2002]. If the total amount of fragments generated during one discrete eruption can be determined and if the specific fragmentation energy (energy per unit mass) for all fragment populations within the respective deposit is known from experimental studies, the total amount of fragmentation energy consumed during this eruption can be calculated. This value is useful to classify the eruption and to calibrate numerical simulations. Furthermore, as the dissipation of kinetic energy (i.e., the proportional allotment of fragmentation energy, pressure wave or shock wave energy, seismic or acoustic energy, ejection and transport energy) can be modeled or at least assumed, the total amount of kinetic energy released and the conversion rate from the thermal energy of the erupted magma batch can be approximated. This will significantly improve the evaluation of specific eruptions in respect to their hazard potential.

[3] A method to determine the specific fragmentation energy for explosive eruptions of basaltic volcanism (particularly with regard to phreatomagmatic explosion) has been already introduced by the authors [*Zimanowski et al.*, 1997a, 1997b; *Büttner et al.*, 1999] and tested for the case of deposits of La Fossa di Vulcano [*Büttner et al.*, 2002]. *Raue* [2004] applied an alternative method to lithic fragments, i.e., ash sized fragments that were produced during explosive phreatomagmatic volcanic eruptions by fragmentation of solid rock that hosted the volcanic edifice. He could demonstrate that the amount of energy needed to explain the production of these lithic fragments is in good agreement with the amount of kinetic energy derived from the evaluation of the respective magmatic ash fragments following the method of *Büttner and Zimanowski* [1998]. As explo-

[1] Physikalisch Vulkanologisches Labor, Universität Würzburg, Würzburg, Germany.
[2] Dipartimento Geomineralogico, Universitá degli Studi di Bari, Bari, Italy.

0148-0227/06/2005JB003958$09.00

sive phreatomagmatic eruptions are characterized by a substantial proportion of lithic fragments [*Zimanowski*, 1998], a combination of both methods leading to converging results is a good test to verify the results in these cases.

[4] In this paper we present a general method to determine the specific fragmentation energy for fragments created by all types of explosive eruptions, also useful for intermediate magma and silica rich compositions, applied as a case history to samples from deposits of volcanic centers of the Campi Flegrei caldera in southern Italy.

2. Theory of Brittle Fragmentation

[5] In contrast to hydrodynamic fragmentation processes [e.g., *Chandrasekhar*, 1968], a general analytical solution for brittle type fragmentation processes does not exist [e.g., *Herrmann and Roux*, 1990]. If large amounts of macroscopic particles are produced, as is the case for volcanic ash, thermodynamic statistical methods, following the approach of *Yew and Taylor* [1994], can be applied under the following assumptions: (1) a solid body breaks up due to internal stress, i.e., thermodynamic equilibrium is not achieved during crack growths within the solid body, but until after fragmentation into n particles, (2) isothermal conditions prevail during fragmentation, (3) surface energy is not recoverable, i.e., the entropy of the system grows, and (4) during increments of time the stress is treated as constant. Now, the free enthalpy (Gibbs thermodynamic function) G can be calculated for a solid body breaking up into n particles:

$$G = U + B - TS \tag{1}$$

where U is the internal energy of the stressed body before fragmentation, B is the total energy consumed in generating new surfaces, T is the temperature, and S is the entropy generated by the formation of new surface.

2.1. Calculation of *U*

[6] The strain energy density is defined by

$$dU = \frac{1}{2}\mu(\dot{\varepsilon}t)^2 \tag{2}$$

where μ is the bulk modulus ($\mu = \rho c^2$) with the density ρ and the speed of sound c, $\dot{\varepsilon}$ is the strain rate, and t denotes the time interval between stress onset and fragmentation.

[7] Within the time t the volume affected by the stress (traveling at the speed of sound c) is $(ct)^3$. If these volumes break independent from each other (assumption 1), the particle diameter s must satisfy

$$s \le 2ct \tag{3}$$

combining (2) and (3) results in

$$dU = \frac{1}{2}\mu\dot{\varepsilon}^2t^2 \Rightarrow dU \ge \frac{1}{2}\mu\dot{\varepsilon}^2\frac{s^2}{4c^2} \tag{4}$$

and thus for the total volume V

$$U = \int_V dU \Rightarrow U \ge \frac{1}{2}\mu\left(\frac{\dot{\varepsilon}s}{2c}\right)^2 V \tag{5}$$

using (3) and assumption 4 the fundamental description of the geometry for n particles is

$$V = n\left(\frac{4}{3}\pi\left(\frac{s}{2}\right)^3\right) = \frac{1}{6}n\pi s^3 \Rightarrow s = \left(\frac{6V}{n\pi}\right)^{1/3} \tag{6}$$

combining (6) and (5), the minimum energy can be calculated by

$$U = \frac{\mu}{8}\left(\frac{\dot{\varepsilon}}{c}\right)^2\left(\frac{6}{\pi}\right)^{2/3} n^{-2/3}V^{5/3} \tag{7}$$

2.2. Calculation of *B*

[8] The fracture surface energy per unit volume [*Grady*, 1988] is

$$dB = \frac{3I^2}{\rho c^2 s} \tag{8}$$

where I denotes the stress intensity factor, i.e., the geometry-dependent energy density that leads to the breaking of a certain material [*Lawn*, 1993]. Thus, for the total volume, V follows

$$B = \int_V dB \Rightarrow B = \frac{3I^2}{\rho c^2 s}V \tag{9}$$

and combination with (6) results in

$$B = \left(\frac{\pi}{6}\right)^{1/3}\left(\frac{3I^2}{\rho c^2}\right)n^{1/3}V^{2/3} \tag{10}$$

2.3. Calculation of *S*

[9] From semiconductor physics a solution was described by *Varotosos and Alexopoulos* [1986]

$$S = k\ln\left\{\frac{(N+n)!)}{N!n!}\right\} \tag{11}$$

where k denotes the Boltzmann constant and N is the total new surface normalized to 1.

[10] Fundamental thermodynamics demand a minimum of G in equilibrium (assumption 1), i.e., combining (7), (10), and (11) in (1)

$$\left(\frac{\partial G}{\partial n}\right)_{T,p} = 0 \tag{12}$$

In the case of the brittle fragmentation of magma, TS will be negligibly small in comparison to U and B. Therefore by inserting (7), (10), and (11) in (12) the mean particle diameter s_0 of an ash fragment can be calculated by

$$s_0 = 2\left(\frac{\sqrt{3}I}{\sqrt{2}\rho c\dot{\varepsilon}}\right)^{2/3} \tag{13}$$

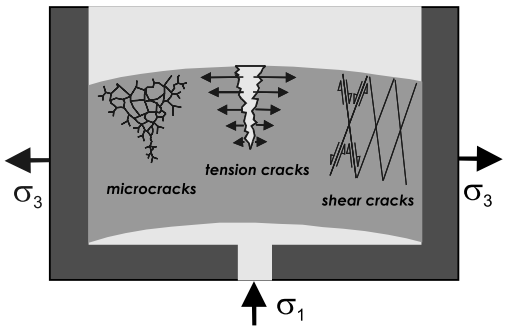

Figure 1. Schematic drawing of the experimental configuration. The stress field is indicated by the arrows, with σ_1 giving the main compression and σ_3 giving the main extension.

finally, the strain rate now can be calculated from measured ash particle properties with

$$\dot{\varepsilon} = \frac{I}{\rho c}\sqrt{\frac{12}{s_0^3}} \tag{14}$$

Now we have a tool to validate and compare fragmentation experiments and field observations of brittle type magma fragmentation using simple measurements on the produced particles.

3. Experimental Setup

[11] The basic design of the experimental configuration is a modification of the "blowout" experiment described by *Zimanowski et al.* [1997a], which also later was used to determine the ductile-brittle transition of basaltic melt [*Zimanowski et al.*, 2003]. A melt plug is generated in a cylindrical crucible and then deformed, fragmented, and ejected by a pressurized gas volume, which is introduced from below the melt plug (Figure 1). The generation of internal strain within the melt plug resembles the setting associated with lava domes and conduits [e.g., *Buisson and Merle*, 2002]. Scaling was achieved by comparison of the products with the natural analogues: volcanic ash fragments of the same chemical composition from explosive eruptions. The final design (Figure 2) features high-resolution monitoring of driving gas pressure (Kistler® 603b pressure transducer) and repulsion force (Kistler 9031A force transducer). The melt is produced in situ by inductive heating using a radio frequency generator. The melt temperature can be adjusted in a range between 1000 and 1700 K with a precision of 2 K. The driving gas volume (argon or air) is released by a high-speed solenoid. The melt mass is adjusted in such way, that the resulting aspect ratio of the melt plug equals the standards for bending tests (DIN 52 112). A standard z component seismometer is mounted onto the base plate (Figure 2) to record seismic signals. All signals are measured with a resolution of 100 kHz using a MacAdios® data acquisition board. A high-speed video system at 500 frames per second (NAC® HSV-1000) is used for the optical monitoring of the fragmentation and ejection history.

4. Origin and Composition of the Test Materials

[12] As an example of use we choose pyroclastic deposits from two eruptive centers of the Campi Flegrei caldera in southern Italy (Astroni and Agnano Monte Spina) because they are representative for recent explosive activity within the caldera [*Di Vito et al.*, 1999]. The deposits are nearly completely confined within the caldera and well exposed in the field. Thus it is possible to correlate individual layers over the whole dispersal area and to obtain a volume estimation of products of each single eruptive event. In addition, both eruptions represent the maximum expected event in a future volcanic crisis [*Dellino et al.*, 2001, 2004; *Orsi et al.*, 2004], and the knowledge of their eruptive dynamics is important for hazard assessment.

[13] The Agnano Monte Spina eruption occurred about 4.1 ka and represents the largest of the recent eruptions at Campi Flegrei. It formed the small caldera characterizing the Agnano plain at Campi Flegrei [*De Vita et al.*, 1999]. It was a mixed magmatic-phreatomagmatic eruption, augmented by a trachytic melt, and produced a complex stratigraphy resulting from a pulsating activity that led to the formation of both Plinian fallout deposits and pyroclastic density currents [*Dellino et al.*, 2001, 2004]. The total amount of erupted magma was about 1.2 km^3. The samples used in this paper come from pumiceous bombs extracted from a layer of phase B2, which represents the most widespread pyroclastic density currents of the eruption. They expanded all over the Agnano Plain area and surmounted the border of the Campi Flegrei at the Posillipo hill, toward Naples.

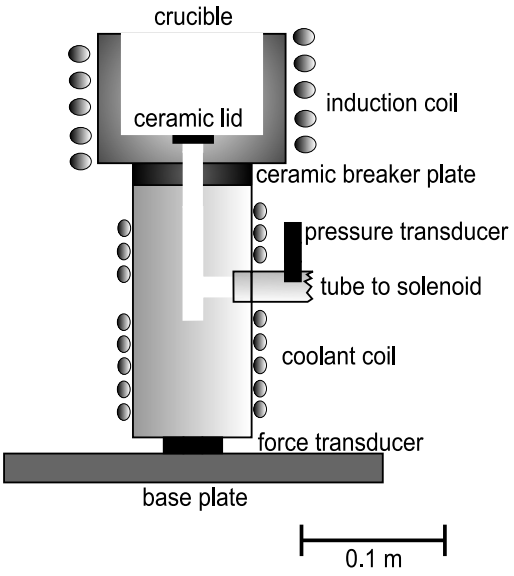

Figure 2. Scaled drawing of the experimental setup.

Table 1. Temperature-Dependent Apparent Newtonian Viscosity of the Melts Used for the Experiments

T, K	AMS η, Pa s	AST η, Pa s
1,573	1,524	1,486
1,548	2,783	2,037
1,523	3,990	2,888
1,498	6,240	4,339
1,473	9,480	6,308
1,448	14,780	9,705
1,423	23,204	15,553
1,398	37,944	24,951
1,373	64,617	-

[14] The Astroni eruptive activity was characterized by multiple eruptions which occurred in the period 4.1–3.8 ka [*Isaia et al.*, 2004]. The eruptions were of mixed magmatic-phreatomagmatic nature and were alimented by a trachytic melt. The total volume of erupted melt was about 0.45 km ^{3}, and the Astroni eruptions represent the average intensity of the recent eruptions at Campi Flegrei. In each eruption the activity was impulsive with both fallout and pyroclastic density currents events. Samples used in this paper come from pumiceous/glass rich bombs of the 6th stratigraphic unit and represent the most energetic pyroclastic density currents, which spread over the Agnano Plain.

[15] About 20 kg of unaltered bombs and lapilli were selected from each deposit, crushed (0.5 mm < granulate < 3 mm) and homogenized. The melting process (nonequilibrium melting) was adjusted in such a way, that only the matrix was molten, and the original composition of the magma in terms of phenocrysts and bubbles was maintained: the melting time was kept short in relation to the resorption time of phenocrysts and in this time, due to the high viscosity of the material the migration of bubbles was found to be negligible. A mass of 0.4 kg of granulate was molten in each run to produce the optimum plug geometry. The temperature was adjusted to 1300 K for all experiments, which is in the upper range of temperature estimations for Campi Flegrei trachytic magma [*Fulignati et al.*, 2004]. Using an inductively heated lid, the melt inside the crucible was kept thermally homogeneous. The lid was removed only a few seconds before the experiment. The apparent Newtonian viscosity of both melts was measured after DIN 53019 (Table 1). The specific density (dense rock) of quenched samples was measured after DIN 18124 at room temperature: 2492 kg m^{-3} for AMS and 2467 kg m^{-3} for AST. The porosity of the samples, measured after DIN 18125 T1, was 46.6 vol % for AMS and 49.9 vol % for AST.

5. Experimental Results

[16] If a critical driving pressure is exceeded, every experiment results in a brittle failure of the melt plug, causing formation of fragments and their rapid ejection from the crucible. At driving pressures close to the critical value, the melt plug gets deformed in a dome-like fashion (Figure 3). At the upper surface of this dome, the onset of brittle fragmentation can be observed (Figure 3a), whereas the lower surface clearly shows patterns of ductile deformation (Figure 3b). This is not a thermal effect, as the exposure time to atmospheric conditions is so short, that only a thin skin ($\ll$1 mm) is affected by cooling (the lengths of the cracks are in the cm range). The critical driving pressure at 1300 K was found to be 3.5 MPa for the AST samples and 3.0 MPa for the AMS samples.

[17] The ash-sized fragments of each fragmentation experiment were collected and compared to the natural analogues. The ash grains were found to be nearly identical in terms of grain size, shape, morphology, and chemical composition (Figure 4). The only notable difference is the lack of elongated bubbles in the experimental ash grains: In contrast to these fragments, the magma of the natural analogues was moving in a conduit, thus shear acted in transport direction onto it, prior to fragmentation. Experiments with AST and AMS resulted in different grain size distributions under identical experimental conditions

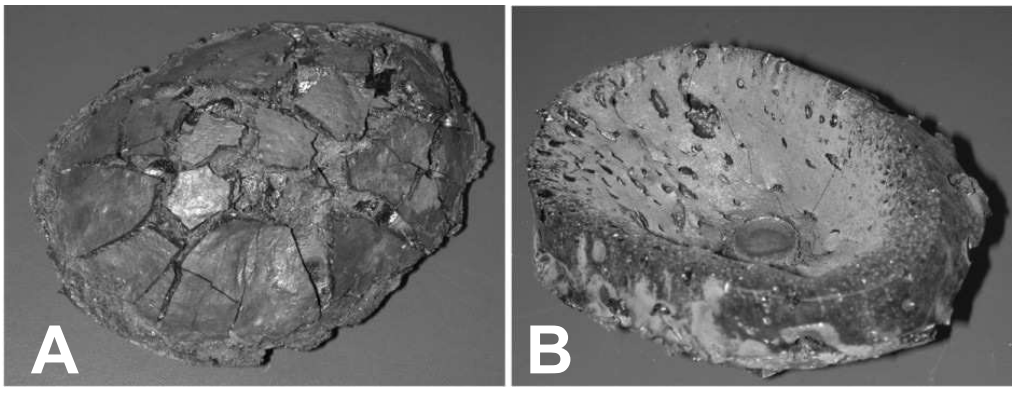

Figure 3. Pictures taken from a "failed" experiment: The melt plug with a diameter of 10 cm was deformed but not fragmented. (a) Upper side of the plug, with a cracked surface indicating a brittle reaction. (b) Lower side of the plug. In its middle the ceramic lid that sealed the gas inlet is visible. The smooth surface with elongated vesicles displays a ductile deformation behavior.

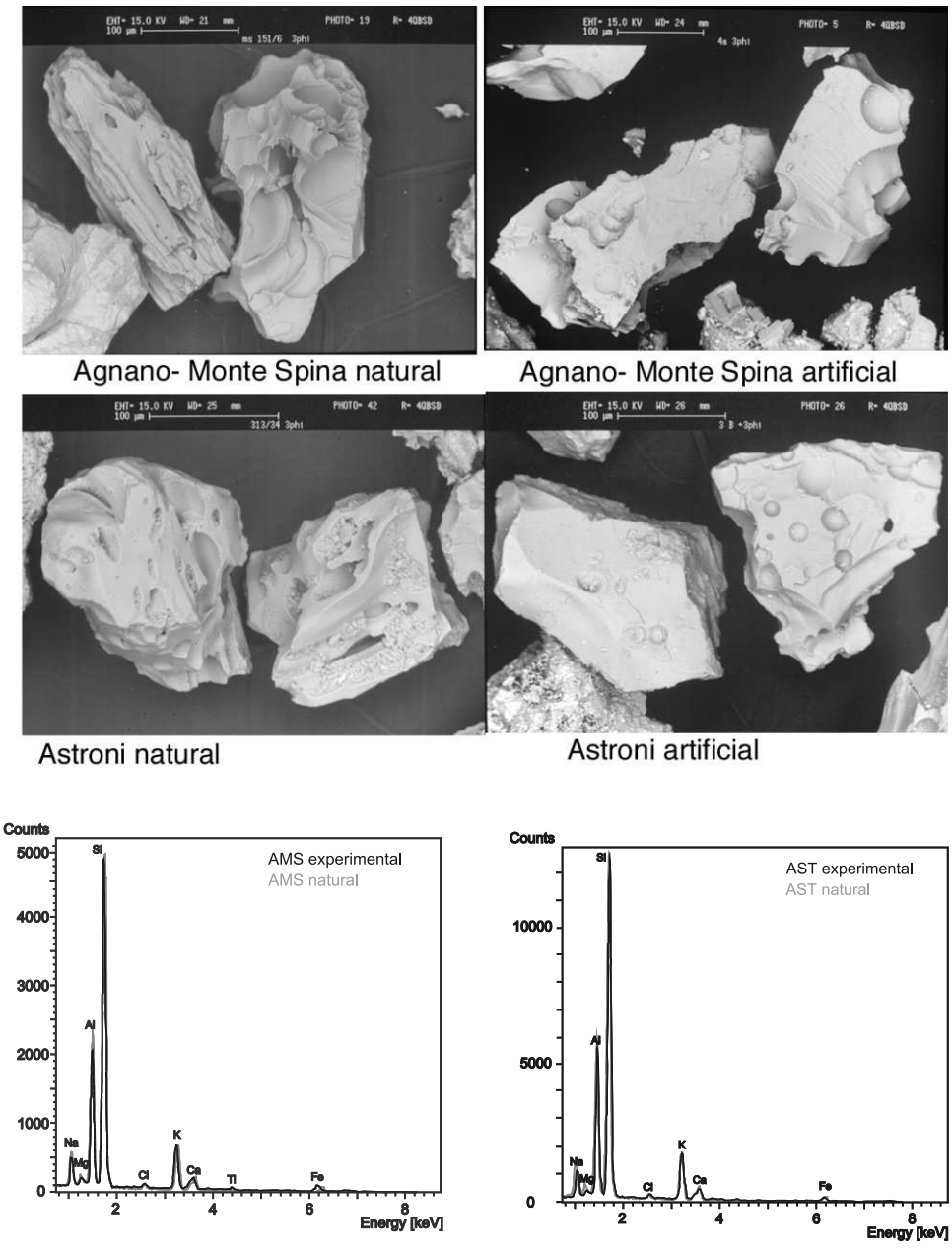

Figure 4. (top and middle) SEM pictures of experimental (artificial) and natural fragments of AMS and AST. (bottom) Results of EDX analysis of fresh glass surfaces of both compositions.

(Figure 5). Systematic variation of the driving pressure between 3 and 6 MPa yielded an increasing amount of fragments with increasing driving pressure. The grain size distribution, however, did not change with changing pressure within the statistical error. Using the BET method (nitrogen sorption), the total surface of the produced fragments was determined for the grain size fractions <360 μm. Application of standard density (DIN 18 124) and porosity

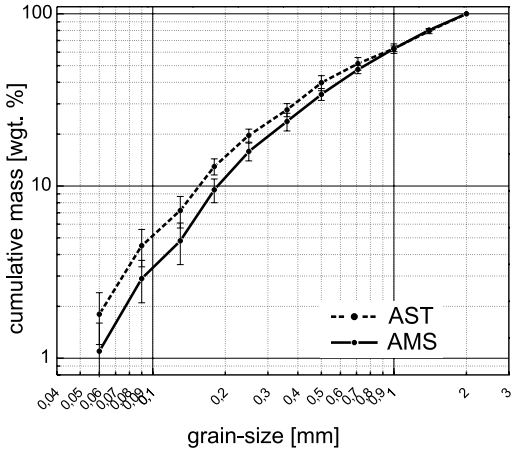

Figure 5. Plot of the grain size distributions of experimentally produced fragments of AMS and AST.

(DIN 18 125 T1) correction results in the total fracture surface. Because of the self-similarity of shapes within the ash fraction and known size fraction densities, the specific fracture surface (SFS) can be calculated for the full grain size range from the granulometric data (Table 2).

[18] From the pressure and force signals (Figure 6) the repulsion force acting on the crucible and the maximum driving pressure acting on the melt can be extracted within time increments of 10 μs. In all experimental runs (AMS and AST samples and different driving pressures) that resulted in fragmentation of the melt, the respective signal of the seismometer shows the onset (t_1) of microseismics connected to the early pressurization history and the onset of a strong seismic signal (t_2) connected to the peak of driving pressure. The records of the high-speed video system were synchronized with the data recording. Figure 7 shows three frames as an example: A at the onset of microseismics (i.e., t_1 in Figure 6), B at the end of fragmentation of the melt plug (i.e., t_2 in Figure 6), and C in the early stage of the ejection of the melt. The respective recording of the driving pressure shows the timing of the frames. Again, this example is representative for all experiments that resulted in fragmentation of the melt plug. From the high-speed video records the speed of ejection can be

Table 2. Grain-Size-Dependent Specific Fracture Surface of the Experimentally Produced Fragments

Fraction, μm	SFS AMS, $m^2\ kg^{-1}$	SFS AST, $m^2\ kg^{-1}$
	BET Measurements	
>32	527.3	453.9
>63	454.9	418.8
>90	394.5	348.9
>125	304.2	339.1
>180	289.1	249.9
>250	267.2	234.4
>360	187.5	162.2
	Model Calculations	
>500	74.2	60.4
>710	52.3	42.4
>1000	36.1	30.0
>1410	26.5	21.7

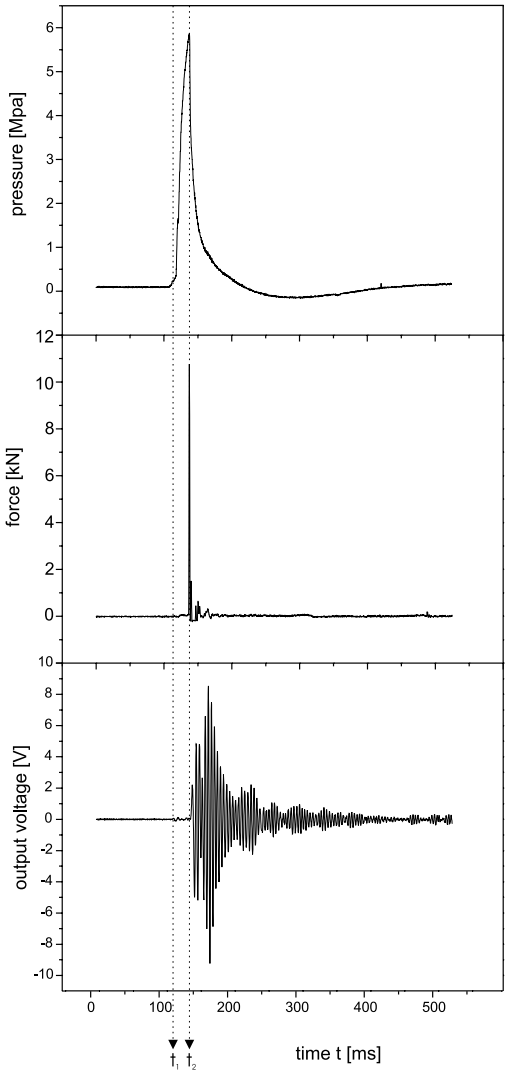

Figure 6. Example of the measured physical parameters. (top) Signal of the pressure transducer, (middle) signal of the force transducer, and (bottom) signal of the seismometer. The onset of deformation is marked by t_1 and related to the onset of microseismics; the onset of fragmentation is marked by t_2 and related to the maximum driving pressure.

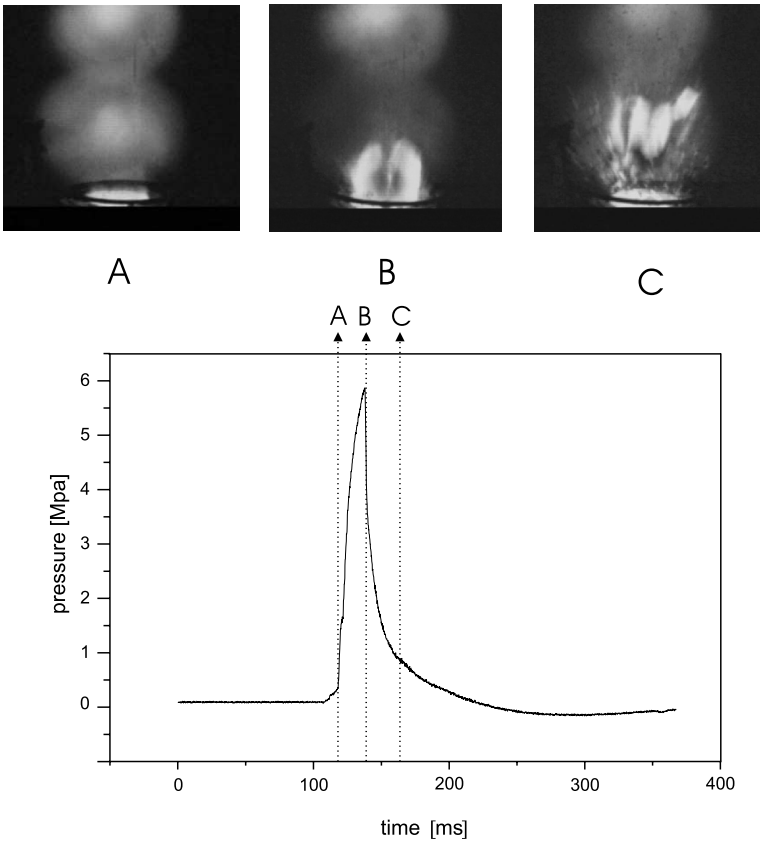

Figure 7. Example of the high-speed video recordings. (a–c) State of the experiment at the times marked A, B, and C in Figure 7 (bottom), showing the signal of the pressure transducer. Figure 7a corresponds to t_1, i.e., onset of deformation within the crucible, Figure 7b corresponds to t_2, i.e., at fragmentation and opening of the system (also see Figure 6), and Figure 7c shows a situation during the ejection of the fragmented melt plug.

obtained. In Figure 8 the deformation history of the melt plug is displayed by a typical force transducer signal. Deformation starts at t_1 (corresponding to t_1 in Figure 6 at the onset of microseismics), and ends with the total fragmentation of the plug at maximum driving pressure at t_2 (corresponding to t_2 in Figure 6). From t_2 on, the fragments are accelerated by the expanding gas until the two-phase system reaches the orifice of the crucible ("shot-gun" physics). The maximum acceleration at t_3 marks the ejection from the crucible.

6. Determination and Validation of the Strain Rate

[19] The cylindrical experimental design (Figure 1) allows the calculation of the strain rate $\dot{\varepsilon}$. The force transducer signal captured before the fragmentation event (Figure 8) represents the accelerated movement of the nonfragmented melt plug, while it is still connected to the crucible wall. The deformation of the melt plug [*Schowalter*, 1978] now can be described as an extensional flow by

$$\dot{\varepsilon} = \frac{1}{L}\frac{dL}{dt} \tag{15}$$

where L denotes the time-dependent length of a volume element. From experimental observations (e.g., Figure 3) the following deformation geometry can be assumed, representing the best fit to the observed curvatures

$$z_{1(r)} = a_1 r^2 + Z_1 \qquad z_{0(r)} = a_0 r^3 + Z_0 \tag{16}$$

where $z_{1(r)}$ describes the downside and $z_{0(r)}$ the upside surface of the plug with the central distance r, the downside apex Z_1, the upside apex Z_0, and the geometry coefficients a

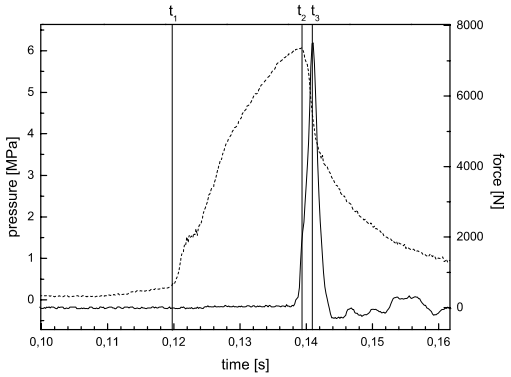

Figure 8. High-resolution plot of an example of force (straight line) and pressure (stippled line) signals during a fragmentation experiment. The onset of deformation is marked by t_1 and related to the onset of deformation (also see Figures 6 and 7), the onset of fragmentation is marked by t_2 and related to the maximum driving pressure, the maximum acceleration of the fragmented system at the orifice of the crucible is marked by t_3.

(see Figure 9). The boundary conditions at the crucible wall are $z_{1(R)} = 0$ and $z_{0(R)} = h$, with the initial plug height h. For the geometry coefficients this results in

$$a_1 = -\frac{Z_1}{R^2} \qquad a_0 = \frac{h - Z_0}{R^3} \tag{17}$$

with the crucible radius R. Inserting equation (17) in equation (16) results in

$$z_{1(r)} = Z_1\left(1 - \left(\frac{r}{R}\right)^2\right) \qquad z_{0(r)} = (h - Z_0)\left(\frac{r}{R}\right)^3 + Z_0 \tag{18}$$

As the melt plug volume V can be treated as constant before fragmentation, we obtain

$$\text{const} = \pi R^2 h = V_0 - V_1 = \int_0^R 2\pi r z_{0(r)} dr - \int_0^R 2\pi r z_{1(r)} dr \tag{19}$$

where V_0 and V_1 are volumes corresponding to the surfaces given in equation (16).

[20] Now the position of the downside apex can be described by

$$Z_1 = \frac{6}{5}(Z_0 - h) \tag{20}$$

The maximum strain rate now can be described as the time-dependent position of the apexes by

$$\dot{\varepsilon}_{(r=0,t)} = \frac{\dot{Z}_0 - \dot{Z}_1}{Z_0 - Z_1} = \frac{\dot{Z}_0}{Z_0 - 6h} \tag{21}$$

From the force transducer signal the momentum P can be calculated and compared to the momentum calculated from the geometry described above by

$$P_{(t)} = \int F_{(t)} dt = \int \rho \bar{\dot{z}} dV = 2\pi\rho \int \frac{1}{2}\left(\dot{z}_{0(r)} + \dot{z}_{1(r)}\right) r \left(z_{0(r)} - z_{1(r)}\right) dr \tag{22}$$

where F denotes the measured repulsion force, ρ is the density of the melt, and $\bar{\dot{z}}$ is the mean velocity of the melt plug at the distance r. Integration of equation (22) over time yields a quadratic equation with a solution for Z:

$$Z_0 = h\left(-21 \pm \sqrt{441 + \frac{400}{3}\frac{1}{Mh}\int Pdt}\right) \tag{23}$$

Here M denotes the total mass of the melt plug. Inserting equation (23) in equation (21) the maximum strain rate can be calculated and the problem is solved.

[21] We calculated $\dot{\varepsilon}$ for AMS with 50 s^{-1} and for AST with 150 s^{-1}. This result can be validated using equation (14) to calculate the stress intensity factor I. The mean particle diameter s_0 can be extracted from the grain size analysis of the experimentally produced particles and is defined as the size fraction that contains the highest amount of newly created surface. In the case of AMS s_0 is 280 μm, for AST samples 180 μm. For both materials a speed of sound of 1800 m s^{-1} was assumed (porous magma). The resulting stress intensity factors I are 3.0×10^2 N $m^{3/2}$ for AMS and 4.5×10^2 N $m^{3/2}$ for AST. These values are in good agreement with respective stress intensity factors for porous media at high temperatures [*Sih*, 1973; *Shan and Leng*, 1999; *Steen*, 1999].

7. Energy Considerations

[22] The products of the experiments are practically identical to the products from the investigated deposits in terms of grain size, grain morphology, and chemical composition. The differences between the natural products AMS and AST can also be found in their experimental analogues, especially the grain size distribution of the experimental

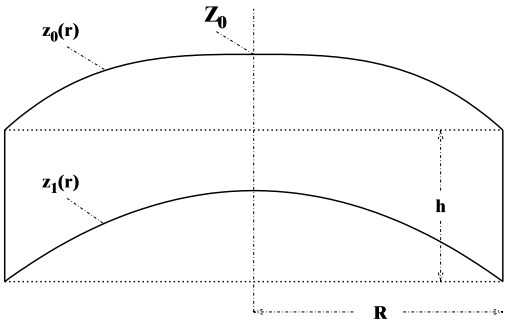

Figure 9. Schematic drawing of the geometric parameters used for calculation of the strain rate (also see Figure 1).

samples mirrors the data from literature [*De Gennaro et al.*, 1999; *Dellino et al.*, 2001]: in both curves the AST samples display a significant shift to smaller grain sizes, whereas the general shapes of the distribution curves are very similar. As the variation of driving pressure does not significantly change the grain size distribution, these differences can be assigned to different material properties of the magmas prior to fragmentation.

[23] The fragmentation energy (E_{frag}) can be calculated from the measured pressure, force, and ejection speed data with the use of

$$E_{frag} = E_{total} - (E_{kin} + E_{seis} + E_{son}) \quad (24)$$

where E_{total} denotes the total kinetic energy acting on the melt plug, E_{kin} the energy of movement (i.e., deformation and ejection of the plug mass), E_{seis} the energy released as shock waves and elastic waves, and E_{son} is the acoustic energy. The amount of acoustic energy released during comparable subaerial blast operations is well known from mining engineering [e.g., *Ex and Schmücker*, 2000] and cannot exceed 5% of E_{total}. Because of this minor importance and because of the large experimental effort needed for this measurement in a complex acoustic environment, the acoustic energy was neglected for our calculations. In the case of submarine explosions, however, the proportional importance of E_{son} can be much higher, because of the incompressible coupling and the much lower acoustic impedance between magma and water.

[24] E_{total} can be expressed by the work of compression $W = \Delta p\ V$ [J], and calculated from the recorded driving pressure. The record of the repulsion force transducer contains (E_{kin} + E_{seis}) [*Zimanowski et al.*, 1997a]. Using the high-speed video recordings, E_{kin} can be obtained from the maximum ejection speed of the plug mass. Thus E_{seis} can also be calculated. For the case of AMS this results in 50% E_{Frag}, 30% E_{kin}, and 20% E_{seis}, for AST in 75% E_{Frag}, 15% E_{kin}, and 10% E_{seis}.

[25] The specific shear stress, i.e., the energy needed for the generation of new surface, can now be expressed as the ratio between E_{Frag} and the total fracture surface. This calculation results in (69 ± 7) J m^{-2} for AMS and (392 ± 26) J m^{-2} for AST. The experimental AST melt was found to be more than five times "stronger" than the experimental AMS melt! The apparent Newtonian viscosity of AMS melt, however, was found to be significantly higher than the viscosity of AST melt. This, at least in the investigated case, shows that Newtonian viscosity measurements are not useful to characterize the brittle-mode fragmentation behavior of magma. On the other hand, the granulometric field observations (see above) are in good agreement with our experimental results.

[26] Combining the specific shear stress and the SFS (Table 2), the specific fragmentation energy (in J kg^{-1}) can be calculated for each grain size fraction. If the total mass of the deposit of one explosive e and the granulometric data is available, E_{Frag} for this eruption can be calculated. In first approximation [Dellino, unpublished data] this calculation results in 8.7×10^{13} J for the AMS and 7.7×10^{13} J for the AST eruption in the Campi Flegrei Caldera. If the energy dissipation during these eruptive events can be assumed to be similar as in the experiments (see above), the totally released kinetic energy also can be approximated: 17.4×10^{13} J, i.e., 40 kt TNT equivalent for AMS and 10.27×10^{13} J, i.e., 25 kt TNT equivalent for AST. In both cases, this represents significantly less than 1% of the total initial thermal energy.

8. Conclusions and Outlook

[27] The reconstruction of past eruptions from their deposits, together with surveillance of the ongoing activity, represents a major tool for hazard assessment and civil defense in areas threatened by active volcanoes. The target of our work was to establish a link between field work and experimental determination of material properties, fragmentation dynamics, and energy balances. Thickness, dispersion, and grain size distribution are probably the best known parameters of volcanic deposits worldwide. Making use of basic thermodynamics and standardized material property measurements, the methodology presented here should be applicable in many cases to infer the kinetic energy release of selected explosive eruptions. Furthermore, the reconstruction of strain rates from grain size data yields information on the dynamics within the conduit prior to fragmentation. Making use of these data for the refinement of existing numerical simulations should increase the quality of risk prediction and hazard management.

[28] Experimental data, theoretical considerations, and field data of the pyroclastic deposits, selected for this study from recent Campi Flegrei eruptions, result in a consistent picture of the physical conditions leading to the their production. If the grain size distribution of volcanic ash of deposits from explosive magmatic eruptions (and also phreatomagmatic eruptions with a low host rock content) can be reconstructed and basic material properties are known, the maximum strain rates acting on the magma prior to fragmentation can be calculated. I a first approximation this can be done using a mean size to characterize the degree of fragmentation of one deposit. In contrast to the use of mean grain sizes in the context of transport and sedimentation, we propose to define this mean size in respect to the size fraction that contributes the largest increase in surface.

[29] **Acknowledgments.** The research was in part funded by the DFG (Germany) in the frame of the SPP 1055 and by the Italian INGV-DPC 2001-03/16 project. We wish to express our thanks to Gregory Valentine, Magnús Tomi Gudmundsson, and the Editors of JGR for their great help in improving the manuscript.

References

Bottinga, Y. (1994), Rheology and rupture of homogeneous silicate liquids at magmatic temperatures, *J. Geophys. Res.*, *99*, 9415–9422.

Buisson, C., and O. Merle (2002), Experiments on internal strain in lava dome cross sections, *Bull. Volcanol.*, *64*, 363–371, doi:10.1007/s00445-002-0213-6.

Büttner, R., and B. Zimanowski (1998), Physics of thermohydraulic explosions, *Phys. Rev. E*, *57*, 5726–5729.

Büttner, R., P. Dellino, and B. Zimanowski (1999), Identifying modes of magma/water interaction from the surface features of ash particles, *Nature*, *401*, 688–690.

Büttner, R., P. Dellino, L. La Volpe, V. Lorenz, and B. Zimanowski (2002), Thermohydraulic explosions in phreatomagmatic eruptions as evidenced by the comparison between pyroclasts and products from Molten Fuel Coolant Interaction experiments, *J. Geophys. Res.*, *107*(B11), 2277, doi:10.1029/2001JB000511.

Chandrasekhar, S. (1968), *Hydrodynamic and Hydromagnetic Stability*, 2nd ed., Oxford Univ. Press, New York.

De Gennaro, M., A. Incoronato, G. Mastrolorenzo, M. Adabbo, and G. Spina (1999), Depositional mechanisms and alteration processes in different types of pyroclastic deposits from Campi Flegrei volcanic field (southern Italy), *J. Volcanol. Geotherm. Res.*, *91*, 303–320.

Dellino, P., and L. LaVolpe (1995), Fragmentation versus transportation mechanisms in the pyroclastic sequence of Monte Pilato Rocche Rosse (Lipari, Italy), *J. Volcanol. Geotherm. Res.*, *64*, 211–231.

Dellino, P., R. Isaia, L. La Volpe, and G. Orsi (2001), Statistical analysis of textural data from complex pyroclastic sequences: Implications for fragmentation processes of the Agnano-Monte Spina Tephra (4.1 ka), Phlegraean Fields, southern Italy, *Bull. Volcanol.*, *63*, 443–461.

Dellino, P., R. Isaia, and M. Veneruso (2004), Turbulent boundary layer shear flows as an approximation of base surges at Campi Flegrei (southern Italy), *J. Volcanol. Geotherm. Res.*, *133*, 211–228.

De Vita, S., et al. (1999), The Agnano Monte Spina eruption (4.1 ka) in the resurgent, nested Campi Flegrei caldera (Italy), *J. Volcanol. Geotherm. Res.*, *91*, 269–301.

Di Vito, M. A., R. Isaia, G. Orsi, J. Southon, S. de Vita, M. D'Antonio, L. Pappalardo, and M. Piochi (1999), Volcanic and deformational history of the Campi Flegrei caldera in the past 12 ka, *J. Volcanol. Geotherm. Res.*, *91*, 221–246.

Ex, W., and G. A. Schmücker (2000), Neuerungen im Erschütterungs-Immissionsschutz, *Sprenginfo*, *1*, 3–17.

Fulignati, P., P. Marianelli, M. Proto, and A. Sbrana (2004), Evidences for disruption of a crystallizing front in a magma chamber during caldera collapse: An example from the Breccia Museo unit (Campanian Ignimbrite eruption, Italy), *J. Volcanol. Geotherm. Res.*, *133*, 141–155.

Grady, D. E. (1988), The spall strengths of condensed matter, *J. Mech. Phys. Solids*, *36*, 353–384.

Heiken, G., and K. H. Wohletz (1985), *Volcanic Ash*, 246 pp., Univ. of Calif. Press, Berkeley.

Herrmann, H. J., and S. Roux (1990), *Statistical Models for the Fracture of Disordered Media*, 364 pp., Elsevier, New York.

Isaia, R., M. D'Antonio, F. Dell'Erba, M. Di Vito, and G. Orsi (2004), The Astroni volcano: The only example of closely spaced eruptions in the same vent area during the recent history of the Campi Flegrei caldera (Italy), *J. Volcanol. Geotherm. Res.*, *133*, 171–192.

Lawn, B. (1993), *Fracture of Brittle Solids*, 398 pp., Cambridge Press, New York.

Orsi, G., M. A. Di Vito, and R. Isaia (2004), Volcanic hazard assessment at the restless Campi Flegrei caldera, *Bull. Volcanol.*, *66*, 514–530.

Raue, H. (2004), A new model for the fracture energy budget of phreatomagmatic explosions, *J. Volcanol. Geotherm. Res.*, *129*, 99–108.

Schowalter, W. R. (1978), *Mechanics of Non-Newtonian Fluids*, 301 pp., Elsevier, New York.

Sih, G. C. (1973), *Handbook of Stress Intensity Factors*, 178 pp., Lehigh Univ., Bethlehem, Pa.

Shan, Z., and Y. Leng (1999), Fracture and fatigue behavior of sintered steel at elevated temperatures: part II. Fatigue crack propagation, *Metall. Mater. Trans. A*, *30*, 2895–2913.

Steen, M. (1999), Fractography and fracture mechanics property assessment of advanced structural ceramics, *Int. Mater. Rev.*, *44*, 165–216.

Varotosos, P. A., and K. D. Alexopoulos (1986), *Thermodynamics of Point Defects and Their Relation With Bulk Properties*, 326 pp., Elsevier, New York.

Yew, C. H., and P. A. Taylor (1994), A thermodynamic theory of dynamic fragmentation, *Int. J. Impact Eng.*, *15*, 385–394.

Zimanowski, B. (1998), Phreatomagmatic explosions, in *From Magma to Tephra*, edited by A. Freundt and M. Rosi, pp. 25–54, Elsevier, New York.

Zimanowski, B., R. Büttner, V. Lorenz, and H.-G. Häfele (1997a), Fragmentation of basaltic melt in the course of explosive volcanism, *J. Geophys. Res.*, *102*, 803–814.

Zimanowski, B., R. Büttner, and J. Nestler (1997b), Brittle reaction of a high temperature ion melt, *Europhys. Lett.*, *38*, 285–289.

Zimanowski, B., K. H. Wohletz, R. Büttner, and P. Dellino (2003), The volcanic ash problem, *J. Volcanol. Geotherm. Res.*, *122*, 1–5.

R. Büttner, H. Raue, I. Sonder, and B. Zimanowski, Physikalisch Vulkanologisches Labor, Institut für Geologie der Universität Würzburg, Pleicherwall 1, D-97070 Würzburg, Germany. (zimano@geologie.uni-wuerzburg.de)

P. Dellino, Dipartimento Geomineralogico, Universitá degli Studi di Bari, Via E. Orabona 4, I-70125 Bari, Italy.

Die Natur des Menschen ist iterativ.